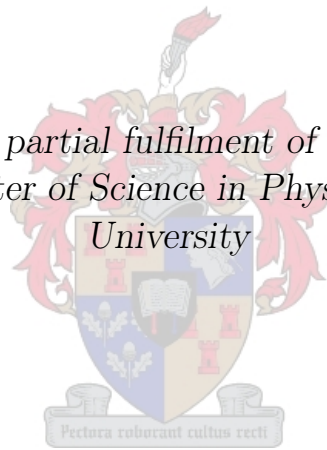


SCATTERING IN SOLITON MODELS AND CROSSING SYMMETRY

by

A.M.H.H. ABDELHADY

*Thesis presented in partial fulfilment of the requirements for
the degree of Master of Science in Physics at Stellenbosch*



Department of Physics,
University of Stellenbosch,
Private Bag X1, Matieland 7602, South Africa.

Supervisor: Prof. Herbert Weigel

December 2012

Declaration

By submitting this thesis electronically, I declare that the entirety of the work contained therein is my own, original work, that I am the owner of the copyright thereof (unless to the extent explicitly otherwise stated) and that I have not previously in its entirety or in part submitted it for obtaining any qualification.

Date: December 2012

Copyright © 2012 Stellenbosch University
All rights reserved.

Abstract

Crossing symmetry relates scattering and annihilation processes to each other. Its derivation is straightforward in perturbative approaches to quantum field theory: it merely reflects the exchange of in- and outgoing states in Feynman diagram computations. In soliton models, the situation is much more complicated because the scattering and the annihilation processes concern distinct topological sectors that are not related by any continuous transformation.

In this thesis a simple soliton model will be employed to address this problem numerically. First, in the unit topological sector we extract asymptotically the phase shift of the scattering process of a wave packet off the kink-solution. To this end we solve the time-dependent equation of motion of the non-integrable φ^4 field model in $(1 + 1)$ space-time dimensions for two distinct initial conditions: the wave packet in a trivial vacuum background and in the background of the kink-solution.

Second, in the topologically trivial sector we present numerical solutions of the kink–antikink interaction in the same model. We find that the final state of this interaction varies dramatically with the impact velocity. As result, we analyze our numerical solutions for the kink–antikink collisions system in two regimes. For the initial velocity of the system less than some critical velocity, $v_c \approx 0.26$, the kink and the antikink either annihilate or inelastically scatter. On the other hand, the kink and the antikink always inelastically scatter when the initial velocity of the system is higher than this critical velocity. However, the scattering processes of the kink–antikink with initial velocity below and above the critical velocity are different. Below the critical velocity the kink and the antikink collide and always undergo n -bounces ($n \geq 2$) before they depart to infinity. When the initial velocity of the system is higher than v_c , the kink and the antikink depart to infinity after only one bounce. We present a qualitative description for these bounce effects between the kink and the antikink motivated by earlier studies as well as our numerical simulations. We utilize collective coordinates to study the dynamics of the kink–antikink system in two degrees of freedom. In this regime, we modify the ansätze of the kink–antikink system from earlier studies to account for relativistic effects. We perform a comparison between this approximation and the full system. We end our discussion of this sector by discussing the scattering data for the inelastic scattering and the annihilation processes of the kink–antikink.

Third, we compare the extracted scattering data for the scattering process of a wave packet off the kink-solution and the annihilation process of the kink–antikink to each other. Finally, these studies of different sectors allow us to make a conjecture about the validity of crossing symmetry within the non-integrable φ^4 field model.

Opsomming

Kruising-simmetrie beskryf 'n verband tussen verstrooiings- en vernietigingsprosesse. Die afleiding daarvan binne die raamwerk van steuringsteorie is eenvoudig: dit behels bloot die omruil van ingaande en uitgaande toestande in die Feynman-diagram. In soliton-modelle is die situasie egter meer ingewikkeld aangesien die verstrooiings- en vernietigingsprosesse in verskillende topologiese sektore plaasvind wat nie deur kontinue transformasies aan mekaar gekoppel is nie.

In hierdie tesis word daar van 'n eenvoudige soliton-model gebruik gemaak om hierdie probleem numeries te ondersoek. Eerstens word die faseverskuiwing van die verstrooiingsproses van 'n golfpakkie vanaf 'n kinkoplossing asimptoties in die topologiese eenheidssektor bepaal. Vir hierdie doel word die tydafhanklike bewegingsvergelykings van die klassieke, nie-integreerbare ϕ^4 -veldeteorie in (1+1) dimensionele ruimte-tyd opgelos. Twee beginkondisies word ondersoek: 'n golfpakkie in die triviale vakuum agtergrond asook in die kinkoplossing agtergrond. Tweedens ondersoek ons ook numeriese oplossings vir die kink-antikink wisselwerking binne die triviale topologiese sektor van dieselfde model. Hier vind ons dat die finale toestand van hierdie wisselwerkingsproses op 'n uiters sensitiewe wyse van die impaksnelheid afhang. Ons ondersoek gevolglik die numeriese oplossings vir die kink-antikink botsings in twee gebiede. Vir beginsnelhede onder die kritieke snelheid $v_c \approx 0.26$ sal die kink en antikink mekaar óf vernietig óf nie-elasties verstrooi. In teenstelling hiermee sal die kink-antikink altyd nie-elastiese verstrooiing ondergaan as die beginsnelheid die kritieke snelheid oorskry. Die aard van die verstrooiingsprosesse vir beginsnelhede bo en onder die kritieke snelheid is egter verskillend. Onder die kritieke snelheid sal die kink en antikink 'n n -bots proses ($n \geq 2$) ondergaan voor hulle finaal van mekaar weg beweeg. Bo die kritieke snelheid sal die kink-antikink egter net 'n enkele botsing ondergaan en dan uitmekaar beweeg. Ons lewer 'n kwalitatiewe beskrywing vir die bots-effek tussen die kink en antikink wat deur vorige studies asook ons numeriese resultate gemotiveer word. Ons maak gebruik van 'n kollektiewe koördinaatstelsel om die dinamika van die kink-antikink in terme van twee vryheidsgrade te bestudeer. In hierdie gebied pas ons ook die ansatz vir die kink-antikink stelsel aan om relativistiese effekte in ag te neem. Ons vergelyk dan hierdie benadering met die oplossing van die volle sisteem. Die bespreking van hierdie sektor word afgesluit met 'n analise van die verstrooiingsdata vir die verstrooiing- en vernietigingsprosesse van die kink-antikink.

Derdens vergelyk ons die verstrooiingsdata vir die verstrooiing van 'n golfpakkie vanaf 'n kinkoplossing met die van die vernietigingsproses van die kink-antikink. Ons studie van die verskillende sektore laat ons dan toe om 'n vermoede te formuleer oor die geldigheid van kruising-simmetrie binne die nie-integreerbare ϕ^4 -model.

Acknowledgements

All Praise and Glory be to Allah. I would like to express my deepest and sincere gratitude to my supervisor Prof. Herbert Weigel for his non-stop guidance, assistance and dedication of attention and effort to direct me always into the right way during my M.Sc. research. Also, I am really grateful for his guidance and assistance for the English matter in this thesis.

I would like to thank the African Institute for Mathematical Sciences (AIMS), Stellenbosch University, NRF and NITheP for supporting me financially. Also, I would like to thank the Physics Department, Stellenbosch University, specially the theoretical physics group for the facility of the research. Further, I would like to thank Mr. Ryno Botha and Dr. Hannes Kriel for helping me to translate my thesis abstract from English Language to Afrikaans Language.

Dedications

*To my parents, brothers and sisters in Egypt.
Further, to my best friends in Egypt, Libya and South Africa.*

Contents

Declaration	i
Abstract	ii
Opsomming	iii
Acknowledgements	iv
Dedications	v
Contents	vi
1 Introduction	1
1.1 Brief discussion of nonlinear systems	1
1.2 Outline	5
2 Crossing symmetry in perturbation theory	6
2.1 Lagrangian formalism	6
2.2 Free scalar fields	7
2.2.1 Quantization of free fields	8
2.3 Complex scalar particle fields	9
2.4 Perturbation theory and Feynman diagrams	10
2.4.1 Feynman diagrams	13
2.5 Crossing symmetry	15
3 Classical soliton models	17
3.1 Kink-solution of φ^4 model	18
3.1.1 Small fluctuations approach	20
3.2 Topological charges	22
3.3 Soliton solution of sine-Gordon model	24
4 Scattering off solitary waves	29
4.1 Scattering off the kink solution	29
4.2 Scattering off the soliton solution	31
4.3 Deformed kink-solution	32

5	Scattering a wave packet off a kink solution	34
5.1	Wave packet and background	34
5.2	Numerical Results	36
5.2.1	Propagation of pure wave packet	39
5.2.2	Propagation in kink background	41
5.2.3	Extraction of the phase shift	42
5.2.4	Nonlinear effects in the kink background	44
6	Kink–antikink collisions	46
6.1	Numerical results	48
6.2	Novel features	53
6.3	Extraction of scattering data	56
6.3.1	Inelastic scattering process	57
6.3.2	Annihilation process	59
7	Summary and Conclusion	61
A		65
A.1	Wick’s Theorem for equation (2.32)	65
A.2	Feynman rules for model (2.27)	65
A.3	Traveling wave solution for φ^4 model	66
A.4	Traveling wave solution for sine-Gordon model	67
B		68
B.1	Numerical solutions	68
	References	71

Chapter 1

Introduction

This thesis centers on obtaining information about crossing symmetry in nonlinear field theories that have a soliton solution, in particular the non-integrable φ^4 field model in $(1+1)$ space-time dimensions. Crossing symmetry plays a crucial role in particle physics. It is defined as the property of scattering amplitudes that allows antiparticles to be interpreted as particles going backwards in time. In ordinary perturbation theory it allows one to relate the scattering amplitudes of two different processes to each other by analytic continuation. For example, the scattering amplitude of $e^+e^- \rightarrow \mu^+\mu^-$ (annihilation process) can be obtained from the scattering amplitude of $e^-\mu^- \rightarrow e^-\mu^-$ (scattering process) by analytic continuation [1, 2]. Another example, exclusive proton-antiproton annihilation into two photons, $p\bar{p} \rightarrow \gamma\gamma$, can be regarded as the Compton process in the crossed channel [3]. Moreover, space- and time-like form factors can be related to each other by analytic continuation. In nonlinear field theories with soliton solutions the situation is much more complicated, because crossing symmetry relates two different processes (scattering and annihilation), which concern distinct topological sectors. These sectors are not related by any continuous transformation.

1.1 Brief discussion of nonlinear systems

Nonlinear field systems have attracted numerous groups in physics [4, 5, 6, 7, 8]. Scientists from various branches of physics have been coming to grips with the fact that the time-honored method of linearizing any nonlinearities that occur in their equations omits phenomena which are of great importance. Nonlinearity is therefore a captivating manifestation of the observable universe, whose importance has been increasingly recognized over the decades, and has found more and more fields of application ranging from elementary particles, nuclear physics, biology, wave dynamics at any scale, fluids, plasmas to astrophysics.

One of the most interesting studies of nonlinear systems that has received a great deal of attention is that of Nonlinear Waves [9, 10]. In particular, solitary wave solutions that are localized and depend on position x and time t only through the argument $x - ct$ have had a great impact on the scientific community. Of particular interest is a special type of solitary wave called a soliton, which has the additional property that its shape

and velocity are preserved asymptotically upon collisions with other solitary waves. This is a familiar situation when one is dealing with a linear dispersionless system such as the wave equation in a dispersionless medium. However, the addition of dispersion or nonlinearity tends to cause the shape of a pulse to spread or sharpen, respectively, [11, 12]. It is therefore remarkable that when both dispersion and nonlinearities are present in the correct proportions, the spreading and sharpening exactly cancel, giving rise to solitons.

To point out these remarkable solutions (solitons) and clarify the difference between them and solitary waves, we consider a simple relativistic wave equation

$$\left(\frac{1}{c^2} \frac{\partial^2}{\partial t^2} - \frac{\partial^2}{\partial x^2} \right) \varphi(t, x) = 0, \quad (1.1)$$

where $\varphi(t, x)$ is a real scalar field in $(1 + 1)$ space-time dimensions. The properties of this equation are well known: it is both linear and dispersionless. As a result, its solutions have two features of relevance to our discussion:

- i) Any real well-behaved function of the form $\varphi(t, x) = f(x \pm ct)$ is a solution of equation (1.1). In particular, if we choose a localized function f , we can construct a localized wave packet¹ that will travel with uniform velocity $\pm c$, and no distortion in shape. This is obviously related to the fact that plane waves $\cos [k(x \pm ct)]$ and $\sin [k(x \pm ct)]$ with frequency $\omega = kc$ form a complete set of solutions to equation (1.1). Any well-behaved localized function, say $f(x - ct)$, can be written as

$$f(x - ct) = \int dk (a_1(k) \cos [k(x - ct)] + a_2(k) \sin [k(x - ct)]), \quad (1.2)$$

since by linearizing we can form arbitrary combinations of these plane wave solutions. The fact that the wave packet $f(x \pm ct)$ travels undistorted with velocity c is related to the fact that all its plane-wave components have the same wave velocity $c = \omega/k$.

- ii) Since the wave equation is linear, given two localized wave packet solutions $f_1(x - ct)$ and $f_2(x + ct)$, their sum $f_3(t, x) = f_1(x - ct) + f_2(x + ct)$ is also a solution. At very early time ($t \rightarrow -\infty$), $f_3(t, x)$ consists of the two packets widely separated and approaching each other essentially undistorted. At a finite time t , they collide. But after collision, at very late time ($t \rightarrow +\infty$), they will asymptotically separate into the same two packets, retaining their original shapes and velocities. For the system of equation (1.1), these properties hold for more than two packets as well.

These two features, namely (i) the shape and velocity retention of a single packet and (ii) the asymptotic shape and velocity retention of several packets even after collision, clearly hold for equation (1.1) because this particularly simple system is both linear and dispersionless. It is noted in refs.[8, 11] that the addition of even simple terms to equation

¹The wave packet is defined as a localized wave function that consists of a group of waves of slightly different wavelengths, with phases and amplitudes chosen such that they interfere constructively over a small region of space and destructively elsewhere [13].

(1.1) tends to destroy these remarkable features, even in $(1 + 1)$ space-time dimensions. For instance, adding the term $m^2 c^2 \varphi(t, x)$ to the right hand side of equation (1.1), we get the Klein-Gordon equation in two dimensions

$$\left(\frac{1}{c^2} \frac{\partial^2}{\partial t^2} - \frac{\partial^2}{\partial x^2} + m^2 c^2 \right) \varphi(t, x) = 0. \quad (1.3)$$

This equation is still linear and the plane waves $\cos[k(x \pm ct)]$ and $\sin[k(x \pm ct)]$ still form a complete set of solutions. But now the dispersion relation is $\omega^2 = k^2 c^2 + m^2 c^4$. These different wavelengths travel at different velocities $\frac{\partial \omega(k)}{\partial k}$, and the equation is dispersive. At time $t = 0$, any localized wave packet having the form

$$\int dk (a_1(k) \cos(kx) + a_2(k) \sin(kx)), \quad (1.4)$$

will spread as time goes on. Thus, feature (i) is lost, and so is feature (ii). If even a single packet cannot retain its shape, there is no question of several packets retaining their shapes after collision. Similarly, we consider adding a simple nonlinear term to equation (1.1) as in

$$\left(\frac{1}{c^2} \frac{\partial^2}{\partial t^2} - \frac{\partial^2}{\partial x^2} \right) \varphi(t, x) + \varphi^3(t, x) = 0. \quad (1.5)$$

Not all solutions of this equation are known, but one can persuade oneself through numerical or approximate calculations that an arbitrary wave packet will spread out and break (*i.e.* the nonlinear term in the KdV (Korteweg-de Vries) equation makes its localized wave solution spread out [11]). However, it is possible that for some equations where both dispersive and nonlinear terms are present, their effects might balance each other in such a way that some special solutions do essentially enjoy feature (i). These solutions are called “Solitary Waves”. In a small subset of these cases, feature (ii) is also exhibited and those solutions are called “Solitons”.

The history of these special solutions dates to 1834, while the Scottish engineer John Scott-Russell was the first to discover them in nature. Here we recite what he reported in his 1844 ‘Report on Waves’ [14]

“I was observing the motion of a boat which was rapidly drawn along a narrow channel by a pair of horses, when the boat suddenly stopped not so the mass of water in the channel which it had put in motion; it accumulated round the prow of the vessel in a state of violent agitation, then suddenly leaving it behind, rolled forward with great velocity, assuming the form of a large solitary elevation, a rounded, smooth and well-defined *heap of water*, which continued its course along the channel apparently *without change of form or diminution of speed*. I followed it on horseback, and overtook it still rolling on at a rate of some eight or nine miles an hour, *preserving* its original figure some thirty feet long and a foot to a foot and a half in height”

He called this phenomena the “*great wave of translation*”. Since then, these waves have been reproduced in the laboratory and their properties investigated.

In 1962, the first evidence that mathematical models could have soliton solutions was given by Perring and Skyrme [15] in their numerical investigation of the sine-Gordon (SG) equation. They found that after colliding, two of these solitary waves emerged with the same shape and velocity that they had long before they interacted. In 1965, results of a similar numerical investigation were published by Zabusky and Kruskal in ref.[16], this time using the Korteweg-deVries (KdV) model. These calculations led to analytic multi-soliton solutions describing the collisions. Soon an entire hierarchy of solitons was produced with the help of Bäcklund transformations [17], which transform an “ n -humped” solution to an “ $n + 1$ -humped” solution.

The φ^4 model constitutes one of the most well known non-integrable models. In this model, we do have an analytic form for a solitary wave, but we cannot use the beautiful machinery of Bäcklund transformations or the Inverse Scattering Transform [17] as a method to generate and/or study soliton solutions. Although this removes one of the only nonperturbative tools for investigating solitary waves, it has not stopped efforts to study this system, as is evidenced by the large number of applications found for non-integrable as well as integrable models.

Undoubtedly the applications of these models are of great interest to physicists. Scott-Russell’s observation of a solitary wave in water was the first example of a physical system bearing soliton solutions. Since then, solitary waves and their numerical simulations have found their way into modern applications, due to their topological properties, such as Langmuir solitons in plasmas [18], solitons in Josephson junctions [19], estimation of the transition time of a phonon through the kink-solution [20], and baryons as solitons in effective meson models for QCD [21], to name a few.

The first application of soliton models in particle physics came through the famous Skyrme model [22]. It is a model of interacting mesons that illustrates how the particle can be built from a wave-packet of mesons. This system is a prototype soliton picture for baryons [23]. As an additional advantage over many models in particle physics, the soliton description represents a means for studying various aspects like meson-baryon scattering and photoproduction [24], baryon–antibaryon annihilation [25], etc.

The non-integrable φ^4 field model has a venerable place in modern applications. The unit topological charge sector has been used to study the interaction of cluster walls with phonons in a one dimensional model for displacive structural phase transitions in ref.[20], and might have applications in condensed matter and cosmology [26]. Earlier numerical simulations in this sector have been employed to investigate the effect of impurities in the kink [27], and to study the brane world collisions [28, 29, 30]. Recently, numerical solutions were able to extract the phase shift of a scattered wave packet in the scattering process of a wave packet off a kink-solution [31].

Furthermore, the topologically trivial sector has been used to study the resonance structure of kink–antikink interaction [32]. Lattice studies of the kink model were reported in refs.[33, 34] as a simulation of molecular dynamics. More recently, this sector has been investigated numerically in the context of pair–creation [35], electro–weak oscillons [36, 37] and bounces [38, 39]. Numerical simulations within the $(2 + 1)$ dimensional generalization at non–zero temperature allowed for studying the effect of fast quenches in resonant nucleation [40].

To this end, motivated by all of these applications of the soliton-model of the non-integrable φ^4 field theory, we perform individual numerical simulations for the kink–wave packet (phonon) scattering and the kink–antikink annihilation processes. Then, we investigate the crossing symmetry between these interactions. Crossing symmetry should relate the kink–antikink annihilation process to the kink–phonon scattering process, where phonons are (small) oscillations about the kink-solution. This means that two distinct topological sectors can be related to each other without any continuous transformation. At the end of this thesis, we explain that crossing symmetry is possible topologically in the non-integrable φ^4 field theory. However, it is not manifest because of the extremely long life of the bion state which forms from the kink–antikink annihilation. Further, in the kink–antikink collisions, we modify the ansätze of the collective coordinate approximation from earlier studies to account for relativistic effects. Then, in this framework we study the kink–antikink collisions in a reduced description that initializes only two degrees of freedom. In this regime we present a thorough comparison with the full system. Also, we determine the shape of the potential energy between the kink–antikink at different initial velocities and discuss whether an internal shape mode is responsible for the bounce effects between the kink–antikink pairs system.

1.2 Outline

We devote chapters 2, 3 and 4 to our analytical discussion and chapters 5 and 6 to our numerical studies. Chapter 2 gives an explanation of crossing symmetry in a perturbative treatment, which relates the amplitude from the meson–baryon scattering process to the one from the baryon–antibaryon annihilation process. Chapter 3 gives an overview of two classical soliton models, the φ^4 and sine-Gordon models, and their topological properties. Chapter 4 discusses the small fluctuations about the solutions of the φ^4 and sine-Gordon models and the excited kink-solution. Chapter 5 presents numerical solutions of the scattering process of a wave packet off the kink-solution of the φ^4 model and the extraction of the phase shift. Also, we observe nonlinear effects beyond the small amplitude approximation. Chapter 6 presents numerical solutions of the kink–antikink collisions in the φ^4 model and the reduced collective coordinate approach of the kink–antikink. This chapter ends with the extraction of scattering data for the kink–antikink interaction. Finally, chapter 7 summarizes our numerical solutions from the previous chapters. We then conclude and make our conjecture about the crossing symmetry in solitons of the non-integrable φ^4 field model in $(1 + 1)$ space-time dimensions. Appendix A shows Wick’s Theorem and Feynman rules and ends with the discussion of traveling wave solutions for the φ^4 and sine-Gordon models. Appendix B presents our numerical treatment for solving the equation of motion in the φ^4 model.

Chapter 2

Crossing symmetry in perturbation theory

In this chapter we utilize a scalar field theory in $(1 + 1)$ space-time dimensions to explain crossing symmetry in Feynman diagrams. This symmetry relates the transition amplitudes of various processes to each other by analytic continuation. This identification takes place between the N particles and their corresponding anti-particles and because of the relation between N -particle scattering matrix elements [41]. We use natural units $c = 1$ and $\hbar = 1$, unless explicitly stated otherwise.

The following section gives an overview of the Lagrangian formalism for the theory of the scalar field. They are followed by a derivation of the second-order Feynman diagrams for meson–baryon scattering and baryon–antibaryon annihilation processes [1, 42, 43]. The purpose of choosing baryons here is that baryons behave like soliton solutions in an effective meson theory [23]. We consider the scalar field of a free particle and quantize the field by expressing it in terms of particle creation and annihilation operators. The free particle and interaction Lagrangians are defined in terms of these operators. The interaction Lagrangian enters into the scattering matrix, a perturbative expansion in terms of the coupling constant. Using Wick’s theorem, the terms are translated into Feynman diagrams. The scattering amplitude follows from the application of Feynman’s rules. We calculate the \mathbf{S} -matrix for the meson–baryon scattering process and the baryon–antibaryon annihilation process. Then the crossing symmetry is a relation between the \mathbf{S} -matrix elements of these processes.

2.1 Lagrangian formalism

Consider a dynamical system whose configuration space (the space of all its possible configurations) is characterized in terms of some manifold M_N of dimension N (the number of degrees of freedom). For example, in the case of a single point particle moving along an infinite straight line, the possible configurations of the system are the positions along that line; therefore its configuration space is the real line, $M_1 = \mathbb{R}$, a one dimensional space, $N = 1$, for this one degree of freedom system. We assume that N is very large ($N \rightarrow \infty$), and show locality in both time and space implies that the Lagrange function,

L , should be given as the space integral of a Lagrangian density, $\mathcal{L}(\varphi, \partial_t\varphi, \partial_x\varphi)$, which means that \mathcal{L} is a function of the field φ and its first time and spatial derivatives, where $\varphi = \varphi(t, x)$ is a scalar field function of the time and space. The action of the system is defined as

$$\mathcal{S}[\varphi] = \int_{t_i}^{t_f} dt L = \int_{t_i}^{t_f} dt \int_{space} dx \mathcal{L}(\varphi, \partial_t\varphi, \partial_x\varphi). \quad (2.1)$$

If we perform an arbitrary variation of the field, $\varphi \rightarrow \varphi + \delta(\varphi)$, subject to the boundary condition $\delta\varphi = 0$ for $t = t_i, t = t_f$ and $x \rightarrow \pm\infty$, then the solution of the variational problem $\delta\mathcal{S} = 0$ leads to the Euler-Lagrange equation

$$\frac{\partial\mathcal{L}}{\partial\varphi} - \partial_\mu \left(\frac{\partial\mathcal{L}}{\partial(\partial_\mu\varphi)} \right) = 0. \quad (2.2)$$

In case of more than one field such an equation applies to each of them.

2.2 Free scalar fields

A free scalar particle of positive mass m is represented by a real field φ that satisfies the Klein-Gordon equation (K.G.)

$$\ddot{\varphi} - \varphi'' + m^2\varphi = 0, \quad (2.3)$$

where $\varphi = \varphi(t, x)$, (t, x) is a point in $(1 + 1)$ space-time dimensions, $\ddot{\varphi}$ and φ'' are the second derivatives of the real field φ with respect to time t and position x , respectively. The K.G. equation (2.3) can be easily derived using the the Euler-Lagrangian equations (2.2) from the free particle Lagrangian density \mathcal{L} , given by

$$\mathcal{L} = \frac{1}{2} \left(\dot{\varphi}^2 - \varphi'^2 - m^2\varphi^2 \right). \quad (2.4)$$

The $\dot{\varphi}$ and φ' are the first derivative of the real field φ with respect to time and space, respectively. The real field φ is a superposition of plane waves $e^{\mp i(E_p t - px)}$ of the form

$$\begin{aligned} \varphi(t, x) &= \int \frac{dp}{(2\pi) \sqrt{2E_p}} \left(a_p e^{-i(E_p t - px)} + a_p^\dagger e^{+i(E_p t - px)} \right) \\ &= \varphi_+(t, x) + \varphi_-(t, x), \end{aligned} \quad (2.5)$$

with $E_p = \sqrt{|p|^2 + m^2}$. Here $\varphi_+(t, x)$ and $\varphi_-(t, x)$ are the positive and negative frequency parts of the field, respectively, given by

$$\varphi_+(t, x) = \int \frac{dp}{(2\pi) \sqrt{2E_p}} a_p e^{-i(E_p t - px)}, \quad (2.6)$$

$$\varphi_-(t, x) = \int \frac{dp}{(2\pi) \sqrt{2E_p}} a_p^\dagger e^{+i(E_p t - px)}, \quad (2.7)$$

where $(\varphi_-)^* = \varphi_+$, and $a_p = a(p)$ and $a_p^\dagger = a^\dagger(p)$ are Fourier amplitudes. The canonical conjugate field is

$$\pi(x) = \frac{\partial \mathcal{L}}{\partial \dot{\varphi}} = \dot{\varphi}. \quad (2.8)$$

The energy momentum tensor is

$$\mathcal{T}^{\mu\nu} = \frac{\partial \mathcal{L}}{\partial(\partial_\mu \varphi)} \partial^\nu \varphi - g^{\mu\nu} \mathcal{L}. \quad (2.9)$$

In particular, the field energy is

$$\mathbb{H} \equiv \mathbf{p}^0 = \int \mathcal{T}^{00} dx = \frac{1}{2} \int (\dot{\varphi}^2 + \varphi'^2 + m^2 \varphi^2) dx \quad (2.10)$$

and the field momentum is

$$\mathbf{p}^1 = \int \mathcal{T}^{01} dx = - \int (\dot{\varphi} \varphi') dx. \quad (2.11)$$

Since the field is a real scalar, it is hermitian with zero intrinsic spin, and there is no phase transformation to yield a charge.

2.2.1 Quantization of free fields

In the quantized theory, the coefficients a_p and a_p^\dagger become annihilation and creation operators, respectively, on particle states $|p\rangle$ in the Fock space. The real scalar field operator, in terms of the annihilation and creation operators, becomes

$$\begin{aligned} \hat{\varphi} &= \int \frac{dp}{(2\pi) \sqrt{2E_p}} (\hat{a}_p e^{-i(E_p t - px)} + \hat{a}_p^\dagger e^{+i(E_p t - px)}) \\ &= \hat{\varphi}_+(t, x) + \hat{\varphi}_-(t, x). \end{aligned} \quad (2.12)$$

The equal-time ($t_x = t_y = t$) commutation relation is

$$[\hat{\varphi}(t, x), \hat{\varphi}(t, y)] = -i\delta(x - y), \quad (2.13)$$

and all other commutation relations are zero. Using the real field operator and its conjugate momentum, it is easy to verify that, in terms of a_p and a_p^\dagger , the commutation relation equation (2.13) entails

$$[\hat{a}_p, \hat{a}_{p'}^\dagger] = (2\pi) \delta(p - p'). \quad (2.14)$$

The Hamiltonian of equation (2.10) can be expressed in terms of the operators

$$\hat{\mathbb{H}} = \int \frac{dp}{(2\pi)} E_p \left(\hat{a}_p^\dagger \hat{a}_p + \frac{1}{2} [\hat{a}_p, \hat{a}_p^\dagger] \right). \quad (2.15)$$

The second term in equation (2.15) makes an infinite contribution and represents an infinite ground state energy. In quantum field theory, we are interested in the energy of states above the ground state, so we discard this infinite term. It is formally removed by the process known as normal ordering. In a normal ordered product of operators, all annihilation operators are placed to the right of creation operators. A bracket of colons $::$ denotes a normal ordered product (however, some books denote the normal order product by N e.g. [41]). For example, $:\hat{a}_p\hat{a}_p^\dagger := \hat{a}_p^\dagger\hat{a}_p$. The normal ordered Hamiltonian is

$$:\hat{H} := \int \frac{dp}{(2\pi)} E_p \hat{a}_p^\dagger \hat{a}_p. \quad (2.16)$$

In section 2.4, we will use Wick's theorem, which renders a time ordered product (denoted by symbol T and explained in section 2.4) into a collection of normal ordered products from which Feynman rules and diagrams are readily extracted. The state $|0\rangle$ with lowest energy is the vacuum state, and is defined by

$$\hat{a}_p|0\rangle \equiv 0; \quad \langle 0|\hat{a}_p^\dagger \equiv 0, \quad (2.17)$$

which is normalized by $\langle 0|0\rangle = 1$. The state $|p\rangle$ describes a single particle of momentum p , and is created by the creation operator acting on the vacuum state

$$|p\rangle = \sqrt{2E_p} \hat{a}_p^\dagger |0\rangle; \quad \langle p| = \sqrt{2E_p} \langle 0|\hat{a}_p. \quad (2.18)$$

2.3 Complex scalar particle fields

In applying scalar field theory to baryons we purposely ignore spin and isospin and treat all baryons as identical. But a real scalar field theory does not distinguish between particles and their corresponding anti-particles (e.g. protons and anti-protons, neutrons and anti-neutrons). We must include electric charge, in considering pair creation and annihilation. These simplifications are appropriate to illuminate the concept of crossing symmetry in a perturbative framework.

The theory of the complex scalar field [41, 43] is very similar to the theory of the real scalar field given in section 2.2. The complex scalar field ψ is assembled from two real scalar field components ψ_1 and ψ_2 ,

$$\psi = \frac{\psi_1 + i\psi_2}{\sqrt{2}}, \quad \bar{\psi} = \frac{\psi_1 - i\psi_2}{\sqrt{2}}. \quad (2.19)$$

Since ψ and $\bar{\psi}$ are linear combinations of real scalar fields, they automatically satisfy the K.G. equation (2.3). For baryons and anti-baryons, particle and anti-particle fields are distinguished by having different sets of creation and annihilation operators. The particle field is expressed as a Fourier expansion of plane waves in terms of the coefficients b_p, c_p^\dagger ,

$$\psi(t, x) = \int \frac{dp}{(2\pi)\sqrt{2E_p}} (b_p e^{-i(E_p t - px)} + c_p^\dagger e^{i(E_p t - px)}) \quad (2.20)$$

and the anti-particle field $\bar{\psi}(x)$ is

$$\bar{\psi}(t, x) = \int \frac{dp}{(2\pi) \sqrt{2E_p}} \left(b_p^\dagger e^{+i(E_p t - px)} + c_p e^{-i(E_p t - px)} \right), \quad (2.21)$$

where the coefficients b_p, b_p^\dagger , in the quantized complex scalar field are the annihilation and creation operators for the particle, and the coefficients c_p, c_p^\dagger are the annihilation and creation operators for the anti-particle. The canonical conjugates are

$$\Pi = \dot{\bar{\psi}}; \quad \bar{\Pi} = \dot{\psi}.$$

The equal-time ($t_x = t_y = t$) commutation relations for the complex fields and their canonical conjugates are

$$\begin{aligned} [\dot{\bar{\psi}}(t, x), \psi(t, y)] &= -i\delta(x - y), \\ [\dot{\psi}(t, x), \bar{\psi}(t, y)] &= -i\delta(x - y), \end{aligned} \quad (2.22)$$

and all other commutation relations are zero. From these commutation relations one can deduce that the creation and annihilation operators obey the commutation relations

$$[\hat{b}_p, \hat{b}_q^\dagger] = [\hat{c}_p, \hat{c}_q^\dagger] = (2\pi) \delta(p - q). \quad (2.23)$$

The vacuum state $|0\rangle$ of the particle and the anti-particle Fock space are defined by

$$\hat{b}_p|0\rangle = 0 \quad \text{and} \quad \hat{c}_p|0\rangle = 0, \quad (2.24)$$

respectively. The Fock space is built by the creation operators acting repeatedly on the vacuum state

$$\hat{b}_p^\dagger|0\rangle = \frac{1}{\sqrt{2E_p}}|p\rangle; \quad \hat{c}_q^\dagger|0\rangle = \frac{1}{\sqrt{2E_q}}|q\rangle, \quad (2.25)$$

and the normal ordered Hamiltonian is given by

$$:\hat{H}: = \int \frac{dp}{(2\pi)} E_p \left(\hat{b}_p^\dagger \hat{b}_p + \hat{c}_p^\dagger \hat{c}_p \right). \quad (2.26)$$

2.4 Perturbation theory and Feynman diagrams

So far, we have discussed the free real and complex scalar fields that give descriptions of the free uncharged and charged particles, respectively. To discuss scattering we must include interaction terms in the Lagrangian. In scalar Yukawa theory, there is a perturbative framework for an interacting field theory whenever its Lagrangian is the sum of a free Lagrangian and interaction terms. Each term of the interaction terms is associated with a multiplicative factor g , the coupling constant for that term. The \mathbf{S} -matrix elements of the interacting-field theory are expanded around those of the free-field theory, as a power series in g . In this approach, the interaction is conceived as a small perturbation on the

free theory; the systematic method for expanding in the coupling constant is perturbation theory [43, 44]. Here, we only consider the second order term since our interest is only to illuminate crossing symmetry in the scattering process.

With the introduction of charge in the previous section 2.3, in the interaction of real and complex scalar fields, the simple scalar Lagrangian involving products of real scalar fields is replaced by a Lagrangian involving complex scalar fields to describe the baryons and the anti-baryons, and real scalar fields to describe the exchange particles, the mesons.

The meson–baryon system is characterized by the Lagrangian density

$$\begin{aligned}\mathcal{L} &= \mathcal{L}_0 + \mathcal{L}_{int} \\ &= \frac{1}{2} \left(\dot{\varphi}^2 - \varphi'^2 - m^2\varphi^2 + \dot{\psi}^2 - \psi'^2 - M^2\bar{\psi}\psi \right) + g : \bar{\psi}\psi\varphi : ,\end{aligned}\tag{2.27}$$

where \mathcal{L}_0 and \mathcal{L}_{int} are the free and the interaction Lagrangian densities, respectively. The field φ , in this case, contains the creation and annihilation operators for the meson field with mass m , which is given by equation (2.5). The ψ and $\bar{\psi}$ contain the creation and annihilation operators for the baryon, equation (2.20), and anti-baryon, equation (2.21), fields both with mass M . Each field in the free Lagrangian density \mathcal{L}_0 obeys the K.G. equation (2.3). As mentioned earlier, we treat our scalar Yukawa theory as a toy model for baryons, without spin, interacting with mesons. The commutation relations, for arbitrary separation, are given by equations (2.13) and (2.22). Since the field operator in the interaction picture obeys the free field equations, the interaction Hamiltonian density is

$$\mathcal{H}_{int} = -\mathcal{L}_{int} = -g : \bar{\psi}\psi\varphi : .\tag{2.28}$$

The time evolution operator [43] is defined in terms of the \mathcal{H}_{int} as

$$\begin{aligned}\hat{U}_{int}(t_f, t_i) &= 1 - i \int_{t_i}^{t_f} dt' \int dx \hat{\mathcal{H}}_{int}(t', x) \\ &\quad + \frac{(-i)^2}{2} \int_{t_i}^{t_f} dt_1 \int_{t_i}^{t_f} dt_2 \int dx \int dy T \left(\hat{\mathcal{H}}_{int}(t_1, x) \hat{\mathcal{H}}_{int}(t_2, y) \right) + \dots\end{aligned}$$

Here t_i and t_f are the initial and final time, respectively. T is the time-ordering operator, which operates on every operator in the expansion from the right side to put them in time order. The \mathbf{S} -matrix is defined in terms of the \hat{U}_{int} [43], as¹

$$\mathbf{S} = \frac{\langle f | \hat{U}_{int}(+\infty, -\infty) | i \rangle}{\langle 0 | \hat{U}_{int}(+\infty, -\infty) | 0 \rangle},\tag{2.29}$$

where $|i\rangle$ and $|f\rangle$ are the initial and final noninteracting eigenstates, respectively. The times t_i and t_f are taken to be $-\infty$ and $+\infty$, and $\langle 0 | \hat{U}_{int}(+\infty, -\infty) | 0 \rangle$ is a normalization constant. As indicated earlier, we only pick up the second order term in equation (2.29) that contributes to scattering process [44]. Therefore the scattering matrix becomes

$$\mathbf{S} = \frac{(-i)^2}{2} \left\langle f \left| \int d^2\mathbf{x}_1 \int d^2\mathbf{x}_2 T \left(\hat{\mathcal{H}}_{int}(\mathbf{x}_1) \hat{\mathcal{H}}_{int}(\mathbf{x}_2) \right) \right| i \right\rangle,\tag{2.30}$$

¹Note the difference between the symbol \mathcal{S} for the action and the symbol \mathbf{S} for the scattering matrix.

where $\mathbf{x}_1 = (t_1, x_1)$ and $\mathbf{x}_2 = (t_2, x_2)$. Now, consider

$$|i\rangle \equiv |p_1, p_2\rangle, \quad |f\rangle \equiv |p_3, p_4\rangle, \quad (2.31)$$

where p_1, p_2 are the momentum of the meson and the baryon fields, respectively, before the interactions (at $t_i \rightarrow -\infty$), and p_3, p_4 are the momentum of the meson and the baryon fields, respectively, after the interactions (at $t_f \rightarrow +\infty$). We use equations (2.28) and (2.31) to rewrite equation (2.30) as

$$\mathbf{S} = \frac{(ig)^2}{2} \left\langle p_3, p_4 \left| \int d^2\mathbf{x}_1 \int d^2\mathbf{x}_2 T (: \bar{\psi}(\mathbf{x}_1)\varphi(\mathbf{x}_1)\psi(\mathbf{x}_1) : : \bar{\psi}(\mathbf{x}_2)\varphi(\mathbf{x}_2)\psi(\mathbf{x}_2) :) \right| p_1, p_2 \right\rangle. \quad (2.32)$$

Using Wick's theorem (Appendix A.1)

$$\begin{aligned} T (: \bar{\psi}(\mathbf{x}_1)\varphi(\mathbf{x}_1)\psi(\mathbf{x}_1) : : \bar{\psi}(\mathbf{x}_2)\varphi(\mathbf{x}_2)\psi(\mathbf{x}_2) :) &= : \bar{\psi}(\mathbf{x}_1)\varphi(\mathbf{x}_1)\psi(\mathbf{x}_1)\bar{\psi}(\mathbf{x}_2)\varphi(\mathbf{x}_2)\psi(\mathbf{x}_2) : \\ &+ : \bar{\psi}(\mathbf{x}_1)\varphi(\mathbf{x}_1)\varphi(\mathbf{x}_2)\psi(\mathbf{x}_2) : \overbrace{\psi(\mathbf{x}_1)\bar{\psi}(\mathbf{x}_2)} \\ &+ : \bar{\psi}(\mathbf{x}_1)\psi(\mathbf{x}_1)\bar{\psi}(\mathbf{x}_2)\psi(\mathbf{x}_2) : \overbrace{\varphi(\mathbf{x}_1)\varphi(\mathbf{x}_2)} \\ &+ \dots, \end{aligned} \quad (2.33)$$

where

$$\overbrace{\varphi(\mathbf{x}_1)\varphi(\mathbf{x}_2)} \equiv \langle 0|T(\varphi(\mathbf{x}_1)\varphi(\mathbf{x}_2))|0\rangle = \int \frac{d^2\mathbf{k}}{(2\pi)^2} \frac{ie^{-ik\cdot(\mathbf{x}_1-\mathbf{x}_2)}}{k^2 - m^2}, \quad (2.34)$$

$$\overbrace{\psi(\mathbf{x}_1)\bar{\psi}(\mathbf{x}_2)} \equiv \langle 0|T(\psi(\mathbf{x}_1)\bar{\psi}(\mathbf{x}_2))|0\rangle = \int \frac{d^2\mathbf{k}'}{(2\pi)^2} \frac{ie^{-ik'\cdot(\mathbf{x}_1-\mathbf{x}_2)}}{k'^2 - M^2} \quad (2.35)$$

are the Feynman propagators or two point Green functions [41, 43] for the real and complex fields, and $\mathbf{k} = (E_k, k)$ and $\mathbf{k}' = (E_{k'}, k')$. We can calculate the \mathbf{S} -matrix of $\psi\varphi \rightarrow \psi\varphi$ (meson–baryon scattering process) by picking up the second term of the R.H.S in equation (2.33). Thus, the \mathbf{S} -matrix in equation (2.32) becomes

$$\mathbf{S} = \frac{(ig)^2}{2} \int d^2\mathbf{x}_1 \int d^2\mathbf{x}_2 \langle p_3, p_4 | \mathcal{O} : \bar{\psi}(\mathbf{x}_1)\varphi(\mathbf{x}_1)\varphi(\mathbf{x}_2)\psi(\mathbf{x}_2) : | p_1, p_2 \rangle, \quad (2.36)$$

where

$$\mathcal{O} \equiv \langle 0|T(\psi(\mathbf{x}_1)\bar{\psi}(\mathbf{x}_2))|0\rangle,$$

is again the Feynman propagator, equation (2.35). We use the definition of φ in equation (2.5), ψ in equation (2.20), $\bar{\psi}$ in equation (2.21) and commutations relations in equations (2.14), (2.23), and $|p\rangle = \sqrt{2E_p} \hat{a}_p^\dagger |0\rangle$ to evaluate equation (2.36) as

$$\begin{aligned} \mathbf{S} &= \frac{(-ig)^2 \sqrt{16E_{p_1}E_{p_2}E_{p_3}E_{p_4}}}{2} \int d^2\mathbf{x}_1 \int d^2\mathbf{x}_2 \langle 0|a_{p_3}b_{p_4}(\bar{\psi}_+)_x \varphi(\mathbf{x}_2)\varphi(\mathbf{x}_1)(\psi_-)_{x_2} \mathcal{O} a_{p_1}^\dagger b_{p_2}^\dagger |0\rangle \\ &= \frac{(-ig)^2}{2} \int d^2\mathbf{x}_1 \int d^2\mathbf{x}_2 \left[(e^{i(\mathbf{p}_4-\mathbf{p}_1)\mathbf{x}_1} e^{i(\mathbf{p}_3-\mathbf{p}_2)\mathbf{x}_2} + e^{i(\mathbf{p}_4+\mathbf{p}_3)\mathbf{x}_1} e^{-i(\mathbf{p}_1+\mathbf{p}_2)\mathbf{x}_2}) + [\mathbf{x}_1 \leftrightarrow \mathbf{x}_2] \right] \mathcal{O}, \end{aligned}$$

where $\mathbf{p} = (E_p, p)$. In the second line of the \mathbf{S} -matrix, the $[\mathbf{x}_1 \leftrightarrow \mathbf{x}_2]$ terms double up with the others to cancel the factor of $1/2$ in front. Meanwhile, using equation (2.35), the \mathbf{x}_1 and \mathbf{x}_2 integrals give δ -functions for the momenta. We are left with the expression

$$\mathbf{S} = (-ig)^2 \int \frac{d^2\mathbf{k}'}{(2\pi)^2} \frac{i(2\pi)^4}{k'^2 - M^2} \left[\delta^2(\mathbf{p}_4 - \mathbf{p}_1 - \mathbf{k}') \delta^2(\mathbf{p}_3 - \mathbf{p}_2 + \mathbf{k}') \right. \\ \left. + \delta^2(\mathbf{p}_4 + \mathbf{p}_3 + \mathbf{k}') \delta^2(\mathbf{p}_1 + \mathbf{p}_2 - \mathbf{k}') \right].$$

Finally, we can trivially do the $d^2\mathbf{k}'$ integral using the δ -functions to get

$$\mathbf{S} = (-ig)^2 \left[\frac{i}{(\mathbf{p}_2 - \mathbf{p}_3)^2 - M^2} + \frac{i}{(\mathbf{p}_1 + \mathbf{p}_2)^2 - M^2} \right] (2\pi)^2 \delta^2(\mathbf{p}_1 + \mathbf{p}_2 - \mathbf{p}_3 - \mathbf{p}_4). \quad (2.37)$$

Since the \mathbf{S} -matrix reflects 2-momentum conservation, thus the \mathbf{S} -matrix should always contains a factor $\delta^2(\mathbf{p}_1 + \mathbf{p}_2 - \mathbf{p}_3 - \mathbf{p}_4)$. The invariant matrix element \mathcal{M} is defined by [1]

$$i\mathcal{M} = (-ig)^2 \left[\frac{i}{(\mathbf{p}_2 - \mathbf{p}_3)^2 - M^2} + \frac{i}{(\mathbf{p}_1 + \mathbf{p}_2)^2 - M^2} \right], \quad (2.38)$$

where

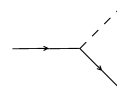
$$\mathbf{S} = i\mathcal{M} (2\pi)^2 \delta^2(\mathbf{p}_1 + \mathbf{p}_2 - \mathbf{p}_3 - \mathbf{p}_4).$$

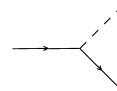
In the same way, we have calculated \mathcal{M} for the $\psi\varphi \rightarrow \psi\varphi$ process, we can calculate \mathcal{M} for the $\bar{\psi}\psi \rightarrow \varphi\varphi$ (baryon–antibaryon annihilation) process by picking up the third term in equation (2.33). For much simpler way, we instead use the Feynman rules (Appendix A.2) to calculate the \mathbf{S} -matrix for various processes, since our concern is to show the crossing symmetry in Feynman diagrams.

2.4.1 Feynman diagrams

The object that we really want to compute is the \mathbf{S} -matrix, since we are not interested in processes where no scattering occurs. The various terms in the perturbative expansion can be represented pictorially as follows

- i) We represent an external line for each particle in the initial state $|i\rangle$ and each particle in the final state $|f\rangle$. We choose dotted lines for mesons, and solid lines for baryons. We assign a directed momentum p_i (where $i = 1, 2, 3, 4$) to each line. Further, we add arrows to solid lines to denote their charges; we choose an incoming (outgoing) arrow in the initial state for ψ ($\bar{\psi}$). We choose the reverse convention for the final state, where an outgoing arrow denotes ψ .



- ii) We join the external lines together with trivalent vertices , corresponding to the terms in the expansion of \mathbf{S} . Thus the initial and final states are connected by an internal line with momentum k' , which obeys the conservation of momentum at each vertex.

Meson–baryon scattering

We use i) and ii) to draw all possible diagrams and apply Feynman rules in Appendix A.2 to the second term in equation (2.33). We get the two possible diagrams in Figure 2.1 for meson–baryon scattering process, where the virtual particle in these diagrams is

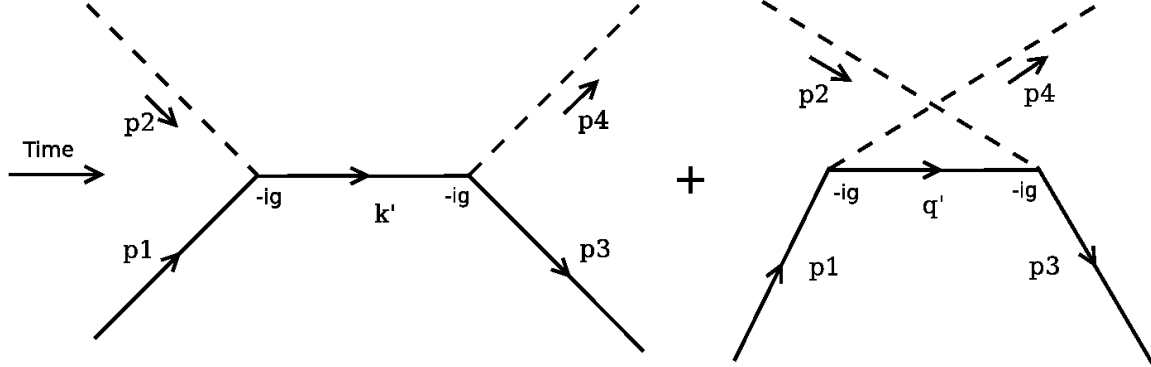


Figure 2.1: The two lowest order Feynman diagrams for meson–baryon scattering ($k' = p_1 + p_2 = p_3 + p_4$) and ($q' = p_1 - p_4 = p_3 - p_2$). The arrows on the dashed lines are to indicate the conservation of momentum.

the ψ and the \mathbf{S} -matrix is

$$\mathbf{S}_s = (-ig)^2 \left[\frac{i}{(\mathbf{p}_1 + \mathbf{p}_2)^2 - M^2} + \frac{i}{(\mathbf{p}_2 - \mathbf{p}_3)^2 - M^2} \right] (2\pi)^2 \delta^2(\mathbf{p}_1 + \mathbf{p}_2 - \mathbf{p}_3 - \mathbf{p}_4). \quad (2.39)$$

Here the subscript s refers to the scattering process. This agrees with the calculation in equation (2.38) that we performed earlier. The Mandelstam variables for this (scattering) process are given by

$$s_s = (\mathbf{p}_1 + \mathbf{p}_2)^2; \quad t_s = (\mathbf{p}_1 - \mathbf{p}_3)^2; \quad u_s = (\mathbf{p}_1 - \mathbf{p}_4)^2,$$

where s_s is the s -channel, t_s the t -channel and u_s the u -channel [1]. Note that $s_s + t_s + u_s = (m^2 + M^2)$. Thus, the invariant matrix element \mathcal{M} , in terms of Mandelstam variables, is

$$\mathcal{M}_s = (-ig)^2 \left[\frac{1}{s_s - M^2} + \frac{1}{u_s - M^2} \right]. \quad (2.40)$$

Baryon–antibaryon annihilation

For the baryon–antibaryon annihilation process, $\psi\bar{\psi} \rightarrow \varphi\varphi$, the Feynman diagrams are a little different. At lowest order, they are given by the diagrams of Figure 2.2. The virtual particle in these diagrams is ψ , as in the meson–baryon scattering. It is a simple matter to write down the \mathbf{S} -matrix using the Feynman rules in Appendix A.2,

$$\mathbf{S}_a = (-ig)^2 \left[\frac{i}{(\mathbf{p}_1 - \mathbf{p}_3)^2 - M^2} + \frac{i}{(\mathbf{p}_1 - \mathbf{p}_4)^2 - M^2} \right] (2\pi)^2 \delta^2(\mathbf{p}_1 + \mathbf{p}_2 - \mathbf{p}_3 - \mathbf{p}_4). \quad (2.41)$$

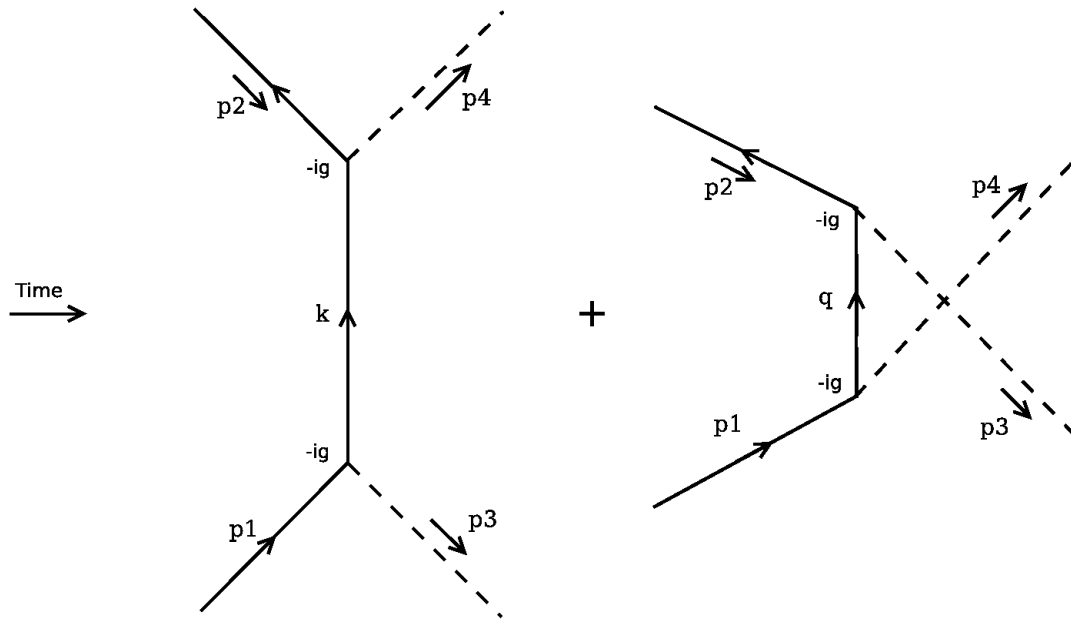


Figure 2.2: The two lowest order Feynman diagrams for baryon–antibaryon Annihilation ($k = p_1 - p_3 = p_2 - p_4$) and ($q = p_1 - p_4 = p_2 - p_3$).

Here the subscript a refers to the annihilation process. The Mandelstam variables for this (annihilation) process are given by

$$s_a = (\mathbf{p}_1 + \mathbf{p}_2)^2; \quad t_a = (\mathbf{p}_1 - \mathbf{p}_3)^2; \quad u_a = (\mathbf{p}_1 - \mathbf{p}_4)^2.$$

Thus, the invariant matrix element \mathcal{M} is

$$\mathcal{M}_a = (-ig)^2 \left[\frac{1}{t_a - M^2} + \frac{1}{u_a - M^2} \right]. \quad (2.42)$$

2.5 Crossing symmetry

The meson–baryon scattering in Figure 2.1 is different from the baryon–antibaryon annihilation in Figure 2.2. However, both invariant matrix elements of these figures arise from the same Lagrangian [41]. To change the meson–baryon matrix element in equation (2.39) into a baryon–antibaryon matrix element equation (2.41), we need only exchange the momenta \mathbf{p}_2 and $-\mathbf{p}_3$.

$$\mathbf{S}_s(\mathbf{p}_1, \mathbf{p}_2; \mathbf{p}_3, \mathbf{p}_4) = \mathbf{S}_a(\mathbf{p}_1, -\mathbf{p}_3; -\mathbf{p}_2, \mathbf{p}_4). \quad (2.43)$$

In other words, between equations (2.40) and (2.42), there is a permutation between the s and t channels as

$$\begin{aligned} \mathcal{M}_s(s_s, u_s) &= (-ig)^2 \left[\frac{1}{s_s - M^2} + \frac{1}{u_s - M^2} \right] \\ &= (-ig)^2 \left[\frac{1}{t_a - M^2} + \frac{1}{u_a - M^2} \right] \\ &= \mathcal{M}_a(t_a, u_a), \end{aligned} \quad (2.44)$$

where $s_s = (\mathbf{p}_1 + \mathbf{p}_2)^2 = (\mathbf{p}_1 - (-\mathbf{p}_3))^2 = t_a$ and \mathcal{M} is a function of s , t and u variables because of the momentum conservation. Graphically, this exchange switches an incoming with an outgoing line, changing at the same time the directions of their arrows. Equivalently, the truncated diagrams in Figures 2.1 and 2.2 are related by analytically continuing the momenta of equation (2.36). From equations (2.43) and (2.44) we conclude that this scalar theory \mathbf{S} -matrix element with a particle of momentum \mathbf{p}_i in the initial state is related to one with an antiparticle of momentum \mathbf{p}_f in the final state by simply changing \mathbf{p}_i to $-\mathbf{p}_f$ in the formula for the \mathbf{S} -matrix. This relation is known as crossing symmetry.

Chapter 3

Classical soliton models

We give a discussion of possible solutions of the φ^4 and sine-Gordon (s.G) models in (1+1) space-time dimensions. These relativistic classical nonlinear field models have attracted great attention due to their topological properties [4, 8, 45]. In classical nonlinear field theory, the dynamics of a single real scalar field $\varphi(t, x)$, that describes the solitary wave system is governed by the Lorentz-invariant Lagrangian density

$$\mathcal{L} = \frac{1}{2}\dot{\varphi}^2 - \frac{1}{2}\varphi'^2 - V(\varphi), \quad (3.1)$$

where the potential $V(\varphi)$ is any positive semidefinite function of φ , reaching a minimum value of zero for some value or values of φ . Application of the Euler-Lagrangian equation (2.2) to the Lagrangian equation (3.1) yields the equation of motion

$$\ddot{\varphi} - \varphi'' = -\frac{\partial V(\varphi)}{\partial \varphi}. \quad (3.2)$$

In this wave equation, the choice of $V(\varphi)$ is responsible for the nonlinearity. We use the energy-momentum tensor, equation (2.9), to get the total energy functional E as

$$E[\varphi] = \int_{-\infty}^{+\infty} dx \varepsilon(t, x) = \int_{-\infty}^{+\infty} dx \left[\frac{1}{2}\dot{\varphi}^2 + \frac{1}{2}\varphi'^2 + V(\varphi) \right], \quad (3.3)$$

where $\varepsilon(x)$ is the total energy density. This total energy E is conserved by equation (3.2), as the time (t) varies, under the condition $\dot{\varphi} \rightarrow 0$ and $\varphi' \rightarrow 0$ as $x \rightarrow \pm\infty$. Let $V(\varphi)$ have N absolute minima, which are also its zeros, so that

$$V(\varphi) = 0 \text{ and } V'(\varphi) = 0 \quad \text{for} \quad \varphi = g^{(i)}; \quad i = 1, \dots, N, \quad N \geq 1,$$

where $g^{(i)}$ are constant values of φ . This condition implies that $\dot{\varphi} \rightarrow 0$ and $\varphi' \rightarrow 0$. From the total energy definition, equation (3.3), the energy E is minimized when the field φ is constant in space-time and takes any one of these values. That is,

$$E[\varphi] = 0 \quad \text{if and only if} \quad \varphi = g^{(i)}; \quad i = 1, \dots, N.$$

According to the definition of a solitary wave for any static solution, the equation of motion (3.2) reduces to

$$\frac{\partial^2 \varphi}{\partial x^2} = \frac{\partial V}{\partial \varphi}. \quad (3.4)$$

This equation has a mechanical analogue, as pointed out in [8]. If we think of the variable x as ‘time’ and φ as the coordinate of a unit-mass point-particle, then equation (3.4) is just Newton’s second law for this particle’s motion of this analogue particle.

Now, since a solitary wave must have finite energy and a localized energy density, its field must approach one of the values $g^{(i)}$ as $x \rightarrow \pm\infty$. Subject to these boundary conditions, we can solve equation (3.4) for φ by multiplying equation (3.4) by φ' and integrating twice. We get

$$x - x_0 = \pm \int_{\varphi(x_0)}^{\varphi(x)} \frac{d\bar{\varphi}}{\sqrt{2V(\bar{\varphi})}}, \quad (3.5)$$

where x_0 , an integration constant, is any arbitrary point in space where the field has the value $\varphi(x_0)$. The solution $\varphi(x)$ can in principle be obtained by integrating equation (3.5) and inverting, for any $V(\varphi)$.

3.1 Kink-solution of φ^4 model

In φ^4 theory the potential function, known as a double well potential is of the form

$$V(\varphi) = \frac{1}{4}\lambda \left(\varphi^2 - \frac{m^2}{\lambda} \right)^2, \quad (3.6)$$

where λ and m^2 are positive constants (m is called the mass parameter of the field and λ is the coupling constant). This potential is plotted in Figure 3.1a and has two minima $\varphi = \pm \frac{m}{\sqrt{\lambda}}$ ($g^{(1)} = -\frac{m}{\sqrt{\lambda}}$ and $g^{(2)} = \frac{m}{\sqrt{\lambda}}$), which are related by reflection symmetry. Obviously this vacuum manifold has two-fold degeneracy. If we substitute this potential in equation (3.1), the Lagrangian density \mathcal{L} becomes

$$\mathcal{L} = \frac{1}{2}\dot{\varphi}^2 - \frac{1}{2}\varphi'^2 - \frac{1}{4}\lambda \left(\varphi^2 - \frac{m^2}{\lambda} \right)^2. \quad (3.7)$$

We apply the Euler-Lagrange equations (2.2) to this Lagrangian to get the equation of motion

$$\ddot{\varphi} - \varphi'' = m^2\varphi - \lambda\varphi^3. \quad (3.8)$$

This equation governs the dynamics of the solitary wave solution in the φ^4 model. As time t varies equation (3.8) conserves the total energy functional

$$E[\varphi] = \int_{-\infty}^{\infty} dx \varepsilon(t, x) = \int_{-\infty}^{\infty} dx \left[\frac{1}{2}\dot{\varphi}^2 + \frac{1}{2}\varphi'^2 + \frac{1}{4}\lambda \left(\varphi^2 - \frac{m^2}{\lambda} \right)^2 \right], \quad (3.9)$$

for any solution of equation (3.8).

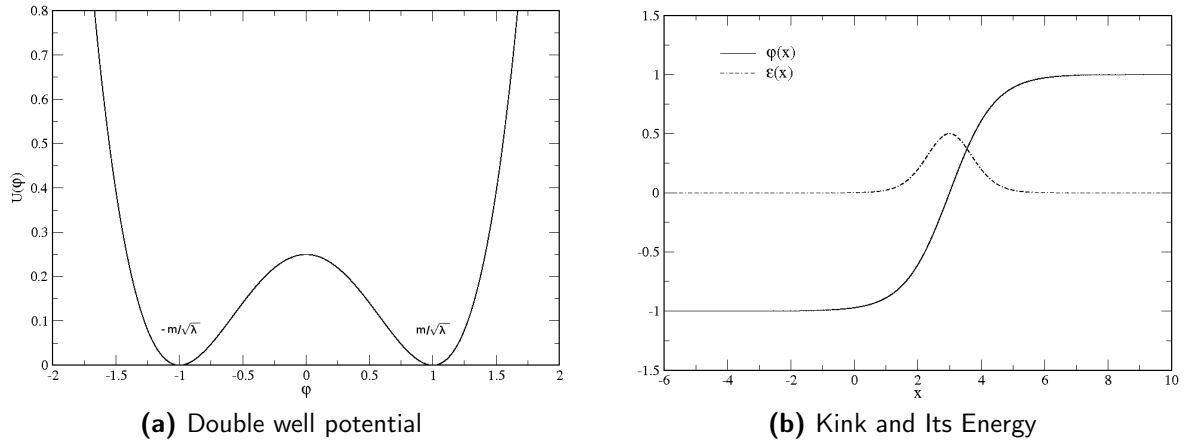


Figure 3.1: (a) The potential $V(\varphi)$ with two minima at $\varphi = \pm m/\sqrt{\lambda}$. (b) The solid line shows the static kink-solution (equation(3.12) with the plus sign), and the dashed line shows the energy density of the kink, all of them are localized at $x_0 = 3$ with $\lambda = m = 1$.

a) Static kink-solution

As we discussed earlier, the static form of equation (3.8), $\ddot{\varphi} = 0$, can be given by

$$\varphi'' = -m^2\varphi + \lambda\varphi^3. \quad (3.10)$$

This equation can be solved using equation (3.5) to give

$$x - x_0 = \pm \int_{\varphi(x_0)}^{\varphi(x)} \frac{d\bar{\varphi}}{\sqrt{\lambda/2}(\bar{\varphi}^2 - m^2/\lambda)}. \quad (3.11)$$

Choosing $\varphi(x_0) = 0$, integrating and inverting, we get

$$\varphi_{K(\bar{K})}(x) = \pm \frac{m}{\sqrt{\lambda}} \tanh \left[(m/\sqrt{2})(x - x_0) \right]. \quad (3.12)$$

The solution φ_K with the plus sign, plotted in Figure 3.1b, is called the static “kink” and $\varphi_{\bar{K}}$, with the minus sign, is called the static “antikink”. We substitute equation (3.12) into the total energy functional, equation (3.9), to get the energy density of the static kink- (or antikink-) solution [8],

$$\varepsilon(x) = (m^4/2\lambda) \operatorname{sech}^4 \left[(m/\sqrt{2})(x - x_0) \right], \quad (3.13)$$

which is plotted in Figure 3.1b and is localized near x_0 . Integrating this energy density over space, we get the total energy of the kink (or antikink), sometimes called the classical kink (or antikink) mass

$$M_{cl} = \int_{-\infty}^{+\infty} dx \varepsilon(x) = \frac{\sqrt{8} m^3}{3 \lambda}, \quad (3.14)$$

which is finite and does not depend on time.

b) Moving kink-solution

The moving kink (time-dependent) solution of equation (3.8) can be obtained either by Lorentz-transform of equation (3.8), transforming the coordinate variables in φ , or using the traveling wave solution method in Appendix A.3. This gives

$$\varphi_v(x, t) = \pm \frac{m}{\sqrt{\lambda}} \tanh \left[\frac{m}{\sqrt{2}} \left(\frac{x - vt}{\sqrt{1 - v^2}} \right) \right], \quad (3.15)$$

where the velocity $-1 < v < 1$. As we mentioned earlier the positive sign is for the moving kink and the negative sign is for the moving antikink. Furthermore, the total energy of the time-dependent solution is

$$\begin{aligned} E[\varphi_v] &= \int_{-\infty}^{\infty} dx \left[\frac{1}{2} \dot{\varphi}_v^2 + \frac{1}{2} \varphi_v'^2 + V(\varphi_v) \right] \\ &= \frac{\sqrt{8}m^3}{3\lambda} \frac{1}{\sqrt{1 - v^2}} = \frac{M_{cl}}{\sqrt{1 - v^2}}. \end{aligned} \quad (3.16)$$

This indicates the particle nature of the kink- (antikink-) solution, since $E[\varphi_v]$ is the Lorentz transform of the total energy of the static kink (antikink).

3.1.1 Small fluctuations approach

As shown in Figure 3.1a and discussed earlier, the potential equation (3.6) has two stable degenerate minima at $\varphi = \pm m/\sqrt{\lambda}$ (vacuum states). We assume that the system fluctuates by a small scalar field $\eta(t, x)$ around any of them. Then the scalar field will be given by

$$\varphi(t, x) = \frac{m}{\sqrt{\lambda}} + \eta(t, x) \quad \text{or} \quad \varphi(t, x) = -\frac{m}{\sqrt{\lambda}} + \eta(t, x), \quad (3.17)$$

where $\eta(t, x)$ is a small amplitude fluctuations with $|\eta| \ll \frac{m}{\lambda}$. We use equation (3.8) and equation (3.17) to get the equation of motion of the fluctuations $\eta(t, x)$,

$$\begin{aligned} \ddot{\eta} - \eta'' &= m^2(m/\sqrt{\lambda} + \eta) - \lambda(m/\sqrt{\lambda} + \eta)^3 \\ &= -2m^2\eta - 3m\sqrt{\lambda}\eta^2 - \lambda\eta^3. \end{aligned} \quad (3.18)$$

Since η is very small, more precisely $|\eta| \ll \frac{m}{\sqrt{\lambda}}$, $\eta^2 \rightarrow 0$ and $\eta^3 \rightarrow 0$, and the equation (3.18) can be rewritten as

$$\ddot{\eta} - \eta'' = -2m^2\eta. \quad (3.19)$$

This is the equation of motion for a Klein Gordon field¹ with mass $\sqrt{2} m$ and the plane wave

$$\eta_k(t, x) = B \exp i(kx - \omega t) + \tilde{B} \exp -i(kx - \omega t) \quad (3.20)$$

¹This equation describes the meson field about one of the trivial vacua in kink-theory of φ^4 model where $\sqrt{2} m$ is the mass of the meson [5].

is a solution for it, equation (3.19). Here $\omega = \omega(k)$ and k are the angular frequency and the wave number of $\eta_k(t, x)$, respectively, and B and \tilde{B} are the amplitudes of $\eta_k(t, x)$. Equation (3.19) is:

1. Linear. Any well-behaved localized function can be written by superposing waves of slightly different wavelengths in the form of Fourier analysis, *i.e.* plane waves (propagating along the x - axis) of different frequencies (or wavelengths) as

$$\eta(t, x) = \int_{-\infty}^{\infty} A(k) \exp \{i(kx - \omega t)\} dk. \quad (3.21)$$

Where $A(k)$ is given by the inverse formula.

2. Dispersive. The dispersion relation is given by

$$\omega(k) = \sqrt{k^2 + 2m^2}.$$

At time $t = 0$, the solution (3.21), abbreviating $\eta(0, x) \equiv \eta_0(x)$, can be rewritten as

$$\eta_0(x) = \int_{-\infty}^{\infty} A(k) e^{ikx} dk \quad (3.22)$$

and its inverse formula $A(k)$ as

$$A(k) = \frac{1}{2\pi} \int_{-\infty}^{\infty} \eta_0(x) e^{-ikx} dx. \quad (3.23)$$

Equations (3.22) and (3.23) show that $A(k)$ determines the initial wave function $\eta_0(x)$ and vice versa. We assume that the wave packet $\eta_0(x)$ is localized: $|\eta_0(x)|$ peaks at $x = 0$ and vanishes far away from $x = 0$. On the one hand, as $x \rightarrow 0$ we have $e^{ikx} \rightarrow 1$. On the other hand, far away from $x = 0$ the phase e^{ikx} goes through many periods, leading to destructive interference.

Gaussian wave packet

We assume that the amplitude $A(k)$ is a Gaussian function, plotted in Figure 3.2b, which is given by

$$A(k) = a_0 \exp \left\{ -(k - k_0)^2 / \sigma^2 \right\}. \quad (3.24)$$

where a_0 is a constant, k_0 is the average momentum, and σ is the width of the distribution. Therefore the wave-packet (3.21) becomes

$$\eta(t, x) = a_0 \int_{-\infty}^{\infty} \exp \left\{ -(k - k_0)^2 / \sigma^2 \right\} \exp \{i(kx - \omega(k)t)\} dk, \quad (3.25)$$

and its first derivative with respect to time t is given by

$$\dot{\eta}(t, x) = -ia_0 \int_{-\infty}^{\infty} \omega(k) \exp \left\{ -(k - k_0)^2 / \sigma^2 \right\} \exp \{i(kx - \omega(k)t)\} dk. \quad (3.26)$$

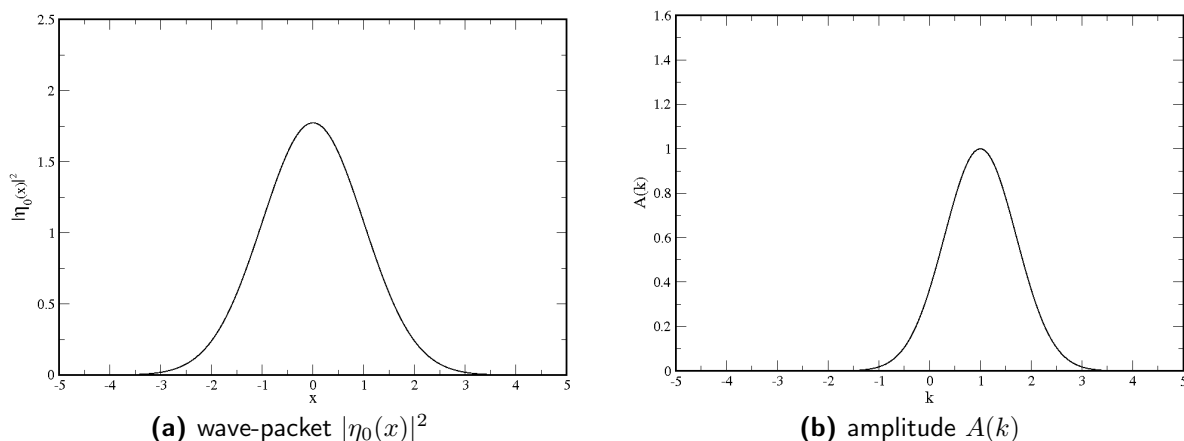


Figure 3.2: Two localized wave packets: $\eta_0(x) = \tilde{a}_0 \exp\{ixk_0 - x^2\sigma^2/4\}$ and $A(k) = a_0 \exp\{-(k - k_0)^2/\sigma^2\}$; they peak at $x = 0$ and $k = k_0$, respectively, and vanish far away. The graphs display the choice $\sigma = 1$, $a_0 = 1$ and $k_0 = 1$.

At time $t = 0$ the shape of this wave packet can be calculated by integrating over momentum space as

$$\eta_0(x) = a_0 \int_{-\infty}^{\infty} \exp\left\{-\frac{(k - k_0)^2 - ikx\sigma^2}{\sigma^2}\right\} dk \quad (3.27)$$

$$= \tilde{a}_0 \exp\{ixk_0 - x^2\sigma^2/4\}, \quad (3.28)$$

where $\tilde{a}_0 = \sqrt{\pi}\sigma a_0$ is a constant and $\eta_0(x)$ is plotted in Figure 3.2a.

3.2 Topological charges

Let the potential $V(\varphi)$ in equation (3.1) have a discrete number of degenerate absolute minima. We consider non-singular finite-energy solutions, such as solitary waves and solitons. Thus the field, whether static or time-dependent, must tend at any instant t to a minimum of $V(\varphi)$ at spatial infinity in order that the energy E in equation (3.3) be finite. In one space-dimension, spatial infinity consists of two points, $x \rightarrow \pm\infty$. First, we consider the field φ at $x \rightarrow +\infty$ and time $t = t_1$ to be

$$\lim_{x \rightarrow \infty} \varphi(t_1, x) \equiv \varphi_1, \quad (3.29)$$

where φ_1 is one of the minima of $V(\varphi)$. So, as time changes (either forward or backward, starting from t_1) the field $\varphi(t, x)$ will change continuously with t at every x as governed by the wave equation (3.2). In particular, $\varphi(t, \infty)$ will be some continuous function of t . On the other hand, since the energy of that solution is conserved and remains finite, $\varphi(t, \infty)$ must always be one of the minima of $V(\varphi)$, which fall into a discrete set. It cannot jump from φ_1 to another of the discrete minima if it is to vary continuously with t . Thus,

$\varphi(t, \infty)$ must remain stationary at φ_1 . Second, by the same arguments at $x \rightarrow -\infty$ and another time $t = t_2$ as

$$\lim_{x \rightarrow -\infty} \varphi(t_2, x) \equiv \varphi_2 \quad (3.30)$$

must also be time-independent and a minimum of $V(\varphi)$, but not necessarily the same as φ_1 in the case of degenerate minima. Therefore, we can divide the space of all finite-energy non-singular solutions into sectors, characterized by two indices, namely, the time-independent values of $\varphi(x = \infty)$ and $\varphi(x = -\infty)$. These sectors are topologically unconnected, in the sense that fields from one sector cannot be distorted continuously into another without violating the requirement of finite energy. In particular, since time evolution is an example of a continuous distortion, a field configuration from any one sector stays within that sector as time changes. Certainly, when $V(\varphi)$ has a unique minimum, there is only one permissible value for both $\varphi(\infty)$ and $\varphi(-\infty)$, thus only one sector of configurations exists.

Now, we consider the potential $V(\varphi)$ in equation (3.6) which has two degenerate minima, at $\varphi = \pm \frac{m}{\sqrt{\lambda}}$. Consequently, all finite-energy non-singular solutions of this system, whether static or time-dependent, fall into four topological sectors. These are characterized by the pairs of possible vacuum configurations $(-\frac{m}{\sqrt{\lambda}}, \frac{m}{\sqrt{\lambda}})$, $(\frac{m}{\sqrt{\lambda}}, -\frac{m}{\sqrt{\lambda}})$, $(-\frac{m}{\sqrt{\lambda}}, -\frac{m}{\sqrt{\lambda}})$ and $(\frac{m}{\sqrt{\lambda}}, \frac{m}{\sqrt{\lambda}})$, respectively, which represent the values of $(\varphi(x = -\infty), \varphi(x = +\infty))$. Thus, the kink, the antikink, and the trivial constant solutions $\varphi = \pm \frac{m}{\sqrt{\lambda}}$, are members of the four sectors, respectively. When a kink from the far left and an antikink from the far right approach one another, the field configuration belongs to the $(-\frac{m}{\sqrt{\lambda}}, -\frac{m}{\sqrt{\lambda}})$ sector. For this sector we present numerical solutions to the kink–antikink collisions in chapter 6. The resulting field configuration always stay in the $(-\frac{m}{\sqrt{\lambda}}, -\frac{m}{\sqrt{\lambda}})$ sector.

The “topological charge” is introduced as a topological degree, or generalized winding number of the field in refs.[8, 45]. It is defined as

$$\mathcal{Q} = \frac{\sqrt{\lambda}}{m} [\varphi(x = \infty) - \varphi(x = -\infty)]. \quad (3.31)$$

Therefore, the kink topological sector has $\mathcal{Q} = 2$, the antikink topological sector has $\mathcal{Q} = -2$, and the trivial topological sector has zero topological charge. This topological charge is associated with a conserved current

$$\mathcal{I}^\mu = \frac{\sqrt{\lambda}}{m} \epsilon^{\mu\nu} \partial_\nu \varphi, \quad (3.32)$$

where a covariant summation notation $\mu, \nu = 0, 1$ and

$$g_{\mu\nu} = \begin{pmatrix} 1 & 0 \\ 0 & -1 \end{pmatrix}_{\mu\nu}, \quad \epsilon_{\mu\nu} = \begin{pmatrix} 0 & 1 \\ -1 & 0 \end{pmatrix}_{\mu\nu}$$

has been used. Clearly

$$\partial_\mu \mathcal{I}^\mu = 0 \quad \text{and} \quad \mathcal{Q} = \int_{-\infty}^{\infty} dx \mathcal{I}_0, \quad (3.33)$$

where $\partial_\mu \mathcal{I}^\mu = 0$ arises from the symmetry of $\partial_\mu \partial_\nu$. We know that to the extent that the field φ is a measurable physical quantity, we need both $\varphi(\infty)$ and $\varphi(-\infty)$ to identify a topological sector, and not \mathcal{Q} alone. However, for cases where physical quantities depend only on differences in φ and not on the absolute value of φ , \mathcal{Q} becomes the sole relevant topological index. The adjective topological is sometimes bestowed on solitary waves which have $\mathcal{Q} \neq 0$.

We note that these topological indices are different from the more familiar conserved quantities like energy, momentum, charge etc. The latter, as is well known in classical and quantum field theory, can be traced to the existence of continuous symmetries of the Lagrangian, such as time translation, space translation, “internal groups” and equation of motion. By contrast, the topological indices are boundary conditions, conserved because of finiteness of energy. Indeed, in many cases, these indices are closely related to breaking of some symmetry. That is, suppose the Lagrangian and $V(\varphi)$ are invariant under some symmetry transformation acting on $\varphi(x)$. If $V(\varphi)$ has a unique minimum at some $\varphi = \varphi_0$, then φ_0 itself must remain invariant under that transformation. But in order to get non-trivial topological sectors, we need to have two or more degenerate minima. In that case, while the full set of minima is invariant under the transformation, each individual minimum need not be so. For instance, the system equation (3.6), which permits four topological sectors, has $V(\varphi)$ invariant under $\varphi \leftrightarrow -\varphi$. But its two minima, $\varphi = -\frac{m}{\sqrt{\lambda}}$ and $\varphi = +\frac{m}{\sqrt{\lambda}}$, are not separately invariant. Rather, they are transformed into one another. In general this feature, called “spontaneous symmetry breaking”, has great importance in the quantum theory, as well as the statistical mechanics of the field system [45, 8].

3.3 Soliton solution of sine-Gordon model

Earlier we examined the kink-solution, the solitary wave solution of the φ^4 system. However, this solution did not turn out to be a soliton solution². Here we look at a system in (1 + 1) space-time dimensions that admits a true soliton solution. The potential function is given by

$$U(\varphi) = \frac{m^4}{\lambda} \left(1 - \cos \left[(\sqrt{\lambda}/m)\varphi \right] \right), \quad (3.34)$$

which is periodic in φ . This potential is depicted by the solid line in Figure 3.3a and has an infinite series of minima:

$$\varphi_n = n \frac{2\pi m}{\sqrt{\lambda}}; \quad n = \dots, -2, -1, 0, 1, 2, \dots \quad (3.35)$$

In the weak field limit, where $|\varphi| \ll 1$, the sine-Gordon potential reduces to the Klein-Gordon potential

$$U_{KG}(\varphi) = \frac{m^2}{2} \varphi^2, \quad (3.36)$$

²We have emphasized in chapter 1 the difference between solitary wave and soliton solutions.

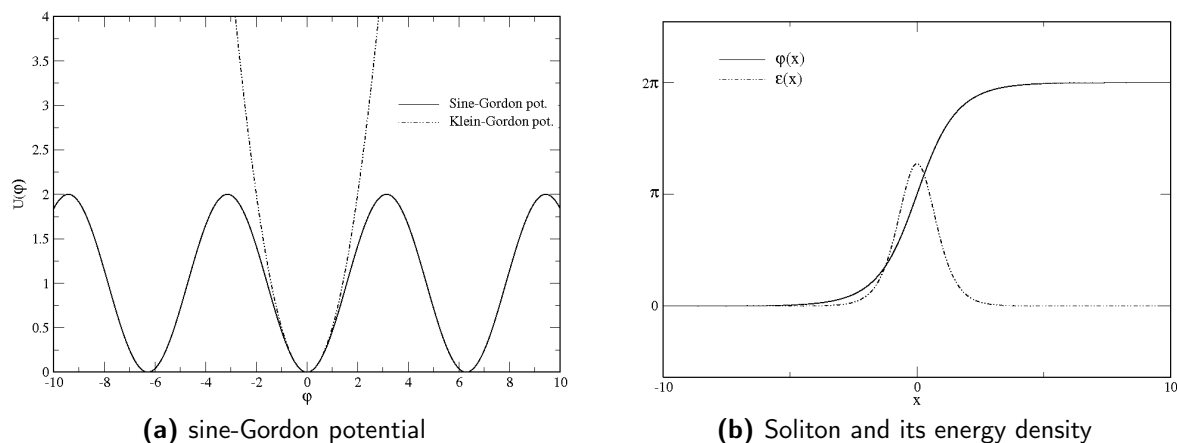


Figure 3.3: (a) The solid line shows the sine-Gordon potential $U(\varphi)$ with an infinite set of minima, and the dashed line shows the Klein-Gordon potential. (b) The solid line shows the static soliton solution (equation (3.43) with a plus sign), and the dashed line shows its energy density. The graphs are localized at $x_0 = 0$ and display the choice $\lambda = m = 1$.

which is depicted by the dashed line in Figure 3.3a. We substitute $U(\varphi)$ in equation (3.1) to get the sine-Gordon Lagrangian density

$$\mathcal{L} = \frac{1}{2} \partial_\mu \varphi \partial^\mu \varphi + \frac{m^4}{\lambda} \left(\cos \left[\left(\frac{\sqrt{\lambda}}{m} \right) \varphi \right] - 1 \right). \quad (3.37)$$

Changing variables to

$$x \rightarrow mx, \quad t \rightarrow mt \quad \text{and} \quad \varphi \rightarrow \frac{\sqrt{\lambda}}{m} \varphi,$$

the Lagrangian can be simplified to

$$\mathcal{L} = \frac{m^4}{\lambda} \left[\frac{1}{2} \partial_\mu \varphi \partial^\mu \varphi + (\cos(\varphi) - 1) \right]. \quad (3.38)$$

and the potential reads

$$U(\varphi) = \frac{m^4}{\lambda} (\cos(\varphi) - 1). \quad (3.39)$$

We apply the Euler-Lagrange equations (2.2) to the Lagrangian equation (3.38) to get the sine-Gordon equation of motion

$$\ddot{\varphi} - \varphi'' + \sin(\varphi) = 0. \quad (3.40)$$

The conserved functional energy is

$$E[\varphi] = \frac{m^3}{\lambda} \int_{-\infty}^{\infty} dx \left[\frac{1}{2} \dot{\varphi}^2 + \frac{1}{2} \varphi'^2 + (1 - \cos(\varphi)) \right]. \quad (3.41)$$

We can see that the Lagrangian equation (3.38) and the field equation (3.40) are symmetric under reflection, $\varphi(x, t) \rightarrow -\varphi(x, t)$, and translation, $\varphi(x, t) \rightarrow \varphi + 2n\pi$. Consistent with these symmetries, the energy E vanishes at the absolute minima of $(1 - \cos \varphi)$, which are $\varphi(x, t) = 2n\pi$.

a) Static soliton solution

In the static case ($\ddot{\varphi} = 0$) the equation of motion, (3.40), becomes

$$\varphi'' = \sin(\varphi). \quad (3.42)$$

It can be solved using equation (3.5) to give

$$x - x_0 = \pm \int_{\varphi(x_0)}^{\varphi(x)} \frac{d\bar{\varphi}}{2 \sin(\bar{\varphi}/2)},$$

where we have used $1 - \cos(z) = 2 \sin^2(z/2)$. Choosing $\varphi(x_0) = 0$, integrating and inverting, we get

$$\varphi_{S(\bar{s})}(x) = \pm 4 \arctan(e^{x-x_0}). \quad (3.43)$$

The solution φ_S with the plus sign, plotted in Figure 3.3b, is called the static “soliton” and the one $\varphi_{\bar{S}}$ with the minus sign is called the static “antisoliton”. The energy density of the static soliton (antisoliton) solution is

$$\varepsilon(x) = \frac{2m^3}{\lambda} [1 - \cos(4 \arctan\{e^{x-x_0}\})], \quad (3.44)$$

which is plotted in Figure 3.3b. It is localized near x_0 . The solution (3.44) is roughly similar in shape to the “kink” discussed earlier, although the function is different in detail. The total energy of the soliton (antisoliton) solution, equation (3.43), can be calculated by integrating equation (3.44) over space, giving

$$M_s = \frac{8m^3}{\lambda}. \quad (3.45)$$

b) Moving soliton solution

The moving soliton (time-dependent) solution of equation (3.40) can again be obtained either by Lorentz-transforming equation (3.40), transforming the coordinate variables in φ , or by using the traveling wave solution in Appendix A.4. This gives

$$\varphi_v(x, t) = \pm 4 \arctan\left(e^{\frac{x-x_0-vt}{\sqrt{1-v^2}}}\right), \quad (3.46)$$

where the velocity $-1 < v < 1$, and as we have seen earlier the positive sign is for the moving soliton and the negative sign for the moving antisoliton. Again, the total energy of this solution can be obtained by substituting equation (3.46) into equation (3.41) and integrating over space. We get

$$\begin{aligned} E_s[\varphi_v] &= \int_{-\infty}^{\infty} dx \left[\frac{1}{2} \dot{\varphi}_v^2 + \frac{1}{2} \varphi_v'^2 + (1 - \cos(\varphi_v)) \right] \\ &= \frac{8m^3}{\lambda} \frac{1}{\sqrt{1-v^2}} = \frac{M_s}{\sqrt{1-v^2}}. \end{aligned} \quad (3.47)$$

Topological Charges

According to our earlier discussion of topological charges in section 3.2, all finite configurations can be divided into an infinite number of topological sectors, each characterized by a conserved pair of integer indices (n_1, n_2) corresponding to the asymptotic field values

$$\lim_{x \rightarrow -\infty} \varphi(x, t) \equiv \varphi(-\infty) = 2n_1\pi \quad ; \quad \lim_{x \rightarrow +\infty} \varphi(x, t) \equiv \varphi(+\infty) = 2n_2\pi.$$

So the topological charge is defined as [8]

$$\mathcal{Q} = \frac{1}{2\pi}(\varphi(-\infty) - \varphi(+\infty)) = n_1 - n_2 = \frac{1}{2\pi} \int_{-\infty}^{+\infty} dx \frac{\partial \varphi}{\partial x}. \quad (3.48)$$

Thus, the topological charge is $\mathcal{Q} = 1$ for the soliton solution and $\mathcal{Q} = -1$ for the antisoliton solution. The soliton and the antisoliton are not the only solutions of the sine-Gordon equation. There are other solutions corresponding to multi-soliton (multi-antisoliton) states. The existence of these solutions is a peculiar property of the sine-Gordon model (there are no exact multi-soliton solutions in the φ^4 model). It turns out that there exists a method for solving the sine-Gordon equation, known as Bäcklund transformations [17], which give an exact solution for the soliton–antisoliton interaction solution,

$$\varphi_{S\bar{S}}(t, x) = 4 \arctan \left[\frac{\sinh(vt/\sqrt{1-v^2})}{v \cosh(x/\sqrt{1-v^2})} \right], \quad (3.49)$$

where v is the asymptotic velocity of each soliton. In this case the field configuration, plotted in Figure 3.4a, always stays in the trivial topological sector. This solution has an asymptotic behavior in time ($t \rightarrow -\infty$) [8]

$$\begin{aligned} \lim_{t \rightarrow \mp\infty} \varphi_{S\bar{S}}(t, x) &\xrightarrow{t \rightarrow \mp\infty} 4 \arctan \left[e^{\left(\frac{x+v(t \pm \Delta t/2)}{\sqrt{1-v^2}} \right)} \right] - 4 \arctan \left[e^{\left(\frac{x-v(t \pm \Delta t/2)}{\sqrt{1-v^2}} \right)} \right] \\ &= \varphi_S \left(\frac{x+v(t \pm \Delta t/2)}{\sqrt{1-v^2}} \right) + \varphi_{\bar{S}} \left(\frac{x-v(t \pm \Delta t/2)}{\sqrt{1-v^2}} \right), \end{aligned} \quad (3.50)$$

where

$$\Delta t = \frac{1-v^2}{v} \ln v \quad (3.51)$$

is the time delay for the soliton and the antisoliton to pass through each other. Thus equation (3.50) corresponds at very early times to a soliton and an antisoliton far apart and approaching each other with relative velocity v , plotted in Figure 3.4a as the line with time $t = -50$. As they approach one another, they tend to annihilate each other until $t = 0$, plotted in Figure 3.4a, when the field vanishes everywhere. But at very late times ($t \rightarrow \infty$), plotted in Figure 3.4a as the line with $t = 50$, the field reemerges and asymptotically grows and separates into the same soliton–antisoliton pair, with the

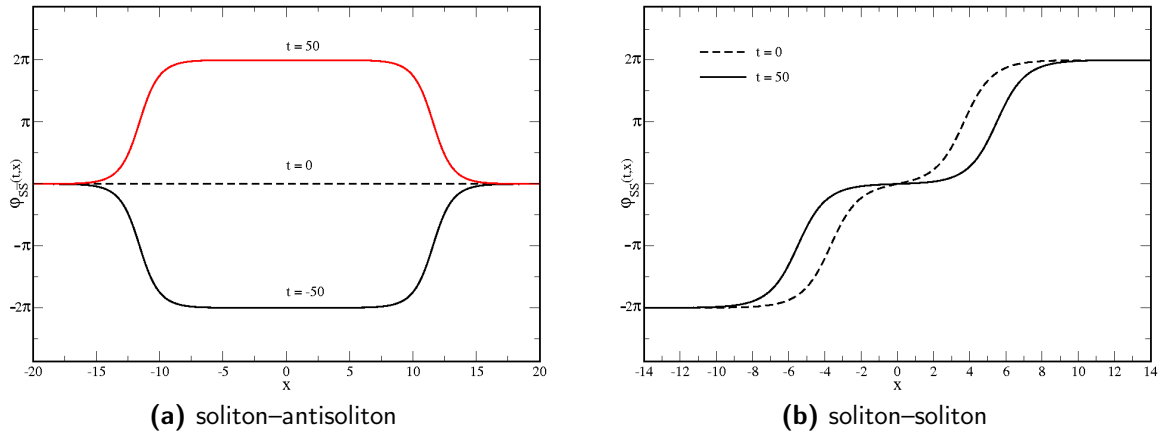


Figure 3.4: (a) and (b) are the field configurations of the soliton-antisoliton $\varphi_{S\bar{S}}$ and the soliton-soliton φ_{SS} solutions at different times.

same shapes and velocities. The only change is in the phase $\Delta t \rightarrow -\Delta t$, as indicated in equation (3.50). The time delay is negative, so a soliton and an antisoliton attract each other. If we take the v to be purely imaginary as iv and $(t, x) \rightarrow (it, ix)$, equation (3.49) becomes

$$\varphi_B(t, x) = 4 \arctan \left[\frac{\sin (vt/\sqrt{1+v^2})}{v \cosh (x/\sqrt{1+v^2})} \right], \quad (3.52)$$

which is a bound state solution of a soliton-antisoliton pair, known as the doublet or the breather solution. This breather solution is periodic with period $\tau = \frac{2\pi\sqrt{1+v^2}}{v}$. In this case the soliton and the antisoliton are separated at very early times. But after they interact with each other they fall in a bound state of the soliton-antisoliton pair and never fully retain their original shapes and oscillate about each other, instead of separating arbitrarily far apart. Again, the Bäcklund transformations give an exact solution for the soliton-soliton interaction solution [8], which is given by

$$\varphi_{SS}(t, x) = 4 \arctan \left[\frac{v \sinh (x/\sqrt{1-v^2})}{\cosh (vt/\sqrt{1-v^2})} \right]. \quad (3.53)$$

This solution is depicted in Figure 3.4b. The field configuration belongs to the topological sector $\mathcal{Q} = 2$ and goes from -2π to 2π as x goes from $-\infty$ to ∞ . In equation (3.53), the two solitons at very early times approach each other with the same speeds, but with time delay Δt given by equation (3.51) [8]. As they approach one another, they tend to repel each other until $t = 0$, plotted in Figure 3.4b. At very late times, plotted in Figure 3.4a as the line with $t = 50$, the two solitons bounce back with velocities equal and opposite to their initial velocities, plotted in Figure 3.4b. This is a case of backward scattering.

Chapter 4

Scattering off solitary waves

In the previous chapter we have mostly dealt with the solutions of the φ^4 and sine-Gordon models in isolation. However, in any real system, there are variety of these solutions, in addition to small amplitude fluctuations (particles) of the fields. The interactions of these solutions with small amplitude fluctuations play a crucial role in the evolution of the system. We use the small amplitude fluctuation approach to study the bound and scattering states of the kink (soliton) solutions. The perturbative expansion about the trivial solution of φ^4 model has already been discussed in section 3.1.1, showing that the fluctuations about the trivial solutions describe bosons of mass $\sqrt{2}m$ [5, 7]. In the next two sections we discuss the eigenfunctions and eigenvalues of the scattering states of the nontrivial solutions of the φ^4 and the sine-Gordon models. They are followed by the derivation of the phase shifts. In the last section we discuss and summarize the deformed kink-solution, which has a decomposition as a single kink plus radiation with two discrete modes and one continuum mode [5, 46, 47].

4.1 Scattering off the kink solution

We recall our discussion of the nonperturbative static kink solution $\varphi_K(x)$, equation (3.12), whose dynamics are governed by the Lagrangian density, equation (3.7). We consider small amplitude fluctuations $\eta(x, t)$ about this kink configuration $\varphi_K(x)$ by parameterizing the field variable as

$$\varphi(x, t) = \varphi_K(x) + \eta(x, t), \quad (4.1)$$

for $|\eta| \ll \langle \varphi \rangle$, where $\langle \varphi \rangle$ is the vacuum expectation value of $\varphi(x, t)$. While $\eta(x, t)$ is very small, the dynamics of the field $\varphi(x, t)$ are still governed by the Lagrangian density, equation (3.7). We expand the Lagrangian density, equation (3.7), to quadratic order in η around the kink configuration φ_K . Thus the Lagrangian becomes a function of the perturbation η around the kink configuration, $\mathcal{L}(\varphi) = \mathcal{L}(\varphi_K + \eta) = \tilde{\mathcal{L}}(\eta)$. Application of the Euler-Lagrangian equations (2.2) to this Lagrangian yields the equation of motion

for small amplitude fluctuations $\eta(x, t)$ about the kink solution

$$\ddot{\eta} - \eta'' + \left[2m^2 - 3m^2 \operatorname{sech}^2 \left(\frac{m}{\sqrt{2}}(x - x_0) \right) \right] \eta = 0,$$

or

$$\ddot{\eta} - \eta'' + [M^2 + U_2(x)] \eta = 0. \quad (4.2)$$

where $\ddot{\eta}$ and η'' are the second derivatives of $\eta(x, t)$ with respect to the time t and position x , respectively. This is just a Schrödinger equation with the potential

$$U_2(x) = -\frac{3M^2}{2} \operatorname{sech}^2 \left[\frac{Mx}{2} \right], \quad (4.3)$$

where $M^2 = 2m^2$. This potential is the $l = 2$ case of the Pöschl-Teller family of exactly solvable potentials [48],

$$U_l(x) = -\frac{(l+1)M^2}{l} \operatorname{sech}^2 \left[\frac{Mx}{l} \right], \quad (4.4)$$

where $l = 0, 1, 2, 3, \dots$ and $l \rightarrow 0$ yields the free theory $U_0(x) = 0$, *i.e.* the free Klein-Gordon field with mass $M = \sqrt{2}m$ in section 3.1.1. These potentials, equation (4.4), are symmetric and reflectionless. The corresponding bound and scattering state wavefunctions of equation (4.2) are known explicitly [7]. Since the potential, equation (4.3), is symmetric ($U_l(-x) = U_l(x)$), the 2×2 \mathbf{S} -matrix for the symmetric and antisymmetric channels is diagonal. Furthermore, it is required from the reflectionlessness of the potential that the 2×2 \mathbf{S} -matrix is proportional to the identity matrix, cf. chapter XVII of [49].

To solve equation (4.2) and find its eigenfunctions, we take $\eta(x, t) = e^{-i\omega t} \eta_k(x)$. The corresponding eigenfunctions of equation (4.2) are

$$\eta_0(x) = \sqrt{\frac{3M}{8}} \operatorname{sech}^2 \left[\frac{Mx}{2} \right], \quad (4.5)$$

$$\eta_1(x) = \sqrt{\frac{3M}{4}} \sinh \left[\frac{Mx}{2} \right] \operatorname{sech}^2 \left[\frac{Mx}{2} \right]. \quad (4.6)$$

These are discrete bound states with eigenvalues $\omega_0^2 = 0$ and $\omega_1^2 = \frac{3M^2}{4}$, respectively. The solution in equation (4.5) is called the translational (zero) mode because it is the small amplitude fluctuations of the translation of the kink that costs the kink zero energy [5]. The solution in equation (4.6) is called the shape mode (excited bound state). These solutions are followed by two linearly independent continuum solutions for each $k > 0$ [7],

$$\eta_k^r(x) = [\eta_k^l]^*(x) = \frac{M^2 e^{ikx}}{\omega \sqrt{4k^2 + M^2}} \left[\frac{3}{2} \tanh^2 \left(\frac{Mx}{2} \right) - \frac{1}{2} - \frac{2k^2}{M^2} - i \frac{3k}{M} \tanh \left(\frac{Mx}{2} \right) \right], \quad (4.7)$$

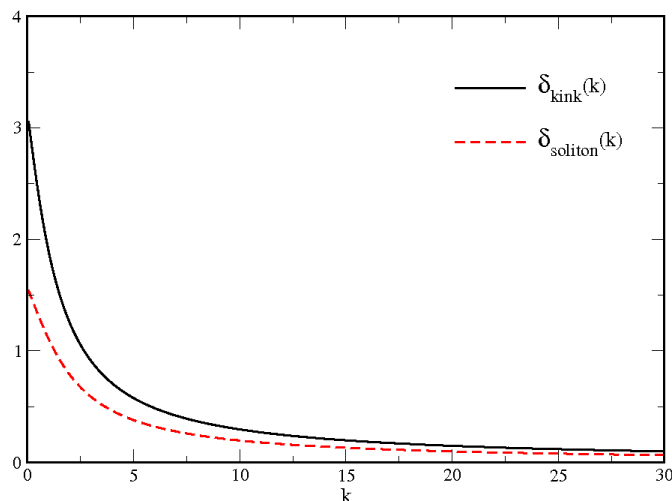


Figure 4.1: The solid (dashed) line depicts the phase shift of scattering states of the kink (soliton) solution.

corresponding to the right- and left-moving scattering waves, respectively, with wave number k and eigenvalues $\omega^2 = k^2 + M^2$. These fluctuations, equations (4.5), (4.6) and (4.7), are orthogonal and normalized such that

$$\int dx \eta_0(x)^2 = 1, \quad \text{and} \quad \int dx \eta_1(x)^2 = 1 \quad (4.8)$$

and

$$\int dx \eta_k(x) \eta_{k'}^*(x) = 2\pi \delta(k - k') \quad (4.9)$$

The asymptotic form of the continuum states, equation (4.7), is given by

$$\eta_k(x) \xrightarrow{x \rightarrow \pm\infty} \frac{M^2 C^\pm(k) e^{ikx}}{\omega \sqrt{4k^2 + M^2}} = \frac{M^2 |C^\pm|}{\omega \sqrt{4k^2 + M^2}} e^{i(kx + \delta_{kink}^\pm(k))}, \quad (4.10)$$

where $C^\pm = \left(1 - \frac{2k^2}{M^2} \mp i\frac{3k}{M}\right)$ and δ_{kink}^\pm is the phase shift of the right moving scattering states off the kink-solution, plotted in Figure 4.1. For $x \rightarrow \pm\infty$, δ_{kink}^\pm is given by [7]

$$\delta_{kink}^\pm(k) = \pm \arctan\left(\frac{3kM}{2k^2 - M^2}\right). \quad (4.11)$$

Again, the left moving scattering states have the same phase shift in equation (4.11).

4.2 Scattering off the soliton solution

Next we apply the small amplitude fluctuations approach to the soliton solution of the sine-Gordon model, equation (3.43). We can repeat the same analysis from the previous

section by replacing the kink-solution with the soliton solution so that the parameterized field variable becomes $\varphi(x, t) = \varphi_S(x) + \eta(x, t)$. We expand the Lagrangian density, equation (3.38), to quadratic order in η around the soliton configuration φ_S . This yields the equation of motion for the small amplitude fluctuations $\eta(x, t)$

$$\ddot{\eta} - \eta'' + \left[M^2 - 2M^2 \operatorname{sech} \left(\frac{M}{2}(x - x_0) \right) \right] \eta = 0 \quad (4.12)$$

about the soliton solution. The potential here is the $l = 1$ case of the Pöschl-Teller family [48]. Again, we take $\eta(x, t) = e^{-i\omega t} \eta_k(x)$ to solve equation (4.12). In this case the corresponding eigenfunctions are a single zero mode (bound state) [7]

$$\eta_0(x) = \sqrt{\frac{M}{2}} \operatorname{sech}^2 [Mx], \quad (4.13)$$

with eigenvalue $\omega_0^2 = 0$ and the scattering states

$$\eta_r(x) = \eta_l^*(x) = \frac{e^{ikx}}{\omega} [k + iM \tanh(Mx)], \quad (4.14)$$

corresponding to the right- and the left-moving waves, respectively, with wave number k and eigenvalues $\omega^2 = k^2 + M^2$. The asymptotic form of these continuum states is given by

$$\eta_k(x) \xrightarrow{x \rightarrow \pm\infty} \frac{|C^\pm|}{\omega} e^{i(kx + \delta_{soliton}^\pm(k))}, \quad (4.15)$$

where $\delta_{soliton}^\pm$ is the phase shift of the right moving scattering states off the soliton solution, plotted in Figure 4.1. It is given by [7]

$$\delta_{soliton}^\pm(k) = \pm \arctan \left(\frac{M}{k} \right). \quad (4.16)$$

Again, the \pm sign refer to $x \rightarrow \pm\infty$ and the left moving scattering states have the same phase shift as in equation (4.16).

4.3 Deformed kink-solution

It has been shown in earlier studies [5] that the nonperturbative kink solution in both its static, equation (3.12), and moving, equation (3.15), forms does not emit radiation unless some external force acts on it. The action of the external force accelerates the kink-solution and deforms its shape. The deformed kink-solution emits radiation in the form of scalar particles [50, 51]. In ref.[52], the emitted radiation was estimated numerically in (3 + 1) space-time dimensions. A bit later, in refs.[5, 46, 47], analytical discussion of this emitted radiation was introduced. Here, we extend earlier studies seeking to discuss the modes of the emitted radiation, their normalization constants and the scattering amplitude of the scattering modes.

We consider small amplitude fluctuations $\xi(x, t)$ about the moving kink-solution $\varphi_K(x, t)$ to describe the emitted radiation from the deformed moving kink-solution. The latter is defined as

$$\varphi(x, t) = \varphi_K(x, t) + \xi(x, t). \quad (4.17)$$

As been discussed in section 4.1, the equation of motion for the small-amplitude fluctuations (emitted radiation) $\xi(x, t)$ can be given by

$$\left[\partial_t^2 - \partial_x^2 + M^2 - U_2 \left(\frac{x - vt}{\sqrt{1 - v^2}} \right) \right] \xi(x, t) = 0. \quad (4.18)$$

Since $\partial_t^2 - \partial_x^2$ is invariant under the Lorentz transformations

$$\begin{pmatrix} \tau \\ Z \end{pmatrix} = \gamma \begin{pmatrix} 1 & -v \\ -v & 1 \end{pmatrix} \begin{pmatrix} t \\ x \end{pmatrix}; \quad \text{and} \quad \gamma = \frac{1}{\sqrt{1 - v^2}}. \quad (4.19)$$

Equation (4.18) simplifies to

$$[\partial_\tau^2 - \partial_Z^2 + M^2 - U_2(Z)] \bar{\xi}(Z, \tau) = 0, \quad (4.20)$$

where $\bar{\xi}(Z, \tau) = \xi(L^{-1}(Z, \tau)) = \xi(x, t)$ and L^{-1} is the inverse of Lorentz transform. Solutions of equation (4.20) have already been discussed in section 4.1. Here we define the emitted radiation $\bar{\xi}(Z, t)$ from the deformed moving kink-solution as a linear combination of these solutions (of equation (4.20))

$$\begin{aligned} \bar{\xi}(Z, \tau) = & a_0 \eta_0(Z) + [a_1 \eta_1(Z) e^{-i\omega_1 \tau} + \bar{a}_1 \eta_1(Z) e^{i\omega_1 \tau}] \\ & + \int dk [a(k) \eta_k(Z) e^{-i\omega_k \tau} + \bar{a}(k) \eta_k^*(Z) e^{i\omega_k \tau}], \end{aligned} \quad (4.21)$$

where η_0 , η_1 and η_k are given by equations (4.5), (4.6) and (4.7), respectively, a_0 is the amplitude of the η_0 modes, a_1 and \bar{a}_1 are the amplitudes of the η_1 modes, and $a(k)$ and $\bar{a}(k)$ are the amplitudes of the η and η^* modes, respectively. We utilize the orthogonal property between η_0 , η_1 and $\eta_k \neq \eta_k^*$ modes, equations (4.8) and (4.9), to find these amplitudes. Therefore we can write the amplitude a_0 as

$$a_0 = \int dZ \bar{\xi}(Z, \tau) \eta_0(Z) \quad (4.22)$$

and the amplitudes a_1 and \bar{a}_1

$$\begin{aligned} a_1 &= \frac{1}{2} \int dZ \left[\bar{\xi}(Z, \tau) + \frac{i}{\omega_1} \dot{\bar{\xi}}(Z, \tau) \right] \eta_1(Z) e^{i\omega_1 \tau}, \\ \bar{a}_1 &= \frac{1}{2} \int dZ \left[\bar{\xi}(Z, \tau) - \frac{i}{\omega_1} \dot{\bar{\xi}}(Z, \tau) \right] \eta_1(Z) e^{-i\omega_1 \tau}, \end{aligned} \quad (4.23)$$

where $\dot{\bar{\xi}}(Z, \tau) = \frac{d}{d\tau} \bar{\xi}(Z, \tau)$. Finally, the scattering amplitudes $a(k)$ and $\bar{a}(k)$ are

$$a(k) = \frac{e^{i\omega_k \tau}}{4\pi} \int dZ \left[\bar{\xi}(Z, \tau) + \frac{i}{\omega_k} \dot{\bar{\xi}}(Z, \tau) \right] \eta_k^*(Z) \quad (4.24)$$

and

$$\bar{a}(k) = \frac{e^{-i\omega_k \tau}}{4\pi} \int dZ \left[\bar{\xi}(Z, \tau) - \frac{i}{\omega_k} \dot{\bar{\xi}}(Z, \tau) \right] \eta_k(Z). \quad (4.25)$$

Chapter 5

Scattering a wave packet off a kink solution

So far we have dealt with the classical kink solution and solved the small fluctuation problem about it. However, the solution of the small fluctuations approach was considered by neglecting the nonlinear terms in equation (3.8). In this sector, the nontrivial topological sector, we present numerical solutions. We solve the time-dependent equation of motion of φ^4 theory, equation (3.8), for two distinct initial conditions: the wave packet in a trivial vacuum background and in the background of the kink solution. At very late times we extract the phase shift of the scattering waves and compare it to the result from static potential scattering, equation (4.11). We study the nonlinear effects of φ^4 model, by varying the size of the initial wave packet until the nonlinear terms in equation (3.8) become active. At that moment the kink will be dragged and deformed by the wave packet. The study of this chapter is based on ref.[31].

5.1 Wave packet and background

We consider a wave packet, equation (3.21), at $t = 0$,

$$\eta_{\text{wp}}(x) = \int_{-\infty}^{\infty} dk A(k) e^{ikx}, \quad (5.1)$$

which is a linear combination of plane waves. This wave packet is localized near $x = 0$ and satisfies the Klein–Gordon dispersion relation, $\omega_k = \sqrt{k^2 + M^2}$. The dispersion relation enters only via the velocity of the initial wave packet,

$$\dot{\eta}_{\text{wp}}(x) = -i \int_{-\infty}^{\infty} dk \omega_k A(k) e^{ikx}. \quad (5.2)$$

In the context of our numerical simulations we assume the spectral function $A(k)$ in momentum space to be of Gaussian shape, equation (3.24). Since the equation of motion is second order in time, we have determined the initial conditions for the wave packet in

equations (5.1) and (5.2). First, we consider the initial configuration

$$\varphi(x, 0) = \frac{M}{\sqrt{2\lambda}} + \eta_{\text{wp}}(x) \quad \text{and} \quad \left. \frac{\partial \varphi(x, t)}{\partial t} \right|_{t=0} = \dot{\eta}_{\text{wp}}(x) \quad (5.3)$$

for the wave packet with zero topological charge in the vacuum background. We feed it into the equation of motion, equation (3.8). Since the velocity $\dot{\eta}_{\text{wp}}(x)$ is characterized by the dispersion relation extracted from equation (3.8), the superposition

$$\varphi(x, t) \simeq \frac{M}{\sqrt{2\lambda}} + a_0 \int_{-\infty}^{\infty} dk e^{-(k-k_0)^2/\sigma^2} e^{i(kx - \omega_k t)} \quad (5.4)$$

is an approximate solution as long as a_0 is small enough to neglect $\mathcal{O}(\eta_{\text{wp}}^2)$ terms in the equation of motion, which defines the small amplitude approximation, as in section 3.1.1. As we increase a_0 nonlinear effects emerge and the solution to the differential equation will no longer be a superposition of plane waves. We use this line of argument to study the nonlinear effects in subsection 5.2.4. Assume $\varphi(x, t_f)$ is the (numerical) solution to the equation of motion that emerges from the initial condition defined above. Then the deviation of the Fourier transform

$$\tilde{\varphi}_{t_f}(k) = \frac{e^{i\omega_k t_f}}{A(k)} \int_{-\infty}^{\infty} \frac{dx}{2\pi} e^{-ikx} \left[\varphi(x, t_f) - \frac{M}{\sqrt{2\lambda}} \right] \quad (5.5)$$

from unity measures nonlinear effects for times $t_f \gg 0$. Second, for the wave packet with unit topological charge in the kink background, we consider the initial configuration

$$\varphi(x, 0) = \varphi_{\text{K}}(x - x_0) + \eta_{\text{wp}}(x), \quad (5.6)$$

where x_0 is the position of the center of the kink solution. It must be taken large enough to avoid any overlap between the kink and the wave packet at $t = 0$ in order to define the scattering problem. For scattering to occur, the signs of x_0 and k_0 must coincide, since otherwise the wave packet will propagate away from the kink.¹ Since the kink is static, the initial velocity is as in equation (5.2). Any non-zero velocity of the kink can eventually be compensated by an appropriate Lorentz transformation [8]. At very late times we can give an analytic expression for the solution to this initial condition, provided we omit $\mathcal{O}(\eta_{\text{wp}}^2)$ terms in the small amplitude approximation,

$$\varphi(x, t) = \varphi_{\text{K}}(x - x_0) + \eta_{\text{wp}}^{(S)}(x, t), \quad (5.7)$$

where

$$\eta_{\text{wp}}^{(S)}(x, t) = \int_{-\infty}^{\infty} dk A(k) \exp[i(kx - \omega_k t + \delta(k))], \quad (5.8)$$

which is the scattered wave packet at very late times and $\delta(k)$ is the phase shift (given by equation (4.11)). We prescribe the spectral function $A(k)$ as in equation (3.24) together

¹The wave packet contains components with negative momenta. They do not participate in scattering.

with the dispersion relation associated with the Klein–Gordon equation. This specifies the initial configurations $\varphi(x, 0)$ and $\dot{\varphi}(x, 0)$, and we utilize the equation of motion (3.8) to find the time–dependent configuration $\varphi(x, t)$. We then consider very late times $t_f \gg 0$ at which the wave packet has completely penetrated the kink and the two structures are again well separated and can be individually identified. This defines the late–time wave packet type solution

$$\eta_{\text{wp}}^{(S)}(x, t_f) = \varphi(x, t_f) - \varphi_{\text{K}}(x - x_0). \quad (5.9)$$

Its (inverse) Fourier transform should be compared with the small–amplitude solution, equation (5.8),

$$\int_{-\infty}^{\infty} \frac{dx}{2\pi} e^{-ikx} \eta_{\text{wp}}^{(S)}(x, t_f) = A(k) \exp[i(\delta(k) - \omega_k t_f)] + \mathcal{O}(a_0^2). \quad (5.10)$$

That is, from the numerical solution to the equation of motion we should be able to extract the phase shift

$$e^{i\delta(k)} = \frac{e^{i\omega_k t_f}}{A(k)} \int_{-\infty}^{\infty} \frac{dx}{2\pi} e^{-ikx} \eta_{\text{wp}}^{(S)}(x, t_f). \quad (5.11)$$

As long as $\eta(x, t)$ satisfies the criteria for a small amplitude fluctuations, the dependence on t_f cancels on the right hand side. A main purpose of the present investigation is to compare the numerical result, equation (5.11), for the components that participate in scattering, with the result from small amplitude approximation in equation (4.11).

5.2 Numerical Results

For simplicity we make an appropriate scaling of the coordinates and the field

$$(x, t) \longrightarrow \frac{(x, t)}{\sqrt{2} M} \quad \text{and} \quad \varphi \longrightarrow \frac{M}{\sqrt{2} \lambda} \varphi \quad (5.12)$$

which allows us to completely absorb the model parameters. Hence their actual values are of minor relevance and all results are general. All numerical results in this section and the next chapter will be quoted in terms of the dimensionless quantities on the right hand side of equation (5.12). In these units, the vacuum solutions are at $\varphi_0 = \pm 1$ and the small amplitude fluctuations have mass $\sqrt{2}$.

The numerical treatment starts by defining an equi–distant grid with spacing $\Delta x = h$ in coordinate space with n_x sites. This establishes an interval on the x –axis that we take to be finite but much larger than the extension of the wave packet and the kink. Again we make sure that grid is sufficiently large to avoid any reflection of the wave packet after the collision with the kink. However, a large grid must be discretized with a greater number of sites to get a good accuracy. The scalar field as a function of time and position is defined by $\varphi_{n,l} = \varphi(x_n, t_l)$, with first time derivative $\dot{\varphi}_{n,l} = \dot{\varphi}(x_n, t_l)$ for $n = 1, 2, \dots, n_x$ and $l = 1, 2, \dots, l_t$, on grids with n_x spatial nodes and l_t temporal nodes. At time $t_1 = 0$, using our algorithm in Appendix B.1, we define the scalar field

as $\varphi_{n,1} = \varphi(x_n, 0)$ and use the initial conditions equations (5.3) and (5.6). We next use a fourth-order center difference scheme to approximate the first and second spatial derivatives [53]:

$$\begin{aligned}\varphi'_{n,1} &\equiv \frac{\partial \varphi_{n,1}}{\partial x} = \frac{1}{12h} (\varphi_{n-2,1} - 8\varphi_{n-1,1} + 8\varphi_{n+1,1} - \varphi_{n+2,1}) + O(h^4), \\ \varphi''_{n,1} &\equiv \frac{\partial^2 \varphi_{n,1}}{\partial x^2} = \frac{1}{12h^2} (-\varphi_{n-2,1} + 16\varphi_{n-1,1} - 30\varphi_{n,1} + 16\varphi_{n+1,1} - \varphi_{n+2,1}) + O(h^4).\end{aligned}$$

This leads to a set of n_x coupled second-order ordinary differential equations (ODE's) for the initial configuration $\varphi_{n,1}$, at $t = 0$ for the initial condition:

$$\ddot{\varphi}_{n,1} = \varphi''_{n,1} + \varphi_{n,1} - \varphi_{n,1}^3. \quad (5.13)$$

Then we employ a fourth order Runge–Kutta algorithm together with an adaptive step size control [53] to solve the equation of motion (5.13). This algorithm propagates the configuration $\varphi_{n,1}$ in time. The adaptive step size slows down the numerical computation considerably as the amplitude, a_0 is increased. At each time step (as well as at the auxiliary intermediate steps required by the Runge–Kutta algorithm) we compute the (second) spatial derivative of the configuration that occurs on the right–hand–side of the equation of motion with an $\mathcal{O}(h^4)$ accuracy. To this end, the configuration is assumed to vanish at points outside the considered interval in coordinate space. This corresponds to the boundary condition that no flux penetrates outside this interval. As a consequence thereof, the wave packet reflects from the spatial boundaries after very long times. This is, of course, not physical but merely a finite size effect, and we have to terminate the simulation at late times when this phenomena becomes visible.

A major criterion to accept the numerical solution is that the total energy, equation (3.9), stays constant in time (at the order of the desired numerical accuracy). As discussed below, the (complex) wave packet initial condition implies that the total energy and the energy density are complex as well. The investigation of the physically relevant energy density, $\varepsilon(x, t)$, in equation (3.9), hence requires to also solve the equation of motion with the initial condition restricted to the real part

$$\eta_R(x) = \int_{-\infty}^{\infty} dk A(k) \cos(kx) \quad \text{and} \quad \dot{\eta}_R(x) = \int_{-\infty}^{\infty} dk \omega_k A(k) \sin(kx) \quad (5.14)$$

of the wave packet. In Figures (5.1) and (5.2) we display the time evolution of the subtracted energy density

$$\bar{\varepsilon}(x, t) = \varepsilon(x, t) - \varepsilon_{\text{bg}}(x) \quad (5.15)$$

for the real initial conditions. To single out the wave packet contribution, we have subtracted the energy density associated with the static background. For the pure wave packet this is zero, but with the kink background we have $\varepsilon_{\text{bg}}(x) = \frac{1}{2} \left[1 - \tanh^2 \left(\frac{x-x_0}{\sqrt{2}} \right) \right]^2$ in the dimensionless units defined in equation (5.12).

We observe an interesting effect at the center of the kink. Once the wave packet has passed by, a residual deformation of the energy density remains. This effect persists even

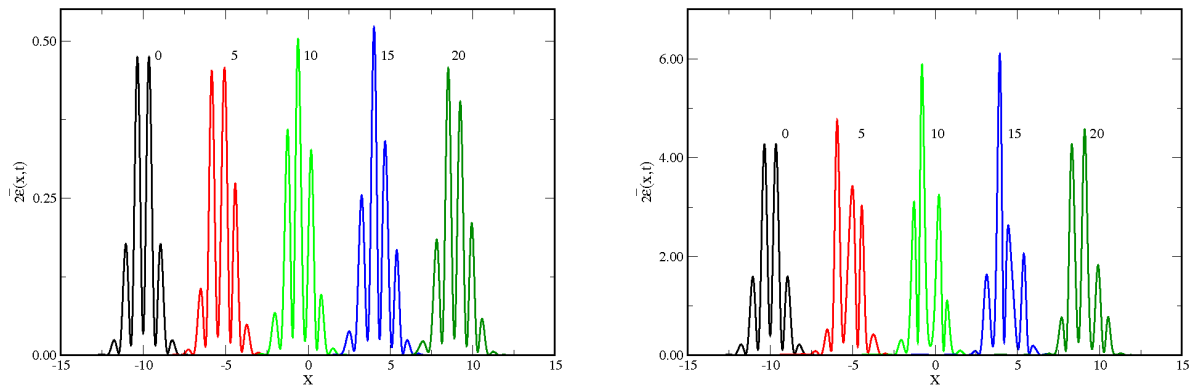


Figure 5.1: Time snapshots of the energy density $\bar{\varepsilon}(x, t)$ (in units $M^4/8\lambda^2$) of the wave packet for real initial conditions. We have used $k_0 = 4$ and $\sigma_k = 2$. Left panel: $a = 0.05$, right panel: $a = 0.15$. The numbers above each wave packet energy density refer to the time variable (we use the same indication for the next figures). Note the different scales on the ordinate.

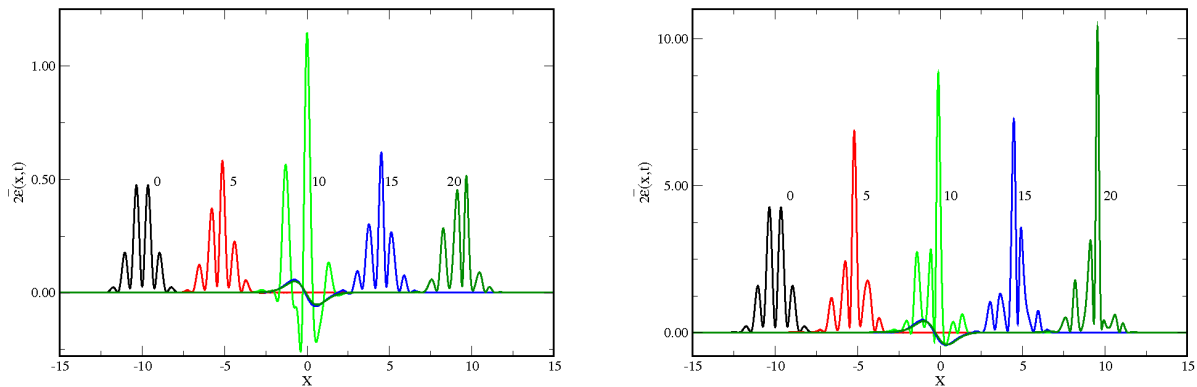


Figure 5.2: Same as Figures 5.1 with the kink background.

for very long times and becomes stable. Also, it is the more pronounced the larger the amplitude of the wave packet is. We will discuss a potential explanation for this effect in subsection 5.2.2.

The energy density associated with the wave packet in particular suggests discussing its spread by first defining the normalized expectation values

$$\langle x^n \rangle = \frac{\int dx x^n \bar{\varepsilon}(x, t)}{\int dx \bar{\varepsilon}(x, t)}, \quad (5.16)$$

where $\bar{\varepsilon}(x, t)$ is the energy density, given by equation (3.3), and n is an integer number. This enables the computation of the squared standard deviation

$$\sigma^2 = \langle x^2 \rangle - \langle x \rangle^2 \quad (5.17)$$

as a direct measure for the width of the wave packet. The time-dependence of the position of the center $\langle x \rangle$ is essentially unaffected by the kink as the data in Table 5.1 show.

	w/o kink		w/ kink	
$t \backslash a_0$	0.05	0.15	0.05	0.15
0	-10.00	-10.00	-10.00	-10.00
5	-5.28	-5.29	-5.28	-5.27
10	-0.56	-0.58	-0.55	-0.55
15	4.15	4.13	4.17	4.17
20	8.87	8.83	8.89	8.90

Table 5.1: The central position $\langle x \rangle$ of the wave packet as a function of time for $k_0 = 4$ and $\sigma_k = 2$.

	w/o kink		w/ kink	
$t \backslash a_0$	0.05	0.15	0.05	0.15
0	0.72	0.72	0.72	0.73
5	0.74	0.79	0.74	0.79
10	0.77	0.95	0.80	0.97
15	0.84	1.16	1.65	1.81
20	0.91	1.38	2.25	2.50

Table 5.2: The standard deviation as a function of time. Parameters are as for Table 5.1.

Furthermore its velocity agrees with what is expected for the wave packet $\frac{k_0}{\sqrt{k_0^2+2}} \approx 0.94$ for $k_0 = 4$. We find the total energy stored in the wave packet to be 0.52 and 4.65 for $a_0 = 0.05$ and $a_0 = 0.15$, respectively. The latter corresponds to more than three times the mass of a Klein-Gordon particle. Nonlinear effects for $\langle x \rangle$, *i.e.* its dependence on a_0 , are only marginal. We compare the results for σ from different values of the amplitude a_0 in both cases, with and without the kink background in Table 5.2. Certainly the kink background causes a significant increase of the spread of the wave packet. Closer inspection shows that this manifests itself mainly after the interaction between the wave packet and the kink, that is for $t > 10$, while even up to the time of interaction no significant difference between the two cases with and without the kink is observed. We associate the strong increase of σ after the interaction with the kink with the emergence of the structure around $x \approx x_0$ rather than a direct spread of the wave packet. Indeed, the comparison between Figures 5.1 and 5.2 does not indicate a severe increase of the spread.

5.2.1 Propagation of pure wave packet

Now we return to the complex valued initial wave packet. We first consider the pure wave packet, equation (5.3). The simulation of equation (5.5) will provide information about the numerical accuracy that we can expect when attempting to extract the phase shift at a later stage.

Figure 5.3 shows the real parts of the numerical solution to the equation of motion for two different values of the amplitude a_0 . The imaginary part in Figure 5.4 behaves similarly, just phase shifted by $\pi/2$. The propagation of the wave packet exhibits spreading similar to that seen in ordinary quantum mechanics, even though the dispersion relation is relativistic. Also we note that the number of (visible) oscillations contained within the wave packet increases with time. From a comparison of the two graphs in Figure 5.3 (or in Figure 5.4) no significant dependence on the initial amplitude of the form of the wave packet can be deduced. This confirms the results for the standard deviation listed in Table 5.2. This absence of significant nonlinear effects is somewhat surprising, since they were expected as a signal of particle production, given that sufficient energy is available.

In Figure 5.5 we show the inverse Fourier transform defined in equation (5.5). As

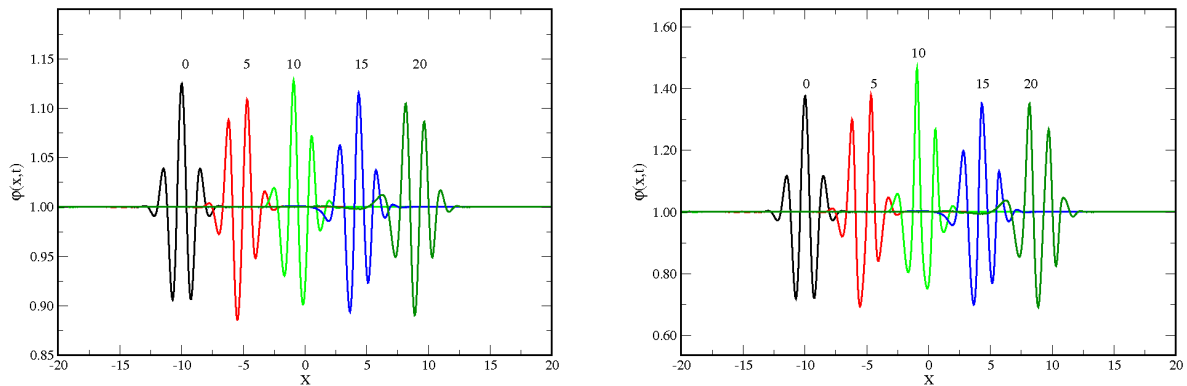


Figure 5.3: Time snapshots of the real part of the configuration $\varphi(x, t) - M/\sqrt{2\lambda}$ for the initial condition, equation (5.6). Furthermore we have used $k_0 = 4$ and $\sigma_k = 2$ to characterize the wave packet. Left panel $a_0 = 0.05$, right panel $a_0 = 0.15$. Note the different scales on the ordinate.

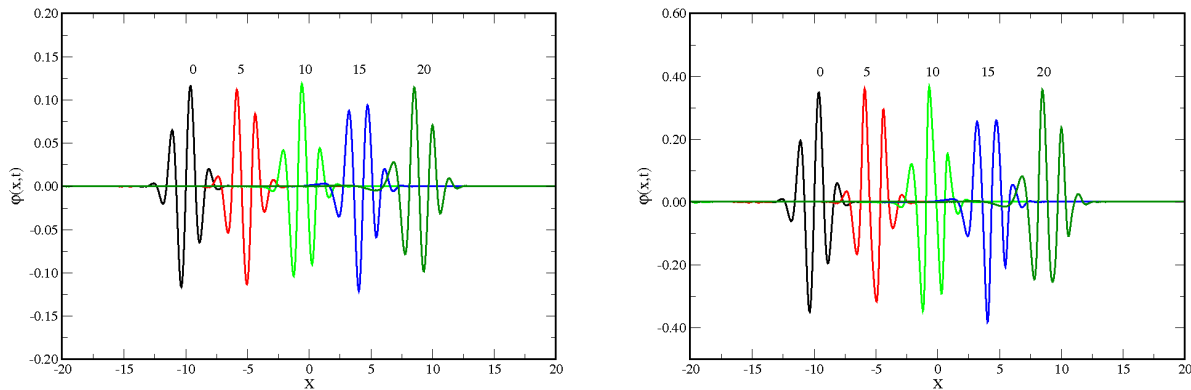


Figure 5.4: Same as Figure 5.3 for the imaginary part.

indicated above, its deviation from unity provides insight into the numerical accuracy that we can achieve, at least for small a_0 . At low momenta, deficiencies (numerical errors) arise because these contributions have left the bulk of the wave packet. Furthermore small errors at low momenta are amplified, since $1/A(k)$ is big in this regime.

The deficiencies at small momenta are certainly independent of a_0 . This is not the case for those at large momenta, even though their structures are very similar. In this momentum regime they originate from the inverse Fourier transform requiring a very fine grid, *i.e.* small h , in coordinate space. Since this comes with a heavy computational cost, it is appropriate to divide the momentum axis into subintervals that are treated with different numerical grid spacings parameters. This change concerns not only the parameters for solving the equation numerically but also the detailed structure of the wave packet characterized by k_0 and σ_k . At the interface of these subintervals, the results extracted from the solutions to the equation of motion (3.8) match. This treatment is also indicated in Figure 5.5. At this stage it is difficult to judge whether these deficiencies at large k are of numerical origin or signals of the nonlinear dynamics.

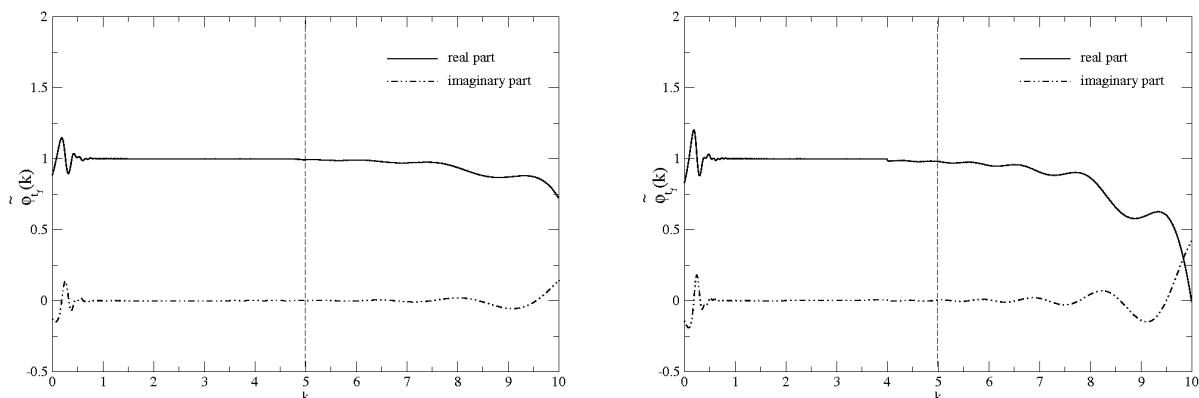


Figure 5.5: The inverse Fourier transform of equation (5.5) for $a_0 = 0.05$ (left) and $a_0 = 0.20$ (right). The dashed vertical lines separate regimes with different numerical parameters to improve the numerical accuracy.

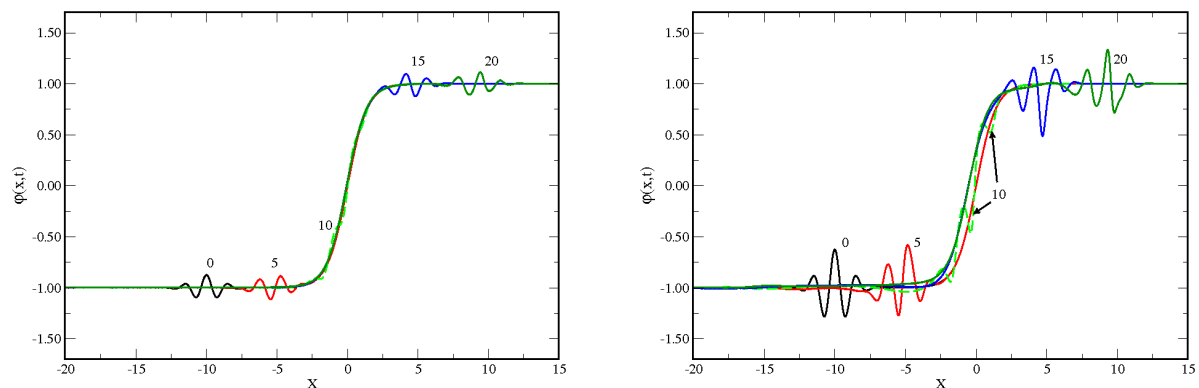


Figure 5.6: Time snapshots of the real part of the configuration $\varphi(x, t)$ for the initial condition, equation (5.7). Left panel $a_0 = 0.05$, right panel $a_0 = 0.15$.

5.2.2 Propagation in kink background

Figure 5.6 displays the solutions of the numerical integration of the equation of motion at different times for small and moderate initial amplitudes of the wave packet. At all times, the deviation from the kink is localized spatially. We clearly identify the interaction process when the wave packet *climbs* up the kink. A wave packet with a small amplitude essentially retains its shape after the interaction, the only effect being characterized by the phase shift, which we will extract later. Surprisingly, even for moderate amplitudes the shape of the wave packet does not change significantly with time.

Figure 5.6 has the potential to explain why the energy density $\bar{\varepsilon}$ developed some structure around $x = x_0$ after the interaction with the kink. The interaction with the wave packet yields a displacement d of the kink. This displacement increases with the initial amplitude a_0 . We quantify this increase by identifying the point d at which $\varphi(d, t) = 0$ in the vicinity of x_0 for very late times. We list d for various values of $a_0 \leq 0.2$ in Table 5.3. In support of the small amplitude approximation, the displacement vanishes with

	t=100				t=150				t=200			
a_0	0.05	0.10	0.15	0.20	0.05	0.10	0.15	0.20	0.05	0.10	0.15	0.20
d	-0.07	-0.40	-0.80	1.32	-0.07	-0.39	-1.13	2.80	-0.07	-0.40	-1.09	3.05

Table 5.3: Displacement, d measured relative to x_0 , of the kink as a function of the initial amplitude of the wave packet, a_0 .

		w/o kink				w/ kink			
		$\langle x \rangle$		σ		$\langle x \rangle$		σ	
$t \setminus a_0$		0.05	0.15	0.05	0.15	0.05	0.15	0.05	0.15
50		37.2	37.1	1.54	2.92	37.5	37.2	1.40	2.28
100		84.4	84.2	2.71	5.28	84.8	85.3	1.84	4.90
150		131.5	131.3	3.89	7.61	132.1	132.8	2.22	7.93
200		178.7	178.4	5.09	9.92	179.3	180.2	4.94	11.40

Table 5.4: Center and spread of the wave packet in the kink background for very late times. We compare the two cases with the vacuum and the kink backgrounds. In both cases, we have used $k_0 = 4$ and $\sigma_k = 2$ with real initial conditions.

the amplitude. For moderate a_0 , it saturates after a while and stays constant, at least at the order of our numerical accuracy.² As a_0 increases further, the displacement changes sign and slowly grows with time. This is the onset of a novel nonlinear effect, which we will discuss further in subsection 5.2.4. Our numerical simulations suggest that d does not depend on k_0 . For negative d , the numerically observed structure of $\bar{\varepsilon}(x, t)$ in the vicinity of x_0 is reasonably reproduced by $\varepsilon_{\text{bg}}(x - d) - \varepsilon_{\text{bg}}(x)$, *i.e.* the corresponding shift of the background energy density. The larger the time interval, the better the agreement with this analytic expression. To separate the displacement effect and to focus on the time evolution of the wave packet, we repeat the calculation of equations (5.16) and (5.17) with the lower boundary of the integral taken between the kink and wave packet, so we can separate these structures unambiguously. The results are shown in Table 5.4. The comparison with the time evolution of the wave packet in the trivial background reveals that the interaction with the kink has only a minor influence on the spread of the wave packet once the displacement of the kink is properly accounted for. In both cases, the spread increases with the amplitude of the wave packet. This summarizes the main features of the wave packet for small and moderate amplitudes. For $a_0 > 0.2$, we observe a different behavior, which we will discuss later.

5.2.3 Extraction of the phase shift

We now turn to a major subject of this investigation in this chapter, the extraction of the phase shift from the scattering process. The comparison with the result in the small amplitude approximation, equation (4.11), serves as a crucial test for the quality of the

²On the overall scale this maximum displacement is an effect at the order of a fraction of a percent.

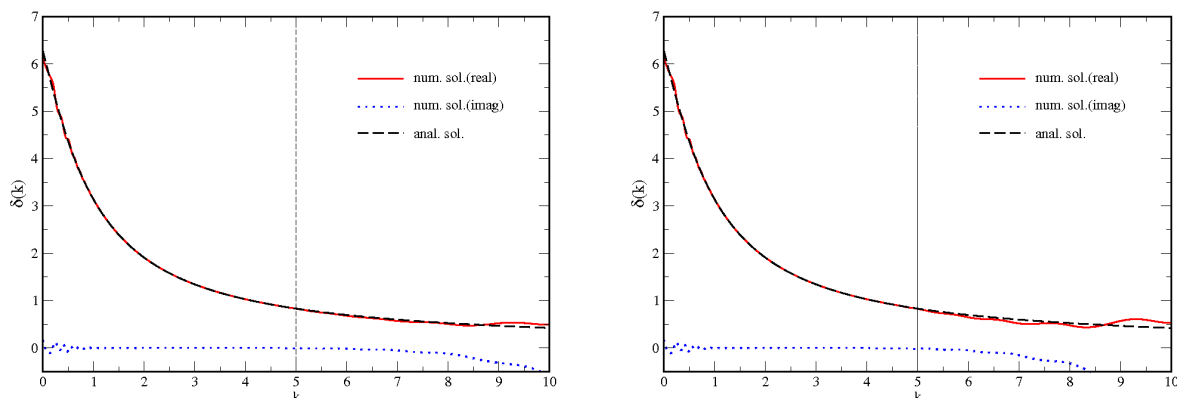


Figure 5.7: Extraction of the phase shift for various momentum regimes. The wave packet is characterized by $k_0 = 4$, $\sigma = 2$. Left panel: $a_0 = 0.05$, right panel: $a_0 = 0.15$. Different numerical parameters serve to improve the agreement with the analytical result in two distinct regimes. Left regime: optimized for small and moderate momenta, right regime: optimized for large momenta.

numerical solution to the time-dependent equation of motion. Numerically solving the equation of motion (3.8) to determine the full momentum dependence of the phase shift faces various obstacles. First we have to incorporate the above mentioned displacement of the integral in equation (5.11). This is straightforwardly accomplished by restricting the integration interval to the regime of the wave packet. For very late times ($t_f > 100$), this regime is clearly separated from the kink. Other obstacles are more cumbersome. Wave packet components with small momenta take long time to finish this interaction with the kink. Hence we need to solve the equation of motion for a large interval on the time axis. In the dimensionless units defined above we consider $t \in [0, 200]$. We also vary the upper limit to verify stability of the results. However, components with large momenta will propagate a long distance in the same time interval. Hence we also need to consider a large interval in coordinate space. In order to reliably find the Fourier transform, equation (5.10), we require a dense grid in coordinate space for large momentum components. To keep the numerical effort within a manageable range, it is therefore appropriate to split the computation in (at least) two parts. To extract the phase shift for small momenta, we consider a large time interval but a small interval in coordinate space. This leads to unreliable results at large momenta. For this regime, we consider a small time interval, but a large one in coordinate space, together with a dense grid. At intermediate momenta, the two procedures yield identical results. Furthermore, we have the freedom to tune the parameters of the wave packet, k_0 and σ_k to suit the considered regime in momentum space. These issues are indicated in Figure 5.7. In that figure we have matched two numerical treatments at $k = 5$. We also display the numerical result for the imaginary part of the right hand side of equation (5.11). Its deviation from unity serves as a further test on the numerical accuracy. As expected, the deviation is small except for very small and very large momenta. Otherwise the agreement with the analytical result, equation (4.11), is excellent. Certainly, further subdivision of the momentum axis and optimization in each segment will yield even better agreement. We have obtained the result displayed in Figure 5.7 for a small amplitude ($a_0 = 0.05$), for which the small

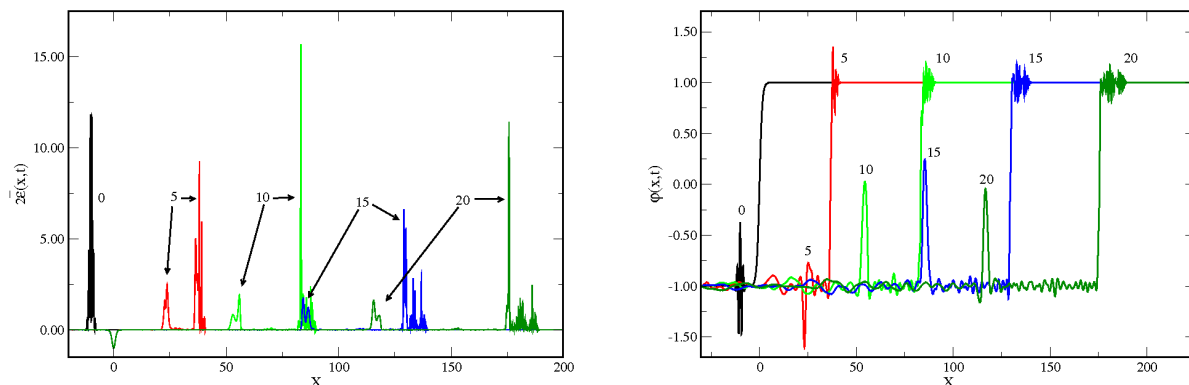


Figure 5.8: Results for real initial conditions using $a_0 = 0.25$. Left panel: subtracted energy density $\bar{\varepsilon}(x, t)$, right panel: field configuration $\varphi(x, t)$.

amplitude approximation is expected to be accurate. Figure 5.7 shows that we find identical phase shifts for different amplitudes, a_0 .

5.2.4 Nonlinear effects in the kink background

As indicated in previous sections, the extraction of the phase shift relies on the small-amplitude assumption. If $\mathcal{O}(\eta_{\text{wp}}^2)$ effects are not negligible, we cannot expect the right-hand-side of equation (5.11) to have unit magnitude. Rather, we expect it to be less than one, corresponding to particle production. But we did not observe this effect even for moderate amplitudes. Instead we have identified a small displacement of the kink as the single major effect of the nonlinear dynamics. It corresponds to an attraction shortly before and a repulsion shortly after the interaction with the wave packet. This displacement also complicates the extraction of that part of the energy density, $\bar{\varepsilon}(x)$, that is associated with the wave packet. Once this is properly done, $\bar{\varepsilon}(x)$ serves as a probability distribution of the wave packet. The propagation of its center does not exhibit consequences of the nonlinear dynamics. This propagation is not significantly altered by the presence of the kink. However, the spread of the wave function shows some increase with the amplitude of the wave packet.

We show the typical behavior of the energy density, $\bar{\varepsilon}(x, t)$ at larger amplitudes in Figure 5.8. Surprisingly, there is no footprint from the kink at x_0 . Instead we observe that the wave packet splits into two pieces and there is a dominant peak in $\bar{\varepsilon}(x, t)$ at the back of the more quickly propagating piece. The field configuration itself reveals the answer to this peculiarity. First we observe that the wave packet splits in (at least) two pieces of different velocities. This is an indication of particle production. Actually we also observe such splitting for the trivial background. However, it sets in at somewhat larger amplitude.³ More notably, in the kink background the transition from one vacuum configuration ($\varphi_0 = -1$) to the other ($\varphi_0 = 1$), which is required to occur somewhere by conservation of the topological charge, now emerges at the back of the dominant piece of the wave packet rather than at the position of the kink before the interaction. The

³For the trivial background we did not observe it for $a_0 = 0.25$ but for $a_0 = 0.35$.

dominant peak in $\bar{\varepsilon}(x, t)$ results from the kink being dragged by the wave packet. As a pronounced nonlinear effect we find a transition from a stationary kink to a co-moving kink as the amplitude exceeds a certain value a_c . We extract this value from the behavior of the energy density. When a structure persists at a value of $d \leq x_0$ that marginally changes in time, the kink is considered to be stationary. Disappearance of this structure provides the critical value. For $k_0 = 4$ and $\sigma_k = 2$ we find $a_c = 0.201$. Obviously, it is impossible to extract scattering data from these structures. This is even more the case as parts of the initial wave packet now trail after the kink.

Chapter 6

Kink–antikink collisions

The kink–antikink collisions in the non-integrable φ^4 field model have been studied by numerous groups [30, 32, 35, 38, 39, 54, 55, 56, 57]. This work has shown that the kink–antikink system can behave both as a bound (trapped or bion) state solution or as a solution having distinct oppositely directed kink–antikink plus small fluctuations. The appearance of these solutions after the collision, for the initial field configuration in Figure 6.1a, depends on the impact velocity of the kink–antikink system. For some velocities the final state has a kink and an antikink that reflected from each other plus emitted fluctuations. This case is depicted in Figure 6.1b. For other velocity ranges, the final state has trapped solutions. These are similar to the breather solutions of the sine-Gordon system except that in the trapped case there is local dissipation of energy every time the kink and the antikink collide with each other. Such a scenario is depicted in Figure 6.1c. In contrast, the kink–antikink collision solutions, in the integrable sine-Gordon field model have two-soliton and breather solutions, cf. section 3.3. Colliding soliton–antisoliton pairs in the sine-Gordon system finally pass through each other by a phase shift or time delay, equation (3.51).

We use the algorithm from the previous chapter (see also Appendix B.1) to present numerical solutions of kink–antikink collisions. Our numerical solutions are consistent with earlier studies. In the following sections, we show the well-known two-bounce windows [32, 56] and n -bounce windows (where n is an integer greater than 2) [55] in the velocity range below a critical velocity $v_{in} \lesssim 0.26$ (to be defined later). In this case the collision results in bound state formation and erratic reflection plus small fluctuations. Beyond the critical velocity, $v_{in} > 0.26$, we see that the kink and antikink bounce once and reflect inelastically to infinity with accompanying small fluctuations. At very late times we subtract the analytic solution for the kink–antikink system from our numerical field configuration solution to get the emitted radiation of the kink–antikink collision (see Figure 6.1d). This radiation is composed of modes bound by the kink–antikink and modes scattering off the kink–antikink, cf. section 4.3. In particular, this radiation gives us information about the kink–antikink annihilation process, as we discuss below. Later on, we discuss the collective coordinate approximation of the kink–antikink system. We compare the results from the collective coordinate system with our numerical simulation. Finally, in the last section we extract the scattering amplitude in two different output

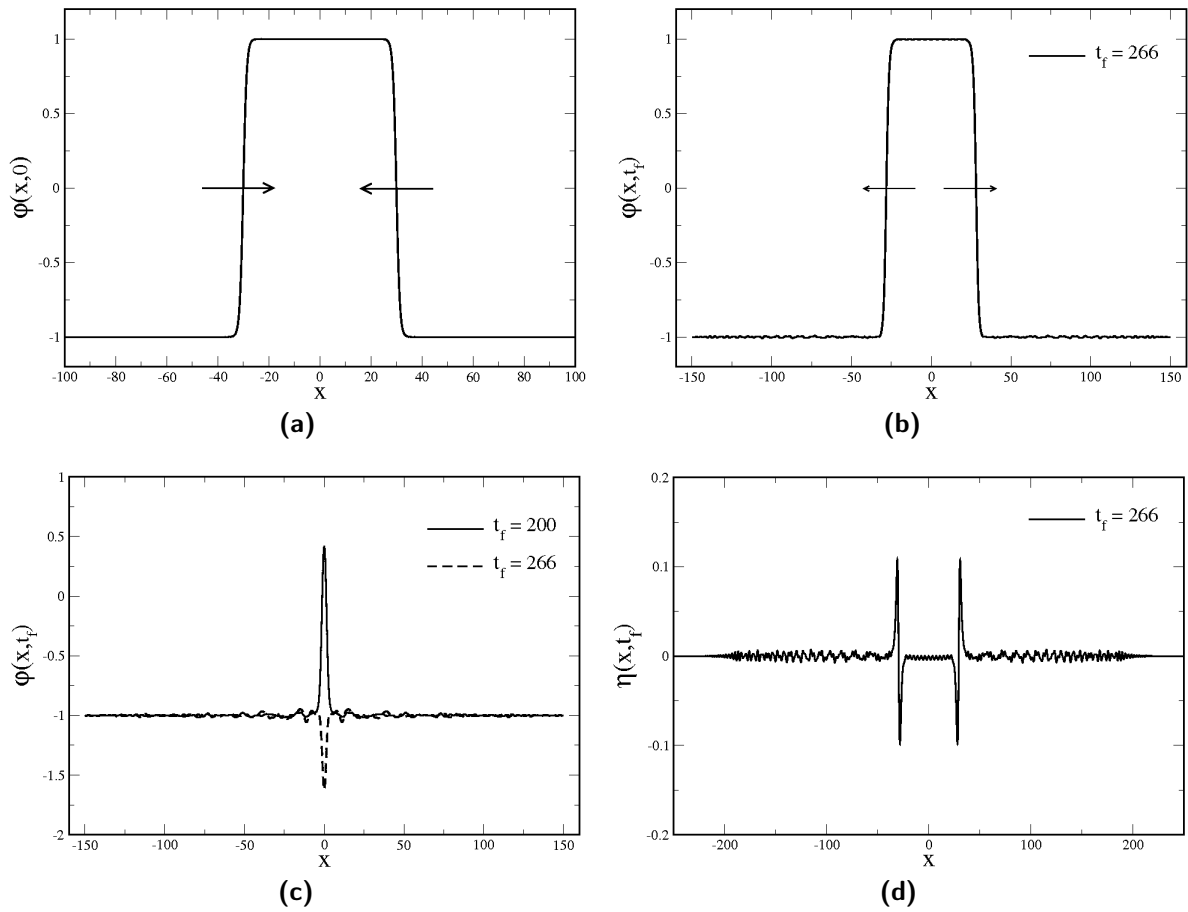


Figure 6.1: (a) The initial field configuration $\varphi(x, 0)$ of the kink–antikink pairs system, equation (6.1), at $x_0 = 30$. (b) Reflected kink–antikink in the final state of the system plus small fluctuations. (c) The bion state in the final state of the system plus small fluctuations. (d) The deformation of the system at very late times (the internal modes plus the scattering modes) beyond the critical velocity. (b), (c) and (d) are asymptotic states at later time $t_f = 266$. Note the different scale on the ordinates.

channels of the kink–antikink collision. First, in the inelastic scattering process for the kink–antikink ($\varphi_K + \varphi_{\bar{K}} \rightarrow \varphi_K + \varphi_{\bar{K}} + \eta_k$ (emitted perturbative radiation)). This takes place beyond the critical velocity and for some initial velocity ranges below the critical velocity, where the final state consists of a kink and an antikink. We calculate the time delay between the incoming and outgoing kinks (or antikinks). The phase shift will be extracted from that time delay. We determine the scattering amplitude by combining the phase shift with the ratio of the outgoing and incoming fluxes. Second, in the annihilation process of the kink–antikink ($\varphi_K + \varphi_{\bar{K}} \rightarrow \eta_k$ (radiation)). For some initial velocity ranges below the critical velocity, we determine the amplitude of the emitted radiation. This radiation consists of plane waves, since neither kinks nor antikinks are formed in the final state of the collision. We focus in particular on crossing symmetry. Beyond the critical velocity, we always have a kink and an antikink in the final state ($\varphi_K + \varphi_{\bar{K}} \rightarrow \varphi_K + \varphi_{\bar{K}} + \eta_k$ (emitted perturbative radiation)). We use a Lorentz transformation to determine the emitted radiation in the rest frame of the antikink. We do

this as subtraction of the analytic kink (or antikink) solution from the transformed final field configuration. Then the amplitude of the emitted radiation can be determined by equation (4.24).

6.1 Numerical results

We consider kink φ_K and antikink $\varphi_{\bar{K}}$ solutions

$$\varphi_{K(\bar{K})}(Z) = \pm \tanh\left(\frac{Z}{\sqrt{2}}\right)$$

and recall our scaling of the coordinates (x, t) and the field φ , equation (5.12), from the previous chapter. Since we seek to solve the time-dependent equation of motion (3.8) for the kink–antikink pair system, we first determine the initial condition, which is

$$\varphi(x, 0) = \varphi_K\left(\frac{x + x_0}{\sqrt{1 - v^2}}\right) + \varphi_{\bar{K}}\left(\frac{x - x_0}{\sqrt{1 - v^2}}\right) - 1. \quad (6.1)$$

Here $\mp x_0$ are the centers of the kink and antikink, respectively. The field configuration $\varphi(x, 0)$ takes the values $\varphi(\pm\infty, 0) = -1$ at the boundaries and $\varphi(0, 0) = 1$ at the center of mass. The time derivative of the field $\varphi(x, 0)$ initially is

$$\dot{\varphi}(x, 0) = \frac{v}{\sqrt{2(1 - v^2)}} \left[2 - \varphi_K^2\left(\frac{x + x_0}{\sqrt{1 - v^2}}\right) - \varphi_{\bar{K}}^2\left(\frac{x - x_0}{\sqrt{1 - v^2}}\right) \right]. \quad (6.2)$$

These equations (6.1) and (6.2) represent widely separated kink and antikink configurations moving toward each other with velocity v at $t = 0$. This field is depicted in Figure 6.1a. We take $2x_0$, the spatial separation of the kink centers, to be large enough to avoid the overlap between the kink and the antikink. We utilize our numerical algorithm from the previous chapter with the initial conditions (6.1) and (6.2) to solve the partial differential equation (3.8) for the kink–antikink pairs system. The accuracy of our numerical solutions is tested by numerically computing the conserved total energy, equation (3.9), for all cases. We observe that the collision results depend on the impact velocity. We summarize our numerical solutions in Figure 6.2a for the initial velocity range $0.0001 \leq v_{in} \leq 0.95$. The critical velocity, $v_c \approx 0.26$, distinguishes between simple and complicated collision results that are observed. In the simple collision the kink and the antikink collide once and reflect inelastically to infinity with emitted radiation. This only happens beyond the critical velocity *i.e.* $v_{in} > v_c$. In the complicated collision regime (*i.e.* $v_{in} < v_c$) the kink and the antikink form a bound state and reflect erratically.

We obtain the final velocity v_{out} of the antikink in Figure 6.2a by calculating the average velocity of the kink–antikink pair

$$\bar{v} = \frac{\langle x \rangle(t + \Delta t) - \langle x \rangle(t)}{\Delta t}, \quad (6.3)$$

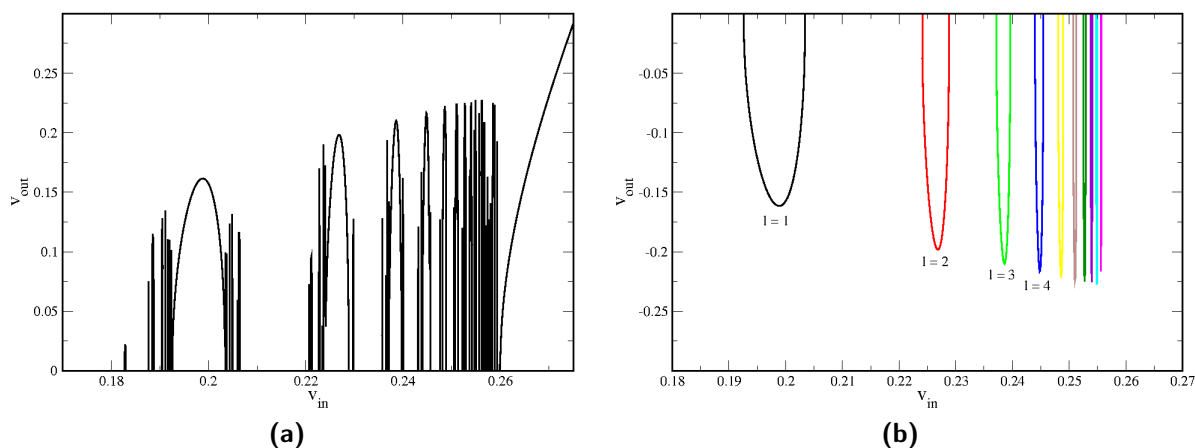


Figure 6.2: (a) Final velocity v_{out} of the antikink, in the kink–antikink system, as a function of the initial velocity v_{in} for the n -bounce windows. (b) Final velocity v_{out} of the kink, in the kink–antikink system, as a function of the initial velocity v_{in} for the two-bounce windows only, with time delay $l = 1, 2, 3, \dots$, and 10, equation (6.5).

where $\langle x \rangle$ is the trajectory of the antikink as a function of time t , given by¹

$$\langle x \rangle(t) = \frac{\int_0^\infty dx x \varepsilon^j(x, t)}{\int_0^\infty dx \varepsilon^j(x, t)}. \quad (6.4)$$

Here $\varepsilon(x, t)$ is the energy density, given by equation (3.9), and j is a positive integer. Thus the final velocity v_{out} of the antikink is the average velocity \bar{v} at very late times, after the collision has occurred. For every impact velocity in $0.0001 \leq v_{in} \leq 0.95$ we calculate \bar{v} to obtain the final velocity v_{out} of the antikink as a function of the impact velocity v_{in} . The result is shown in Figure 6.2a. Note that $v_{out} = 0$ implies that no kink in the asymptotic state; instead, a trapped oscillatory state is formed. We have seen that at low initial velocities, $v_{in} \leq 0.1828$, a trapped state is always formed, and at higher initial velocities, $0.261 \leq v_{in}$, the kink and the antikink always reflect inelastically from each other. The striking feature of Figure 6.2a is the sequence of regions of intermediate v_{in} , in which trapping and erratic reflection arise from the asymptotic state. In the same way, by integrating equation (6.4) from $-\infty$ to 0 and varying v_{in} from 0.0001 to 0.95, we have calculated the final velocity of the kink in Figure 6.2b. We omit the $n \neq 2$ bounce windows to display the figure and initial velocity intervals that were already found by Campbell et al.[32] for the two-bounce windows.

Below the critical velocity

For some ranges of the initial velocity less than the critical velocity, $0.0001 \leq v_{in} \leq v_c$, the kink and antikink collide, reflect, recede to finite separation, return to collide again, reflect, recede to finite separation, return to collide and so on. In this type of collision, after the first collision, the kink and the antikink do not have enough energy to escape to

¹The trajectory of the kink is the same but with negative $\langle x \rangle$.

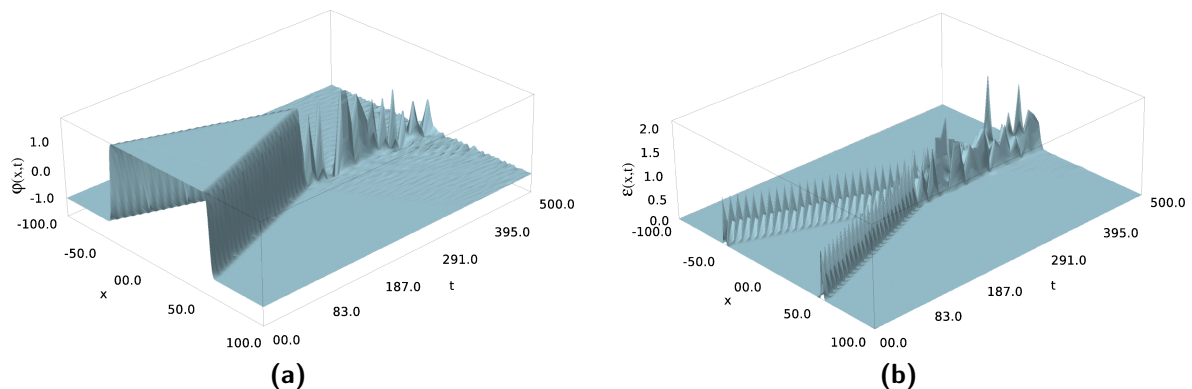


Figure 6.3: (a) The numerical field configuration solution $\varphi(x, t)$ of the kink–antikink pairs system as a function of space and time in the bion state formation plus emitted fluctuations and (b) Its energy density as a function of space and time.

infinity. Instead, they stick together, form a bound (bion) state and emit radiation every time they collide. In this case, the final state does not have any kink solutions. This behavior appears in some intervals below the critical velocity in Figure 6.2a, where the final velocity of the antikink (kink) is zero. These solutions have the potential to allow a statement about crossing symmetry for soliton interaction in the φ^4 model. Figure 6.4a displays the formation of this bound state by showing the field at the center of mass $\varphi(0, t)$ for initial velocity $v_{in} = 0.19$. Earlier studies [56] showed that the bound state oscillations in Figure 6.4a are chaotic. We exhibit in Figures 6.3a and 6.3b the evolution of the numerical solution of the field configuration $\varphi(x, t)$ for the kink–antikink system in the bound state and its energy density. This oscillating state has extremely long life time and frequency ≈ 1.07 . Approximately 0.5% of its energy dissipates per period. This result is in good agreement with the earlier study in [58, 59]. To this end, the bion state is similar to the breather state in the sine-Gordon system, equation (3.52), except that it has dispersion of energy carried by the emitted fluctuations, as shown in Figure 6.1c.

In the other ranges of the initial velocity less than the critical velocity, $0.0001 \leq v_{in} \leq v_c$, reflection can occur: The kink and antikink collide, reflect, recede to finite separation, return to collide again and then reflect to infinity. This state is called the two-bounce window, referring to the number of reflections. In this window we use equation (6.4) to trace the trajectory of the antikink, which is depicted in Figure 6.4b. Figures 6.5a and 6.5b display the numerical solution of the field configuration $\varphi(x, t)$ in the two-bounce window and its energy density at different times. This process has been qualitatively explained by Campbell et al.[32] in terms of an exchange of energy between the kink translational energy and a localized mode (“shape mode”). The basic idea is that when the kink–antikink first collide, there is an energy transfer into the shape mode. The kink–antikink then move apart, but do not have enough energy to overcome the attractive potential which exists between them, since some energy was given to the shape mode and they fall back toward one another. When they collide again, the energy in the shape mode can be transferred back to the translational motion if the time T between the collisions obeys the following resonance condition

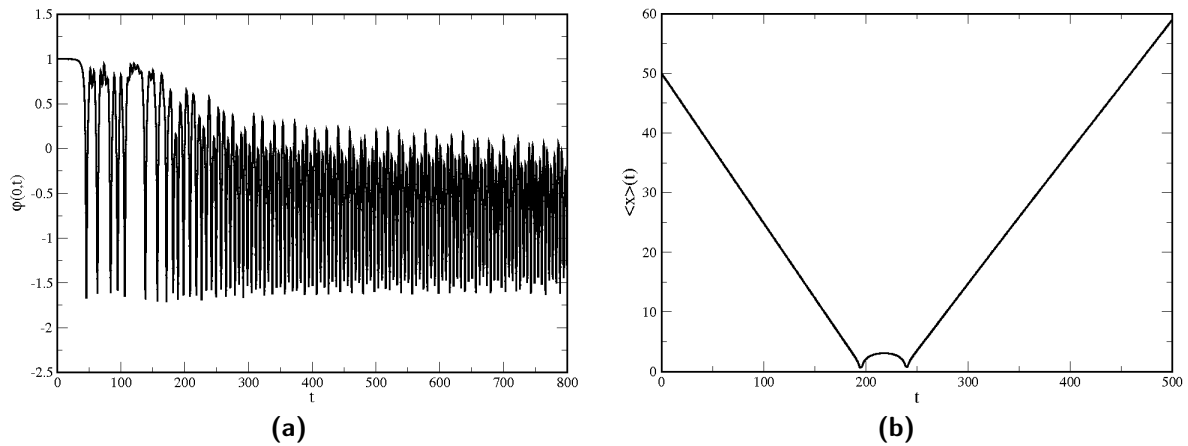


Figure 6.4: (a) Formation of a bound state is represented by an oscillating center of mass $\varphi(0, t)$ of the kink-antikink system at initial velocity $v_{in} = 0.19$. (b) Trajectory of the antikink solution in the kink-antikink system at initial velocity $v_{in} = 0.251$.

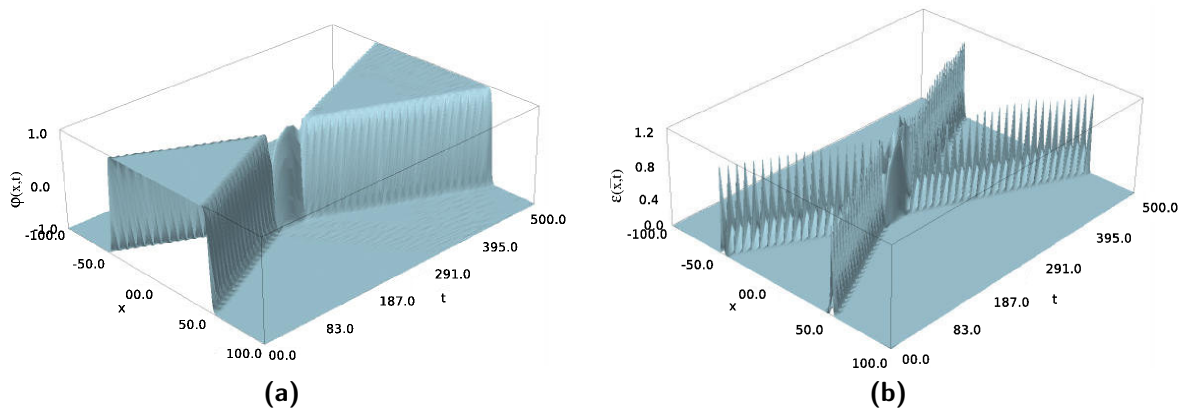


Figure 6.5: (a) The numerical field configuration solution $\varphi(x, t)$ of the system as a function of space and time in the two-bounce window at $v_{in} = 0.251$ and (b) Its energy density as a function of space and time.

$$\omega_1 T = \theta + 2\pi l, \quad (6.5)$$

where $\omega_1 = \sqrt{3/2}$ is the frequency of the shape mode, θ is some offset phase and l is an integer (the window's number). Figures 6.6a and 6.6b show that the time between the two-bounce collision in window $l = 5$ is much longer than the time in window $l = 1$. It was reported in ref.[56] that equation (6.5) is valid for the three-bounce windows as well, which can be observed from Figures 6.6c and 6.6d.

Such a transfer of energy allows the kink and antikink to overcome this attractive potential and escape to infinity. This idea was used by Campbell et al.[32] to predict the velocity intervals for the two-bounce windows and find the behavior of the final velocity as a function of the initial velocity. These estimates are in good agreement with the results obtained from our numerical simulation in Figure 6.2b. Also, we have calculated the final

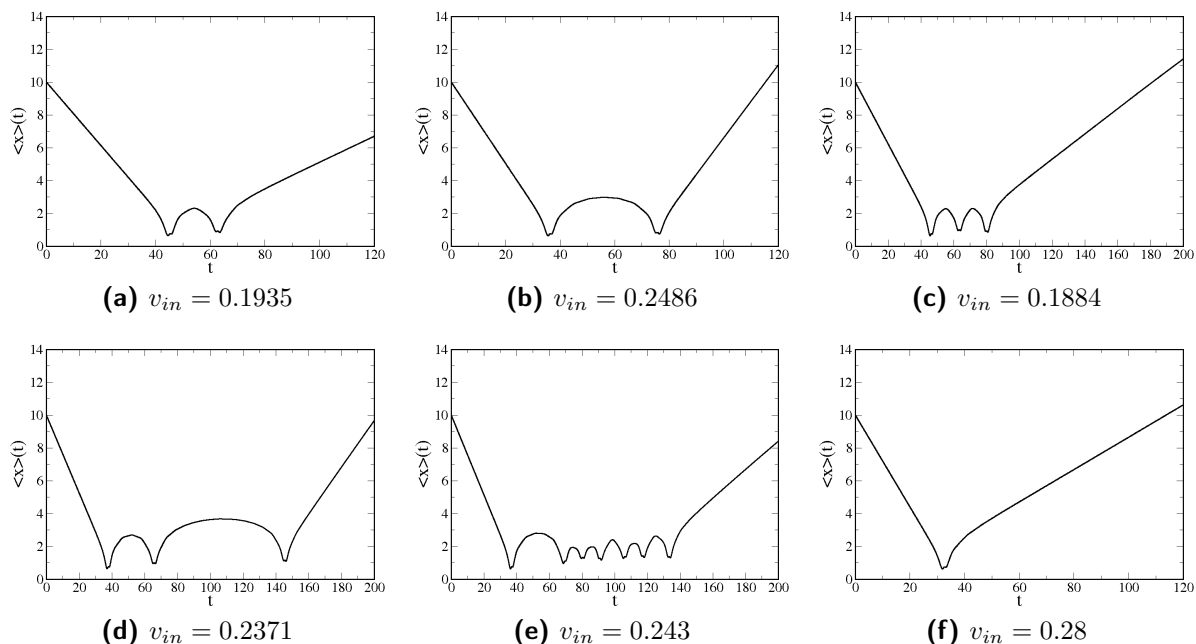


Figure 6.6: (a) and (b) display the antikink trajectory in two different two-bounce windows ($n = 1$ and $n = 5$ respectively). (c) and (d) display the antikink trajectory in two different three-bounce windows. Note that the time between the collision gets longer as the window's number l increases. (e) and (f) display the highest- and lowest-bounce window found in our numerical simulation, respectively.

velocity for n -bounce windows, which is depicted by the striking feature in Figure 6.2a. In our numerical simulation we have observed over 20 two-bounce windows and windows with bounce number up to seven, as shown in Figure 6.6e. But as long as we allow the window width Δv to be small enough, for $0.0001 \leq v_{in} \leq v_c$, we can observe windows with more bounces. Up to 30 two-bounce windows were reported in [56].

Beyond the critical velocity

Now, we come to the single collision results that occur when the initial velocity is larger than the critical velocity v_c . The kink and antikink collide once and inelastically reflect to infinity, emitting small fluctuations. For these cases, the trajectories of the antikinks behave like the trajectory of the antikink in Figure 6.6f with one bounce collision. Note that after the collision takes place, the velocity of the system is not equal to the initial one. The kink–antikink, after the collision, transfer some energy to other modes of the system, such as the shape mode and the small fluctuations (radiation or phonons). These modes are shown in Figure 6.1d. Figures 6.7a and 6.7b display the numerically obtained field configuration $\varphi(x, t)$ of the kink–antikink pair and its energy density $\varepsilon(x, t)$, respectively, at $v_{in} = 0.28$, which is above the critical velocity v_c .

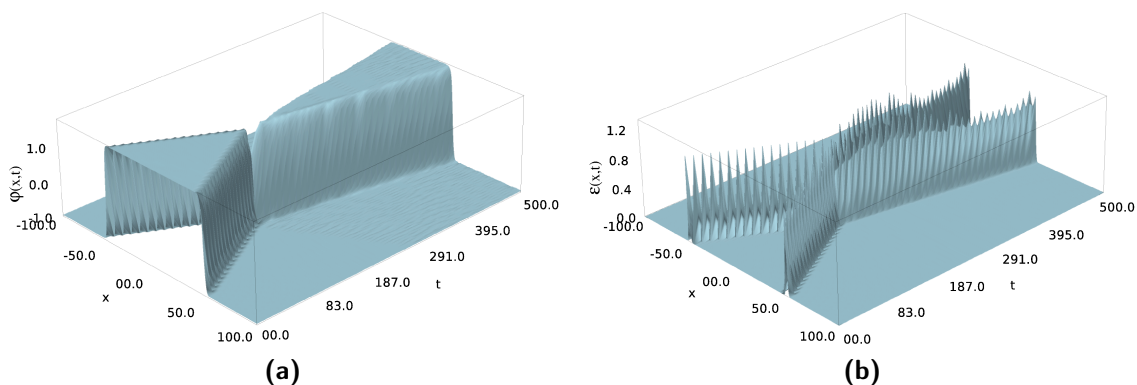


Figure 6.7: (a) The numerical field configuration solution of the kink–antikink as function of the space and the time in the one-bounce window at velocity $v_{in} = 0.28$ and (b) its energy density.

6.2 Novel features

In the context of our numerical simulation and from Figure 6.6f we see that when the kink–antikink come close to each other and begin to interact with one another, their velocity increases, suggesting that they experience an attractive force. At shorter distances they suddenly decelerate and exhibit a repulsive force, almost like a hard core collision, until they stop. The same scenario starts again when they reflect from each other and they accelerate. After passing some distance, they decelerate again. After leaving the interaction region between them, they move with mainly constant velocity. This behavior is depicted in Figures 6.8a and 6.8b, which display the phase diagrams of the antikink solution in one bounce and two-bounce windows, respectively. For n -bounce windows, $n > 2$, the figures contain n loops before the kink–antikink depart to infinity.

Earlier studies of this sector provided an approximate analytic description of the dynamics of the kink–antikink pair as well as the attractive force between the kink and the antikink. Kudryavtsev [59] was the first to implement collective coordinates showing that the effective potential between the kink and antikink was attractive. A bit later, Sugiyama [60] introduced collective coordinates to reduce the number of degrees of freedom of the kink–antikink pairs system. The collective coordinates are the center of mass of the kink–antikink and the amplitude $A(t)$ of the shape mode ξ_1 , equation (4.6). His analysis was mainly analytic, producing an attractive potential in which the kink–antikink moved and a solution for the shape mode coordinate that exhibited harmonic oscillations.

We reanalyze the ansätze of the reduced system from earlier studies to study kink–antikink collisions using two degrees of freedom. In this study we seek to find the shape of the potential between the kink and the antikink, describe the relative velocity of the kink–antikink as a function of the collective coordinates and perform a thorough comparison with the solution of the full system. We modify the parameterization of the ansätze that were introduced in [32, 60] to account for relativistic effects,

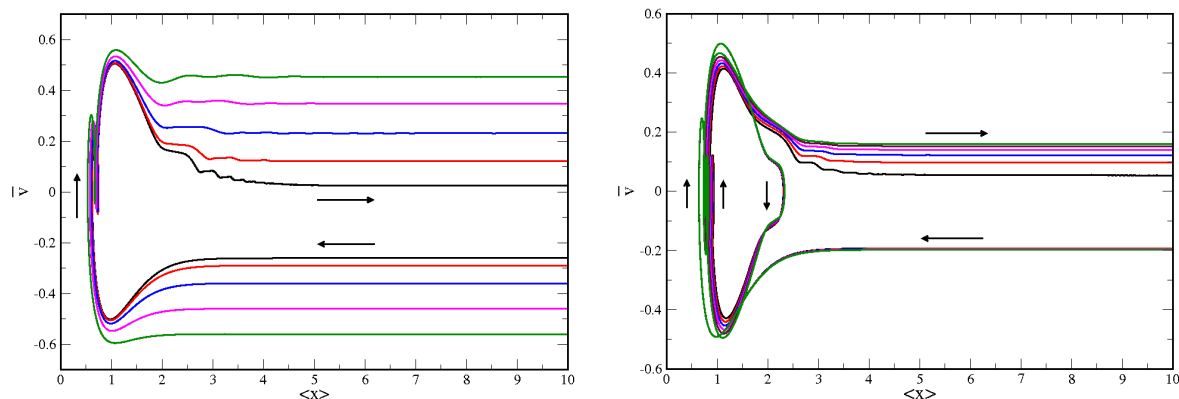


Figure 6.8: (a) and (b) display the average velocity \bar{v} of the kink–antikink pairs system as a function of the mean value of the position $\langle x \rangle$ for one- and two-bounce window, respectively. Each line represents the calculation of v_{out} for specific initial velocity v_{in} and the arrows indicate the direction of the motion. Note that in figure (b) the difference between the chosen initial velocities is very small but they are not equal.

$$\begin{aligned} \varphi_{\text{ansatz}}(x, t) = & \varphi_K \left(\frac{x + X(t)}{\sqrt{1 - v^2}} \right) + \varphi_{\bar{K}} \left(\frac{x - X(t)}{\sqrt{1 - v^2}} \right) - 1 \\ & + A(t) \left[\xi_1 \left(\frac{x + X(t)}{\sqrt{1 - v^2}} \right) - \xi_1 \left(\frac{x - X(t)}{\sqrt{1 - v^2}} \right) \right]. \end{aligned} \quad (6.6)$$

Here $v = v_{in} \equiv \dot{X}(0)$ and \dot{X} is the first derivative of X with respect to time t . Equation (6.6) describes the kink–antikink system using two degrees of freedom. It consists of a kink and an antikink at a time-dependent separation given by $X(t)$, each accompanied by an internal shape mode ξ_1 with time-dependent amplitude $A(t)$. The variable $X(t)$ is introduced as the collective coordinate representing half the distance between the kink and antikink. We substitute the ansätze, equation (6.6), into the Lagrangian density equation (3.7) and integrate over all the space, x from $-\infty$ to ∞ . This yields the effective Lagrangian for the collective coordinates

$$L_{\text{eff}}(X, \dot{X}, A, \dot{A}) = [M_v + I_v(X)]\dot{X}^2 - U_v(X) + \dot{A}^2/\gamma - w^2 A^2 + 2 F_v(X) A, \quad (6.7)$$

where the functions $I_v(X)$, $U_v(X)$ and $F_v(x)$ are given by

$$\begin{aligned} I_v(X) &= 3M_v (1 - \tanh^2(\alpha)) (\alpha - \tanh(\alpha)) / \tanh^3(\alpha), \\ U_v(X) &= 6M_v \left[-\frac{2}{3} + \alpha + 3 \coth(\alpha) - [2 + 3\alpha] \coth^2(\alpha) + 2\alpha \coth^3(\alpha) \right], \\ F_v(X) &= \frac{3\pi\gamma}{2\sqrt{M_0}} \tanh^2(\alpha) (1 - \tanh^2(\alpha)), \end{aligned} \quad (6.8)$$

and $\alpha = \sqrt{2}\gamma X$. The constants M_v , w and ω_1 are defined as

$$M_v = \gamma \frac{2\sqrt{2}}{3}, \quad w^2 = \gamma \omega_1^2, \quad \omega_1 = \sqrt{\frac{3}{2}} \quad \text{and} \quad \gamma = \frac{1}{\sqrt{1 - v_{in}^2}}.$$

We have dropped the mixed terms with A and \dot{X} in the effective Lagrangian (6.7) by

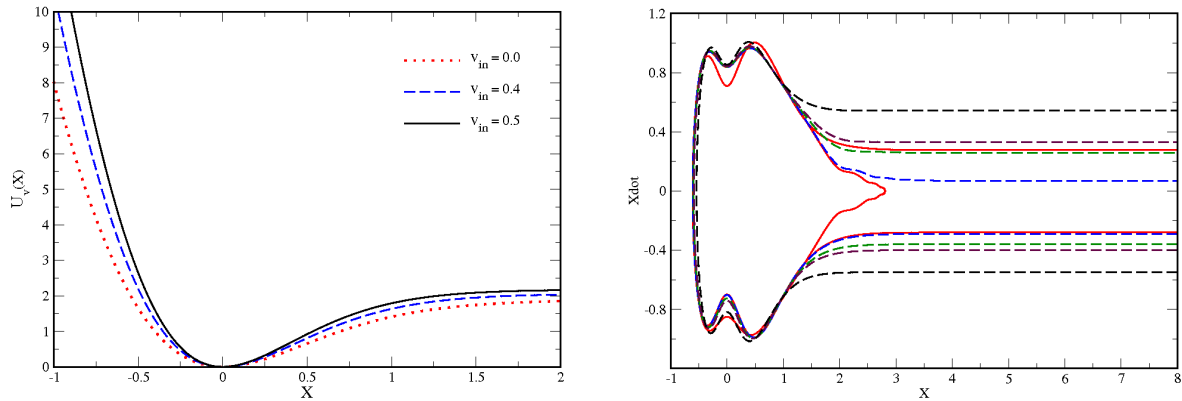


Figure 6.9: (a) and (b) display the potential $U_v(X)$ and the velocity \dot{X} , respectively, of the reduced system of the kink–antikink pairs as a function of the collective coordinate X . In figure (b) the dashed lines were calculated with initial velocities higher than the critical velocity and the solid lines with initial velocity less than the critical velocity. Note that in the collective coordinates system the critical velocity is $v_c \approx 0.283$.

assuming that they are very small. Application of the Euler-Lagrangian equations (2.2) to the effective Lagrangian, equation (6.7), gives the evolution equations for the collective coordinate X ,

$$\ddot{X} = \frac{1}{2(M_v + I(X))} (-I'_v(X)\dot{X}^2 + 2F'_v(X)A - U'_v(X)), \quad (6.9)$$

where the prime indicates the first derivative with respect to X , and the time-dependent amplitude $A(t)$ obeys

$$\ddot{A} + \gamma^2 \omega_1^2 A = \gamma F_v(X). \quad (6.10)$$

We numerically solve equations (6.9) and (6.10) with the initial conditions, at time $t = 0$ $X(0) = 10$, $\dot{X}(0) = -v_{in}$ and $A(0) = \dot{A}(0) = 0$, using a fourth-order Runge-Kutta method [53]. This collective coordinate approach confirms what we have been anticipating earlier from our numerical simulations about the dynamics of the kink–antikink pairs system: the kink and antikink exhibit attraction when they come close to each other and at some distance repel. This can be observed from the potential $U_v(X)$ at different initial velocities in Figure 6.9a. Further, we exhibit the phase diagram of the collective coordinate system in Figure 6.9b. It displays the velocity of the system as function of the collective coordinate X . In this framework we have measured the critical velocity to be $v_c \approx 0.283$, which is slightly different from what we have measured in our numerical simulation of the kink–antikink collisions system, *i.e.* $v_c \approx 0.26$.

Further, Figure 6.10a displays the change of the average velocity \bar{v} , equation (6.3), with the position coordinate of the antikink (or kink) in the kink–antikink collision. This average velocity \bar{v} is calculated from the field configuration obtained from two different approaches, the partial differential equation (PDE) (3.8) and the ordinary differential equation (ODE) (6.9). From this figure we observe that the final velocity in the PDE system is larger than the one in ODE system. This happens because in the ODE system

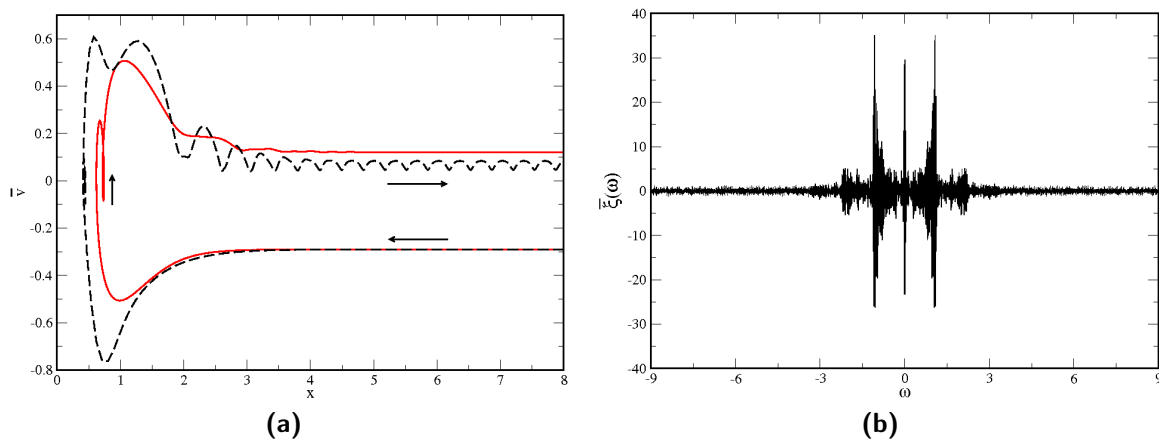


Figure 6.10: (a) The solid (dashed) line displays the average velocity that is calculated through the partial differential equation (3.8) (ordinary differential equation (6.9)). (b) Fourier transform function $\bar{\xi}(\omega)$ of the bound state in Figure 6.4a.

only two (slowly moving) degrees of freedom contribute to the energy density. But, in the PDE system additional (fast moving) fluctuations enter the average, equation (6.4), from which the velocity is extracted. Furthermore, when we Fourier transform the bound state oscillations $\varphi(0, t)$ at the center, as shown in Figure 6.4a, with respect to time t

$$\bar{\xi}(\omega) = \int d\omega \varphi(0, t) e^{i\omega t}, \quad (6.11)$$

we observe structures more than the shape mode. This is depicted in Figure 6.10b, which is symmetric around $\omega = 0$ because $\varphi(0, t)$ is real. We observe three peaks, one at $\omega = 0$ and two at $\omega \approx \pm 1.09$. We interpret the peak at $\omega = 0$ as a signal for the zero mode and at $\omega \approx \pm 1.09$ for the shape mode. The frequency $\omega \approx 1.09$ is obviously less than the shape mode frequency $\omega_1 = \sqrt{3}/2 \approx 1.22$ that is obtained by the collective coordinate approximation. We therefore conclude that the collective coordinate ansätze, equation (6.6), is not a good approximation to the kink–antikink collisions system, equation (3.8), although it gives a reasonable picture for the interaction potential $U_v(X)$ of the kink–antikink interaction and suggests that the shape mode is responsible for the bouncing between the kink–antikink.

6.3 Extraction of scattering data

So far, from the numerical solutions of the kink–antikink collisions we see that the kink–antikink either annihilate to a bound (bion) state plus emitted radiation or inelastically scatter to kink–antikink plus emitted radiation. In this context we discuss and extract the scattering amplitudes for the inelastic scattering and annihilation processes of the kink–antikink.

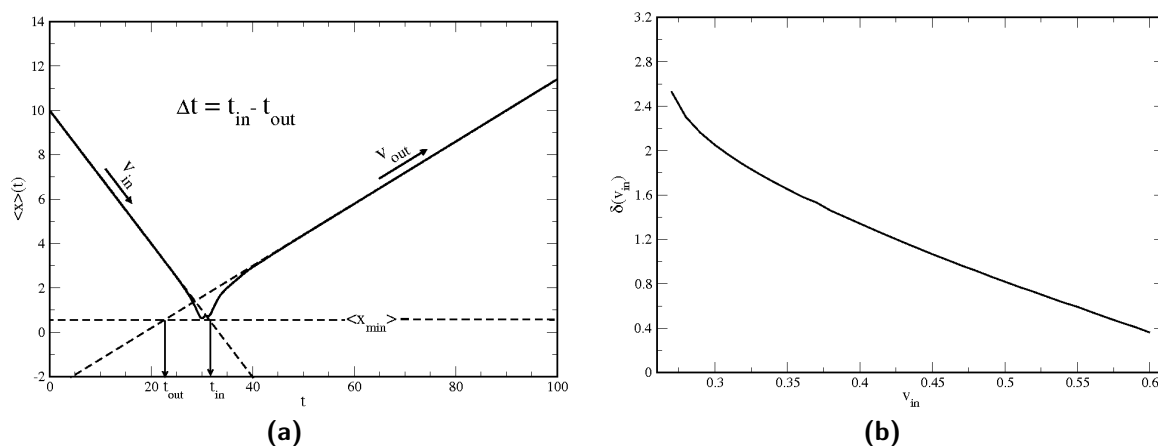


Figure 6.11: (a) The incoming and outgoing paths in the trajectory of the antikink, with $\langle x_{min} \rangle = 0$. (b) The phase shift of the kink–antikink as a function of the initial velocity in the inelastic scattering process of the kink–antikink.

6.3.1 Inelastic scattering process

As we have seen earlier, inelastic scattering of the kink–antikink is observed when the initial velocity of the system is beyond the critical velocity or takes place in some intervals below the critical velocity v_c . We can extract the scattering amplitude of the inelastic scattering process of the kink–antikink if the final state of the system contains kink–antikink. For simplicity, we here extract the scattering amplitude when the initial velocity of the system is higher than the critical velocity. In that regime the kink and the antikink always collide and directly reflect to infinity without bouncing. Below the critical velocity, we assume that the calculations behave similarly between the kink and the antikink after they depart to infinity. We choose the initial velocity v_{in} of the system between v_c and 0.95, and use equation (6.3) to calculate the final velocity v_{out} of the system. For every initial velocity in $v_c \leq v_{in} \leq 0.95$ we draw a trajectory graph similar to Figure 6.11a with incoming and outgoing antikink paths. We define the incoming path of the antikink, before the collision, as

$$\langle x \rangle - \langle x_{min} \rangle = -v_{in}(t - t_{in}) \quad (6.12)$$

and the outgoing path, after the collision, as

$$\langle x \rangle - \langle x_{min} \rangle = v_{out}(t - t_{out}), \quad (6.13)$$

where $\langle x_{min} \rangle$ is the half of the smallest separation distance between the kink and the antikink found during the collision. For each trajectory graph, we determine t_{in} for the incoming antikink path, as well as t_{out} for the outgoing antikink path. In terms of these times, t_{in} and t_{out} , we define the time delay between the incoming and outgoing antikinks (or kinks) as

$$\Delta t = t_{in} - t_{out}. \quad (6.14)$$

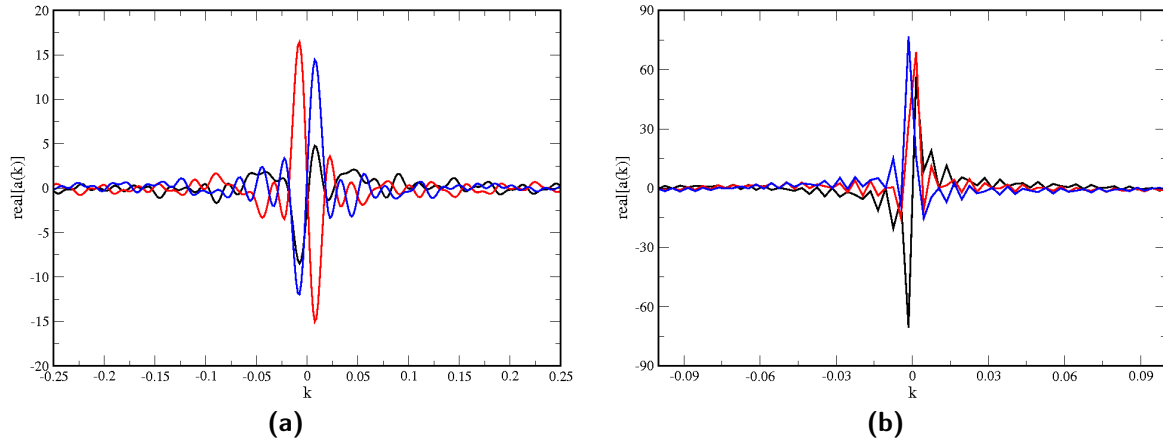


Figure 6.12: (a) The real part of the scattering amplitude of the emitted phonons in the scattering process of the kink–antikink with initial velocity v_{in} higher than the critical velocity v_c at different times. (b) The real part of the scattering amplitude of the emitted phonons in the annihilation process of the kink–antikink with initial velocity v_{in} less than the critical velocity v_c at different times.

Now, we multiply the time delay Δt by $v_{out}/\sqrt{1-v_{out}^2}$ to get the phase shift

$$\delta(v_{in}) = \frac{v_{out}}{\sqrt{1-v_{out}^2}} \Delta t, \quad (6.15)$$

where the phase shift is just a change in the phase of the kink-solution. In Figure (6.11b) we show the variation of this phase shift $\delta(v_{in})$ with the initial velocity v_{in} . Note that in this figure we have taken $\langle x_{min} \rangle = 0$, which is done by calculating the mean value of the position in equation (6.4) for high power, $j = 150$, of the energy density $\varepsilon(x, t)$. Further, the scattering amplitude $a(v_{in})$, relative to hard core reflection, of the inelastic scattering process of the kink–antikink is given by

$$a(v_{in}) = \rho \sin(\delta) e^{i\delta}; \quad \rho^2 = \left| \frac{\mathcal{J}_{out}}{\mathcal{J}_{in}} \right| = \frac{v_{out}}{v_{in}} \sqrt{\frac{1-v_{in}^2}{1-v_{out}^2}}, \quad (6.16)$$

where ρ is the inelasticity coefficient. It is defined as the ratio of the outgoing \mathcal{J}_{out} and incoming \mathcal{J}_{in} fluxes. For the single antikink the flux can easily be computed to be $\mathcal{J} \sim v/\sqrt{1-v^2}$.

Phonon emission in the kink–antikink background

In this scattering process with the initial velocity v_{in} higher than the critical velocity, we use equation (4.19) to Lorentz transform the final state $\varphi_f(x, t)$, which contains the moving kink–antikink plus emitted perturbative radiation, to the rest frame of the antikink.² Therefore, the transformed field configuration $\bar{\varphi}_f(Z, \tau)$ consists of a stationary kink and antikink plus emitted perturbative radiation. From our numerical simulations

²After transforming $\varphi(x, t) \rightarrow \bar{\varphi}(Z, \tau)$ we use the bilinear interpolation method [53] to find $\bar{\varphi}(Z_i, \tau_i)$ for a prescribed grid $\{Z_i, \tau_i\}$.

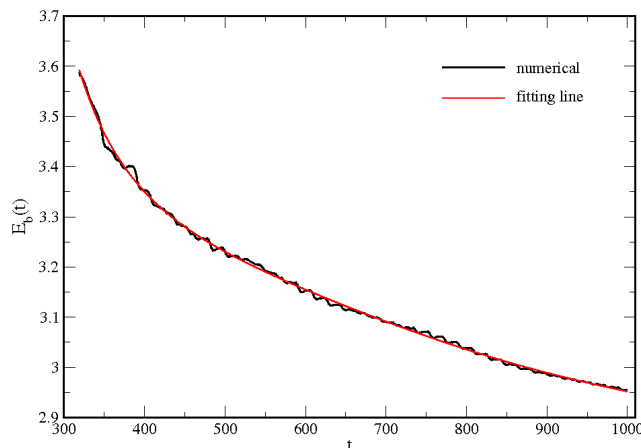


Figure 6.13: The change of the bion state energy $E_b(t)$ with the time t .

we have observed that the amplitude of the emitted radiation is very small compared to the amplitude of the kinks. Thus, we use the small amplitude fluctuation approach about a static kink-solution, section 4.1, to determine the scattering amplitude of the emitted phonons in the scattering process of the kink–antikink. The emitted perturbative radiation is defined as $\xi(Z, \tau) = \bar{\varphi}(Z, \tau) - \varphi_{\bar{K}}(Z)$, which obeys the equation of motion (4.20). Following the discussion in section 4.3, we therefore determine the scattering amplitude of the emitted phonons in the scattering process for the kink–antikink using equation (4.24). Figure 6.12a displays the real part of the scattering amplitude of the emitted phonons at different times, for kink–antikink scattering with initial velocities beyond the critical velocity. We observe that the scattering amplitude varies with the time τ , which is not expected. We assume this happens because the shape mode decays very slowly and its amplitude is beyond the small amplitude approximation.

6.3.2 Annihilation process

The annihilation process for the kink and antikink is observed for some intervals of the initial velocity less than the critical velocity. In this process, the final state always consists of the bion state accompanied by emitted radiation, without a kink or an antikink. We numerically calculate the final state, the field configuration $\varphi_f(x, t) = \xi(x, t)$ and its time derivative $\dot{\varphi}_f(x, t) = \dot{\xi}(x, t)$, for the annihilation process. Then, we recall equation (4.24) to determine the scattering amplitude $a_{v < v_c}(k, t)$,

$$a_{v < v_c}(k, t) = \frac{e^{i\omega_k t}}{4\pi} \int_{x_0}^{\infty} dx \left[\xi(x, t) + \frac{i}{\omega_k} \dot{\xi}(x, t) \right] \eta_k^*(x). \quad (6.17)$$

Here $\omega_k = \sqrt{k^2 + 2}$ and the emitted radiation modes are just plane waves *i.e.* $\eta_k(x) = e^{ikx}$. We integrate equation (6.17) over the space from $x_0 = 10$ to ∞ to avoid any contribution of the bion state to the Fourier transformation. Figure 6.12b displays the real part of the scattering amplitude $a_{v < v_c}(k)$ of the emitted radiation at different times in the annihilation process of the kink–antikink. We observe that the scattering amplitude

$a_{v < v_c}(k)$ varies moderately with the time t . We interpret this as a signal for the existence of some emitted radiation from the decay process of the bion state. For this we compute the change of the bion state energy $E_b(t)$,

$$E_b(t) = \int_{-a}^a dx \varepsilon(x, t), \quad (6.18)$$

with time t in Figure (6.13). Here $2a$ is the length where the bion state is located in the final state and $\varepsilon(x, t)$ is given by equation (3.3). Also, in Figure (6.13) we draw a fitting line with formula

$$E_b(t) \approx \frac{\exp(-a_1 t)}{a_2 + a_3 t + a_4 t^2 + a_5 t^3} + a_6, \quad (6.19)$$

where a_i 's are constants ($i = 1, 2, \dots, 6$). The agreement with this formula suggests that even at very late times, $t \rightarrow \infty$, the bion state still has a non-zero energy ($E_b \approx a_6$). Earlier studies [61, 62] have shown that the bion state of energy $E_b \lesssim 1$ decays asymptotically as $(\ln t)^{-1}$. Note that the initial state of the kink–antikink interaction has an energy $2M_0 \approx 1.88$. The final state has the energy of the bion state (E_b) and the emitted phonons. In [61] it has been estimated that at $t = 10^4$ the energy of the bion state is $E_b \approx 0.97$ and approximately half of its energy is radiated away at $t = 10^{11}$. But at $t = 10^{22}$, the bion state still has energy $E_b \approx 0.25$. Therefore, we cannot determine the exact scattering amplitude of emitted phonons in the annihilation process of the kink–antikink, since the annihilation state is not found even at very late times.

Chapter 7

Summary and Conclusion

In this thesis we have numerically solved the time dependent equation of motion in the non-integrable φ^4 field model in $(1 + 1)$ space-time dimensions. We have focused on the scattering of a wave packet about the static kink solution and kink–antikink collisions. The main motivation of these investigations was the working hypothesis that the scattering data of these two interactions should be related by crossing symmetry. We have seen within a perturbative treatment of a suitable field theory how this crossing symmetry relates the scattering amplitudes of the meson–baryon scattering process and the baryon–antibaryon annihilation process to each other by analytic continuation, as in section 2.5. Further, this property allows antiparticles, *e.g.* antibaryons, to be interpreted as particles, *e.g.* baryons, going backwards in time. This also allows form factors in the space- and time-like momentum regime to be related to each other by analytic continuation.

However in soliton models this remarkable property is less obvious. The main reason is that the scattering amplitudes of different processes concern distinct topological sectors, which are not related by any continuous transformation. For example, as discussed in ref.[63], the crossing symmetry between the kink–kink¹ and the kink–antikink interactions is possible in the integrable sine-Gordon field model, even though these interactions take place in different topological sectors. In contrast, in the non-integrable φ^4 field model, the crossing symmetry between the kink–kink and the kink–antikink is not possible. The simple reason is that an initial (or final) configuration describing widely separated two kinks (or antikinks) is not a stationary state. In the non-integrable φ^4 field model, the crossing symmetry between the scattering process of a wave packet off a kink solution and the annihilation process of the kink–antikink is topologically possible. In contrast, the crossing symmetry between the interactions of a wave packet about a static kink-solution and the kink–antikink is not possible in the integrable sine-Gordon field model. This happens because there is no annihilation state in the kink–antikink channel and the kink–wave packet amplitude is nonzero. We summarize the comparison between these two models in table 7.1.

Motivated by the concept of crossing symmetry, we have performed individual nu-

¹We have shown in chapter 3 that the soliton-solution of the integrable sine-Gordon field model in $(1 + 1)$ space-time dimensions is the kink-solution.

processes \ models	sine-Gordon	φ^4
phonon + $\varphi_K \rightarrow$ phonon + φ_K and $\varphi_K + \varphi_{\bar{K}} \rightarrow$ phonons	not realized	possible
$\varphi_K + \varphi_{\bar{K}} \rightarrow \varphi_K + \varphi_{\bar{K}}$ and $\varphi_K + \varphi_K \rightarrow \varphi_K + \varphi_K$	possible	not possible

Table 7.1: Possibilities of crossing symmetry in the integrable sine-Gordon and non-integrable φ^4 models.

numerical simulations for both “kink–wave packet” and “kink–antikink” interactions in the non-integrable φ^4 field model in $(1 + 1)$ space-time dimensions. For the first interaction, the scattering of a wave packet off the kink-solution, we have produced the phase shift known from potential scattering in the small amplitude approximation. By choosing a significantly wide initial spectral function (in momentum space) this was possible using a single integration of the equation of motion in coordinate space. However, numerical accuracy can be improved by both optimizing numerical parameters and restricting initial conditions to a special momentum regime. Although our technique also captures non-linear effects, we did not observe them for the phase shift in the regime of small and moderate amplitude of the wave packet. In this regime the kink does not pick up any energy from the wave packet. However, it gets displaced as a result of the interaction. Surprisingly, the displacement is opposite to the propagation direction of the kink. This displacement occurs as attraction before and repulsion after the interaction. Upon further increase of the amplitude, the kink picks up kinetic energy and gets dragged by the wave packet. Once the kink co-moves with the wave packet, the scattering process cannot be uniquely identified nor can a phase shift be extracted. This is our main result regarding the search for effects of the non-linear dynamics. We interpret this effect as a signal for the existence of a critical amplitude beyond which the attraction between the wave packet and the kink are inescapable. Furthermore, the wave packet splits into two or more distinct pieces for sufficiently large amplitudes. We interpret this splitting as particle production. It is a consequence of the non-linear dynamics because it is also observed without the kink background.

The numerical framework of the “kink–wave packet” scattering makes no particular reference to the background configuration and we can equally well use it to study the kink–antikink system. To do so, we have set up the initial conditions to investigate the kink–antikink interaction. In this topologically trivial sector, we have seen that the collision results dramatically vary with the impact velocity of the kink–antikink system. The kink and the antikink either annihilate, *i.e.* $\varphi_K + \varphi_{\bar{K}} \rightarrow$ phonons, or inelastically scatter from each other, *i.e.* $\varphi_K + \varphi_{\bar{K}} \rightarrow \varphi_K + \varphi_{\bar{K}} +$ phonons. We have been able to measure the critical velocity, $v_c \approx 0.26$ for the kink–antikink collision. For initial velocities of the system less than v_c , the annihilation and the inelastic scattering processes of the kink–antikink take place erratically. However, above v_c the kink and the antikink always scatter inelastically. The scattering processes of the kink–antikink with initial velocity

less and higher than the critical velocity are different, whereas below v_c the kink–antikink collide and always show n bounces ($n \geq 2$) before they depart to infinity. When the initial velocity of the system is higher than the critical velocity v_c the kink and the antikink depart to infinity after only a single bounce. For the bounce states that occur between the kink and the antikink, we have preserved a qualitative explanation from earlier studies as well as from our numerical simulations. We have observed over 20 two-bounce windows and windows with up to seven bounces. We have noticed that as long as we decrease the window width, for initial velocity within $0.0001 \leq v_{in} \leq v_c$, we can observe more bounce windows.

We have determined the phase shift $\delta(v_{in})$ and the scattering amplitude $a(v_{in})$ of the kink–antikink in the inelastic scattering process as functions of the initial velocity. Furthermore, in the scattering process for the kink–antikink, we have been able to numerically transform our numerical solution for the final state to the rest frame of the antikink. This transformation allowed us to compare our numerical data to the small amplitude approximation. As a result, we have been able to determine the scattering amplitude for emitted phonons in the scattering process as a function of their momentum. We have observed that this scattering amplitude depends on the duration of the simulation. We assume this happens because the shape mode decays very slowly and its amplitude is too big for the small amplitude approximation to be applicable. Moreover, in the annihilation process for the kink–antikink, we have determined the scattering amplitude of the emitted phonons. Again, the resultant scattering amplitude is time-dependent. Here, the reason is that the final state of the annihilation process of the kink–antikink contains the bion state plus the emitted phonons. Since the bion state has an ambiguous shape, we have not been able to subtract it from the final state configuration of the annihilation process to single out the emitted phonons. The decay rate of this bion state is very slow, with approximately 0.5% of its energy lost during one period of its oscillation. Although this suggests that the bion state energy decays exponentially with time, we observe that even at $t \rightarrow \infty$ the bion state is approximately stable and has some energy. Earlier studies [61, 62] showed that small-amplitude φ^4 breathers (or bion state) of energy $E_b \lesssim 1$ decay asymptotically as $(\ln t)^{-1}$. We recall that in these units the energy of the kink–antikink before the interaction is $2M_0 \approx 1.88$. The final state has the energy of the bion state (E_b) and the emitted phonons. In [61] it has been estimated that at $t = 10^4$ the energy of the bion state is $E_b \approx 0.97$ and approximately half of its energy is radiated away at $t = 10^{11}$. But at $t = 10^{22}$ the bion state still has an energy $E_b \approx 0.25$.

In conclusion, in the non-integrable φ^4 model in $(1 + 1)$ space-time dimensions the crossing symmetry between the scattering process of a wave packet off a kink solution and the annihilation process of the kink–antikink does not seem to exist, although it is possible to define topologically when the bion state has no energy and the final state of the annihilation process of the kink–antikink has only emitted phonons. In addition, for kink–antikink collisions in the non-integrable φ^4 model in $(1 + 1)$ space-time dimensions, we have modified the ansätze of the collective coordinate approximation from earlier studies to account for relativistic effects. In this framework, we have studied kink–antikink collisions in a reduced description that introduces only two degrees of freedom. We have numerically solved the ordinary differential equation (ODE) system of the collective

coordinate $X(t)$. In this approximation, we have measured the critical velocity to be $v_c \approx 0.283$, which moderately differs from that of the full system. Also, we have been able to determine the shape of the potential energy between the kink–antikink at different initial velocities. Further, we have given the phase diagram of the kink–antikink system at different initial velocities. This approximation gives a reasonable representation of the shape of the potential energy, and suggests that the shape mode ξ_1 is responsible for the bouncing effects between the kink–antikink. However, the comparison of the field configuration with the one from the full system suggests that this approximation is not a good approach for the kink–antikink system.

Further study of the one-dimensional non-integrable scalar φ^6 model might shed light on the question of whether the shape mode is responsible for the bounce effect in the kink–antikink collisions. Although the single-kink solutions for this model do not possess an internal vibrational (shape) mode, ref.[64] showed that the kink and the antikink have a resonant scattering structure. In the φ^6 model we thus want to utilize the collective coordinate system to study the kink–antikink collisions system in a similar reduction to a system with only two degrees of freedom. The crucial question then is whether this reduction exhibits a bion structure, even though it cannot be regarded a solution to the equation of motion.

Appendix A

A.1 Wick's Theorem for equation (2.32)

This theorem tells us how to go from time ordered products to the normal ordered products. Following Wick's rules in [1], we write the six field example, which is mentioned in section 2.4, as

$$\begin{aligned}
 T (: \bar{\psi}(x)\varphi(x)\psi(x) :: \bar{\psi}(y)\varphi(y)\psi(y) :) &= : \bar{\psi}(x)\varphi(x)\psi(x)\bar{\psi}(y)\varphi(y)\psi(y) : \\
 &+ : \bar{\psi}(x)\varphi(x)\varphi(y)\psi(y) : \overbrace{\psi(x)\bar{\psi}(y)} \\
 &+ : \bar{\psi}(x)\psi(x)\bar{\psi}(y)\psi(y) : \overbrace{\varphi(x)\varphi(y)} \\
 &+ : \varphi(x)\psi(x)\bar{\psi}(y)\varphi(y) : \overbrace{\bar{\psi}(x)\psi(y)} \\
 &+ : \bar{\psi}(x)\psi(y) : \overbrace{\psi(x)\bar{\psi}(y)} \overbrace{\varphi(x)\varphi(y)} \\
 &+ : \varphi(x)\varphi(y) : \overbrace{\psi(x)\bar{\psi}(y)} \overbrace{\bar{\psi}(x)\psi(y)} \\
 &+ \overbrace{\varphi(x)\varphi(y)} \overbrace{\psi(x)\bar{\psi}(y)} \overbrace{\bar{\psi}(x)\psi(y)} .
 \end{aligned}$$

Where the possible pairings $\overbrace{(\psi(x)\varphi(y))}$ and $\overbrace{(\bar{\psi}(x)\varphi(y))}$ are omitted because they give a zero contribution.

A.2 Feynman rules for model (2.27)

To each diagram we associate a number of rules;

- We draw all possible diagrams with appropriate external legs and add a momentum k' to each internal line (to impose the momentum conservation at each vertex).
- For each vertex, we write down a factor of

$$(-ig)(2\pi)^2 \delta^2 \left(\sum_i p_i \right) ,$$

where $\sum_i p_i$ is the sum of all momenta flowing into the vertex.

- For each internal solid line, corresponding to a ψ particle with momentum k' and mass M , we write down the factor (the Feynman propagator or the two point Green function)

$$\frac{i}{k'^2 - M^2 + i\eta},$$

where $\eta \rightarrow 0^+$. Throughout this thesis $k'^2 \neq M^2$, so η is set to zero. We include the same factor for dotted internal φ lines, with the mass m replaced by the baryon mass M .

- We integrate over momentum k' flowing through each loop $\int \frac{d^2k'}{(2\pi)^2}$.
- We multiply by a symmetry factor $1/f$, where f is the number of permutations of internal lines and vertices that leave the diagram unchanged when the external lines are fixed.

A.3 Traveling wave solution for φ^4 model

We assume that $\varphi_v(t, x) = f(x - vt)$ in equation (3.8), where v is the speed of the solitary wave, with boundary conditions $\varphi_v = \pm \frac{m}{\sqrt{\lambda}}$, $\varphi'_v, \varphi''_v \rightarrow 0$ as $|x| \rightarrow \infty$, then (3.8) becomes

$$v^2 f'' - f'' = m^2 f - \lambda f^3$$

$$f''(1 - v^2) = \lambda f(f^2 - m^2/\lambda), \quad (\text{A.1})$$

where the two primes indicate the second derivative of $f(x - vt)$ with respect to the argument $(x - vt)$. We multiply both sides of (A.1) by f' and integrate, to get

$$(f')^2(1 - v^2) = \frac{\lambda}{2}(f^2 - m^2/\lambda)^2 + B, \quad (\text{A.2})$$

where B is a constant of integration. We use the boundary conditions $\varphi = \pm \frac{m}{\sqrt{\lambda}}$, $\varphi'_v, \varphi''_v \rightarrow 0$ as $|x| \rightarrow \infty$, then $B = 0$. Therefore (A.2) becomes

$$\frac{df}{d(x - vt)} = \pm \sqrt{\frac{\frac{\lambda}{2}(f^2 - \frac{m^2}{\lambda})^2}{1 - v^2}}$$

or

$$\int_{f(x_1)}^{f(x-vt)} \frac{df}{\sqrt{\frac{\lambda}{2}(f^2 - m^2/\lambda)}} = \pm \int_{x_1}^{x-vt} \frac{d(x - vt)}{\sqrt{1 - v^2}}. \quad (\text{A.3})$$

where x_1 is the initial position, any arbitrary point where the traveling wave f has the value $f(x_1)$. Then (A.3) becomes

$$f(x - vt) = \pm \frac{m}{\sqrt{\lambda}} \tanh \left[\frac{m}{\sqrt{2}} \left(\frac{x - vt}{\sqrt{1 - v^2}} \right) \right]$$

A.4 Traveling wave solution for sine-Gordon model

We are looking for solution of the form $\varphi = f(x - vt)$, since $\frac{\partial^2 \varphi}{\partial x^2} = f''$ and $\frac{\partial^2 \varphi}{\partial t^2} = v^2 f''$, then (3.40) becomes

$$f''(1 - v^2) = \sin f,$$

or

$$f'' = \gamma^2 \sin f, \quad (\text{A.4})$$

where $\gamma = \frac{1}{\sqrt{1-v^2}}$. We multiply (A.4) by f' and integrate to find

$$(f')^2 = A - 2\gamma^2 \cos f,$$

or

$$f' = \pm \sqrt{A - 2\gamma^2 \cos f}, \quad (\text{A.5})$$

As $x \rightarrow \pm\infty$ we impose $f' = f'' = 0$ and $f(x) \rightarrow 2\pi n$. Therefore $A = 2\gamma^2$ and

$$f' = \pm \sqrt{2\gamma^2 \sqrt{1 - \cos f}}, \quad (\text{A.6})$$

Integrating

$$\int \frac{df}{\sqrt{1 - \cos f}} = \pm \sqrt{2}\gamma(x - vt), \quad = \sqrt{2} \log \left(\tan \left(\frac{f}{4} \right) \right) + \text{constant} \quad (\text{A.7})$$

Picking the constant to be equal to $\pm\sqrt{2}\gamma x_0$, then

$$\varphi(x, t) \equiv f(x - vt) = 4 \arctan \left(e^{\pm\gamma(x-x_0-vt)} \right). \quad (\text{A.8})$$

Appendix B

B.1 Numerical solutions

In this appendix we show our numerical treatments for solving the time-dependent equation of motion (3.8)

$$\ddot{\varphi}(x, t) = \varphi''(x, t) + \varphi(x, t) - \varphi^3(x, t). \quad (\text{B.1})$$

Our numerical treatments start by using the conditions (5.12) and defining the position axis as

$$x_n = x_{min} + (x_{max} - x_{min}) \frac{n - 1}{n_x - 1} \quad (\text{B.2})$$

where $n = 1, 2, 3, \dots, n_x$ and $x_{min} = x_1$ and $x_{max} = x_{n_x}$. In the same way as in equation (B.2) we define the momentum axis. The time axis is defined as

$$t_j = t_{min} + \Delta t$$

where $j = 1, 2, 3, \dots, j_t$ and $t_{min} = t_1$ and $t_{max} = t_{j_t}$ and Δt is defined via the adaptive step size method discussed below. Note that the position and momentum points are equidistant, but the time point is not. We solve equation (B.1) for distinct initial conditions

i) For the scattering of a wave packet off the kink-solution:

a) In the trivial topological sector (the wave packet in vacuum background), the initial field configuration $\varphi(x_n, t_1) \equiv \varphi_{n,1}$ (at $t_1 = 0$) is

$$\varphi_{n,1} \equiv \varphi(x_n, t_1) = 1 + \eta_{wp}(x_n). \quad (\text{B.3})$$

b) In the unit topological sector (the wave packet in kink background), the initial field configuration $\varphi(x_n, t_1)$ is

$$\varphi_{n,1} \equiv \varphi(x_n, t_1) = \varphi_K(x_n - x_0) + \eta_{wp}(x_n). \quad (\text{B.4})$$

Note that $\varphi_K(x_n - x_0)$ and $\eta_{wp}(x_n)$ are given by equations (3.15) and (3.21), respectively.

- ii) For the kink and antikink collisions (in the unit topological sector), the initial field configuration $\varphi(x_n, t_1)$ is

$$\varphi_{n,1} \equiv \varphi(x_n, t_1) = \varphi_K(x_n + x_0, t_1) - \varphi_{\bar{K}}(x_n - x_0, t_1) - 1. \quad (\text{B.5})$$

We use a fourth-order center difference scheme to approximate the first and second spatial derivatives [53]:

$$\varphi'_{n,1} \equiv \frac{d\varphi_{n,1}}{dx} = \frac{\varphi_{n-2,1} - 8\varphi_{n-1,1} + 8\varphi_{n+1,1} - \varphi_{n+2,1}}{12h}, \quad (\text{B.6})$$

$$\varphi''_{n,1} \equiv \frac{d^2\varphi_{n,1}}{dx^2} = \frac{-\varphi_{n-2,1} + 16\varphi_{n-1,1} - 30\varphi_{n,1} + 16\varphi_{n+1,1} - \varphi_{n+2,1}}{12h^2}, \quad (\text{B.7})$$

where $h = x_2 - x_1$. This leads to a set of n_x coupled second-order ordinary differential equations for the field $\varphi_{n,1} \equiv \varphi(x_n, t_1)$

$$\ddot{\varphi}_{n,1} = \varphi''_{n,1} - \varphi_{n,1}^3 + \varphi_{n,1}. \quad (\text{B.8})$$

Next, we use the fourth order Runge-Kutta algorithm to solve equation (B.8) in time for every t_j between t_{min} and t_{max} (with errors that scale as $(\Delta t)^5$ and $(\Delta x)^5$):

$$\begin{aligned} r1 &= \Delta t \ddot{\varphi}_{n,1} \\ s1 &= \Delta t \dot{\varphi}_{n,1} \end{aligned} \quad (\text{B.9})$$

$$\begin{aligned} r2 &= \Delta t (\varphi''_{n,1} + (s1''/2) - (\varphi_{n,1} + (s1/2))^3 + \varphi_{n,1} + (s1/2)) \\ s2 &= \Delta t (\dot{\varphi}_{n,1} + r1/2) \end{aligned} \quad (\text{B.10})$$

$$\begin{aligned} r3 &= \Delta t (\varphi''_{n,1} + (s2''/2) - (\varphi_{n,1} + (s2/2))^3 + \varphi_{n,1} + (s2/2)) \\ s3 &= \Delta t (\dot{\varphi}_{n,1} + r2/2) \end{aligned} \quad (\text{B.11})$$

$$\begin{aligned} r4 &= \Delta t (\varphi''_{n,1} + s3'' - (\varphi_{n,1} + s3)^3 + \varphi_{n,1} + s3) \\ s4 &= \Delta t (\dot{\varphi}_{n,1} + r3) \end{aligned} \quad (\text{B.12})$$

$$\begin{aligned} \dot{\varphi}_{n,2}(x_n, \Delta t) &= \dot{\varphi}_{n,1}(x_n, 0) + (r1 + 2r2 + 2r3 + r4)/6 \\ \varphi_{n,2}(x_n, \Delta t) &= \varphi_{n,1}(x_n, 0) + (s1 + 2s2 + 2s3 + s4)/6, \end{aligned} \quad (\text{B.13})$$

Therefore, we give inputs n_x , x , Δt , $\varphi_{n_x,j}$, and $\dot{\varphi}_{n_x,j}$ to Rung-Kutta subroutine and obtain outputs $\varphi_{n_x,j+1}$ and $\dot{\varphi}_{n_x,j+1}$. Finally we use an adaptive step size [53] to make sure that the integration over time is done in a good enough approximation. In the adaptive step size method we have two steps, big step and small step:

i- In the first step (one big step) we call Runge-Kutta subroutine

$$\text{input: } n_x, x, 2\Delta t, \varphi_{n_x,1}, \dot{\varphi}_{n_x,1} \rightarrow \text{output: } \varphi_c \dot{\varphi}_c.$$

ii- In the second step we have two small steps

– In the first small step we call Runge-Kutta subroutine

$$\text{input: } n_x, x, \Delta t, \varphi_{n_x,1}, \dot{\varphi}_{n_x,1} \rightarrow \text{output: } \varphi_a \dot{\varphi}_a,$$

– In the second small step we call Runge-Kutta subroutine

$$\text{input: } n_x, x, \Delta t, \varphi_a, \dot{\varphi}_a \rightarrow \text{output: } \varphi_b \dot{\varphi}_b.$$

Note that, for the first time to run Runge-Kutta and adaptive step size subroutines we put $\Delta t = 10^4 (t_{max} - t_{min})$. Next, we define

$$\begin{aligned} \Delta_0 &= 10^{-9} (|\varphi_{n_x,1}| + 2 \Delta t |\dot{\varphi}_{n_x,1}|) ; \Delta_1 = \varphi_c - \varphi_b, \\ \dot{\Delta}_0 &= 10^{-9} (|\dot{\varphi}_{n_x,1}| + 2 \Delta t |\ddot{\varphi}_{n_x,1}|) ; \dot{\Delta}_1 = \dot{\varphi}_c - \dot{\varphi}_b \text{ and} \\ \Delta_{max} &= \text{Maximum} \left(\left| \frac{\Delta_1}{\Delta_0} \right|, \left| \frac{\dot{\Delta}_1}{\dot{\Delta}_0} \right| \right). \end{aligned}$$

We use "if statement" to check whether the time increment is enough,

$$\text{if } (\Delta_{max} > 1.0) \text{ then we write } \Delta t(\text{new}) = 0.9 \Delta t(\text{old}) \left(\frac{1}{\Delta} \right)^{0.25}$$

and repeat Runge-Kutta and the adaptive step size at same time,

$$\text{elseif } (\Delta_{max} \leq 1.0) \text{ then we write } \Delta t(\text{new}) = 0.9 \Delta t(\text{old}) \left(\frac{1}{\Delta} \right)^{0.2}$$

at this moment ($\Delta_{max} \leq 1.0$) we calculate

$$\begin{aligned} \dot{\varphi}_{n,2} &= \dot{\varphi}_b + (\dot{\varphi}_c - \dot{\varphi}_b) / 15, \\ \varphi_{n,2} &= \varphi_b + (\varphi_c - \varphi_b) / 15. \end{aligned}$$

Then, we increase the time $t_2 = t_1 + \Delta t$. We run the adaptive step size subroutine until we get $t_j = t_{max}$. Therefore, we get the numerical field configuration solution $\varphi_{n,j} \equiv \varphi(x, t)$ at any time and position.

References

- [1] M.E. Peskin and D.V. Schroeder. *An Introduction to Quantum Field Theory*. Perseus Books Publishing, L.L.C., 1995.
- [2] J.D. Bjorken and S.D. Drell. *Relativistic Quantum Mechanics*. McGraw-Hill, Inc., 1964.
- [3] C. Weiss. Proton–antiproton annihilation into two photons at large s . 2002. arxiv:hep-ph/0206295v1.
- [4] A.R. Bishop and T. Schneider. *Solitons in Condensed Matter Physics*. Springer, Berlin, 1978.
- [5] T. Vachaspati. *Kinks and Domain Walls, An Introduction to Classical and Quantum Solitons*. Cambridge University Press, 2006.
- [6] V. Belinski and E. Verdaguer. *Gravitational Solitons*. Cambridge University Press, 2004.
- [7] N. Graham, M. Quandt, and H. Weigel. *Spectral Methods in Quantum Field Theory*. Springer, 2009.
- [8] R. Rajaraman. *An Introduction to Solitons and Instantons in Quantum Field Theory*. North-Holland, 1989.
- [9] L. Lam. *Introduction to Nonlinear Physics*. Springer-Verlag New York, Inc., 1997.
- [10] G.B. Whitham F.R.S. *Linear and Nonlinear Waves*. John Wiley & Sons, Inc., 1974.
- [11] P.G. Drazin and R.S. Johnson. *Solitons: An Introduction*. Cambridge University Press, 1989.
- [12] A.C. Scott, F.Y.F. Chu, and D.W. McLaughlin. The soliton: A new concept in applied science. *IEEE*, 61(10), October 1973.
- [13] N. Zettili. *Quantum Mechanics Concepts and Applications*. John Wiley & Sons Ltd, 2 edition, 2009.
- [14] J. Scott Russell. Report on waves, made to the meeting of the British association in 1842-43. *British association for the advancement of Science*, 1844.
- [15] J.K. Perring and T.H.R. Skyrme. A model unified field equation. *Nucl. Phys.*, 31(550), 1962.

- [16] N.J. Zabusky and M.D. Kruskal. Interaction of solitons in a collisionless plasma and the recurrence of initial states. *Phys. Rev.*, 51(240), 1965.
- [17] M. Dunajski. *Solitons, Instantons and Twistors*. Oxford University Press, 2010.
- [18] E.A. Kuznetsov, A.M. Rubenchik, and V.E. Zakharov. Soliton stability in plasmas and hydrodynamics. *Physics Reports*, 142(105), 1986.
- [19] N.F. Pedersen and D. Welner. Comparison between experiment and perturbation theory for solitons in Josephson junctions. *Phys. Rev. B*, 29(2551), 1984.
- [20] W. Hasenfratz and R. Klein. The interaction of a solitary wave solution with phonons in a one-dimensional model for displacive structural phase transition. *North-Holland Publishing Co.*, 1977.
- [21] E. Witten. Baryons in the $1/N$ expansion. *Nucl. Phys. B*, 160(57), 1979.
- [22] T.H.R. Skyrme. A unified field theory of mesons and baryons. *Nucl. Phys.*, 31(556), 1962.
- [23] H. Weigel. *Chiral Soliton Models for Baryons*. Springer-Verlag Berlin Heidelberg, 2008.
- [24] B. Schwesinger, H. Weigel, G. Holzwarth, and A. Hayashi. The Skyrme soliton in pion, vector- and scalar-meson field: πn -scattering and photoproduction. *Phys. Rept.*, 173(173), 1989.
- [25] M.M. Musakhanov, U.T. Yakhshiev, and A.M. Rakhimov. In-medium dynamics of antibaryon-baryon annihilation in the Skyrme model. *Physics Letters B*, 482(363), 2000.
- [26] M. Gleiser and R.C. Howell. Emergence of complex spatio-temporal behavior in nonlinear field theories. *AIP Conf. Proc.*, 861(501), 2006.
- [27] Y.S. Kivshar, Z. Fei, and L. Vazquez. Resonant soliton-impurity interactions. *Phys. Rev. Lett.*, 67(1177), 1991.
- [28] P.M. Saffin and A. Tranberg. Particle transfer in braneworld collisions. *J. High Energy Phys.*, 0708(072), 2007.
- [29] P.M. Saffin and A. Tranberg. The fermion spectrum in braneworld collisions. *J. High Energy Phys.*, 0712(053), 2007.
- [30] Y. Takamizu and K. Maeda. Collision of domain walls in asymptotically anti de sitter space-time. *Phys. Rev.*, 73(103508), 2006.
- [31] A.M.H.H. Abdelhady and H. Weigel. Wave-packet scattering off the kink-solution. *International Journal of Modern Physics A*, 26(21):3625-3640, July 2011. arXiv:1106.3497v1 [nlin.PS].
- [32] D.K. Campbell, J.F. Schonfeld, and C.A. Wingate. Resonance structure in kink-antikink interaction in φ^4 theory. *North-Holland Publishing Co.*, 1983.
- [33] J.A. Combs and S. Yip. Single-kink dynamics in a one-dimensional atomic chain: A non-linear atomistic theory and numerical simulation. *Phys. Rev. B*, 28(6873), 1983.

- [34] J.A. Combs and S. Yip. Molecular dynamics study of lattice kink diffusion. *Phys. Rev. B.*, 29(438), 1984.
- [35] S.V. Demidov and D.G. Levkov. Soliton pair creation in classical wave scattering. *J. High Energy Phys.*, 1106(016), 2011. arXiv:1103.2133v1 [hep-th].
- [36] A.B. Adib, M. Gleiser, and C.A.S. Almeida. Long-lived oscillons from asymmetric bubbles: existence and stability. *Phys. Rev. D*, 66(085011), 2002.
- [37] N. Graham. Numerical simulation of an electroweak oscillon. *Phys. Rev. D*, 76(085017), 2007.
- [38] R.H. Goodman and R. Haberman. Kink-antikink collisions in the φ^4 equation: The n -bounce resonance and the separatrix map. *Siam J. Appl. Dyn. Syst.*, 4(1195), 2005.
- [39] R.H. Goodman and R. Haberman. Chaotic scattering and the n -bounce resonance in solitary-wave interactions. *Phys. Rev. Lett.*, 98(104103), 2007.
- [40] M. Gleiser and R.C. Howell. Resonant nucleation. *Phys. Rev. Lett.*, 94(151601), 2005.
- [41] P. Roman. *Introduction to Quantum Field Theory*. John Wiley and Sons, Inc., 1968.
- [42] J. Govaerts. *An Introduction to Quantum Physics and Relativistic Quantum Field Theory*. Unpublished manuscript, 2008.
- [43] F. Gross. *Relativistic Quantum Mechanics and Field Theory*. John Wiley & Sons, Inc., 1993.
- [44] M. Maggiore. *A Modern Introduction to Quantum Field Theory*. Oxford University Press, 2005.
- [45] N. Manton and P. Sutcliffe. *Topological Solitons*. Cambridge University Press, 2004.
- [46] N.S. Manton and H. Merabet. φ^4 kinks—gradient flow and dynamics. *Nonlinearity*, 12(851), 1996. arXiv:hep-th/9605038.
- [47] M. Ślusarczyk. Dynamics of a planar domain wall with oscillating thickness in $\lambda\varphi^4$ model. *Acta Phys. Polon. B.*, 31(617), 2000. arXiv:hep-th/9903185.
- [48] G. Pöshl and E. Teller. *Z. Phys.*, 83(143), 1933.
- [49] K. Chadan and P.C. Sabatier. *Inverse Problems in Quantum Scattering Theory*. Springer, New York, 1977.
- [50] B.A. Malomed. Decay of shrinking solitons in multidimensional sine-Gordon equation. *Physica D*, 24(155), 1987.
- [51] S. Mandelstam. Soliton operators for the quantized sine-Gordon equation. *Phys. Rev. D*, 11(3026), 1975.
- [52] L.M. Widrow. The collapse of nearly spherical domain walls. *Phys. Rev. D*, 39(3576), 1989.

- [53] W.H. Press, S.A. Teukolsky, W.T. Vetterling, and B.P. Flannery. *Numerical recipes; The Art of Scientific Computing*. Cambridge University Press, 3 edition, 2007.
- [54] J. Shiefman and P. Kumar. Interaction between soliton pairs in a double sine-Gordon equation. *Physica Scripta.*, 20(435), 1979.
- [55] R.H. Goodman. Chaotic scattering in solitary wave interactions: A singular iterated-map description. *Chaos*, 18:023113, 2008. arXiv:0710.3209v1[nlin.PS].
- [56] P. Anninos, S. Oliveira, and R.A. Matzner. Fractal structure in the scalar $\lambda(\varphi^2 - 1)^2$ theory. *Physical Review D*, 44(4), 1991.
- [57] P. Hawrylak, K.R. Subbaswamy, and S.E. Trullinger. Numerical simulation of kink dynamics for a two-component field. *Physical Review D*, 29(6), 1983.
- [58] V.G. Makhankov. Dynamics of classical solitons. *Phys. Lett. c.*, 35(1), 1978.
- [59] A.E. Kudryavtsev. About Soliton Similar Solutions for Higgs Scalar Field. *Pisma Zh.Eksp.Teor.Fiz.*, 22:178–181, 1975.
- [60] T. Sugiyama. Kink–antikink collisions in the two-dimensional φ^4 model. *Prog. Theor. Phys.*, 61(1550), 1979.
- [61] J. Geicke. Logarithmic decay of φ^4 breather of energy $e \lesssim 1$. *Phys. Rev. E*, 49(4), 1994.
- [62] H. Segur and M.D. Kruskal. Nonexistence of small-amplitude breather solutions in φ^4 theory. *Phys. Rev. Lett.*, 58(8), 1987.
- [63] S. Coleman. Semiclassical crossing symmetry for semiclassical soliton scattering. *Physical Review D*, 12(6), 15 Sep. 1975.
- [64] P. Dorey, K. Mersh, T. Romanczukiewicz, and Y. Shnir. Kink–antikink collisions in the φ^6 model. *Phys. Rev. Lett.*, 107(091602), 2011. arXiv:1101.5951 [hep-th].